

**Technical Report  
1025**

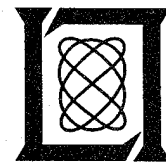
# **Applications of Tunable Lasers to Laser Radar and 3D Imaging**

**L.G. Shirley  
G.R. Hallerman**

**26 February 1996**

---

**Lincoln Laboratory**  
MASSACHUSETTS INSTITUTE OF TECHNOLOGY  
*LEXINGTON, MASSACHUSETTS*



---

Prepared for the Department of the Army under Air Force Contract F19628-95-C-0002.

Approved for public release; distribution is unlimited.

**19960410 054**

DTIC QUALITY INSPECTED 1

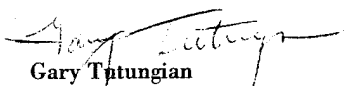
This report is based on studies performed at Lincoln Laboratory, a center for research operated by Massachusetts Institute of Technology. The work was sponsored by the Department of the Army under Air Force Contract F19628-95-C-0002.

This report may be reproduced to satisfy needs of U.S. Government agencies.

The ESC Public Affairs Office has reviewed this report, and it is releasable to the National Technical Information Service, where it will be available to the general public, including foreign nationals.

This technical report has been reviewed and is approved for publication.

**FOR THE COMMANDER**

  
Gary T. Tungian  
Administrative Contracting Officer  
Contracted Support Management

Non-Lincoln Recipients

PLEASE DO NOT RETURN

Permission is given to destroy this document  
when it is no longer needed.

MASSACHUSETTS INSTITUTE OF TECHNOLOGY  
LINCOLN LABORATORY

**APPLICATIONS OF TUNABLE LASERS TO  
LASER RADAR AND 3D IMAGING**

*LYLE G. SHIRLEY  
GREGORY R. HALLERMAN  
Group 35*

TECHNICAL REPORT 1025

26 FEBRUARY 1996

Approved for public release; distribution is unlimited.

LEXINGTON

MASSACHUSETTS

## ABSTRACT

This report demonstrates the remote sensing of a scattering object's size, shape, and surface properties using techniques based on the wavelength dependence of laser speckle. Originally, these techniques were motivated by applications of laser radar to target discrimination in ballistic missile defense. More recently, the emphasis has shifted to industrial applications of 3D imaging involving machine vision and dimensional metrology. Consequently, the report addresses a wide range of techniques and potential applications.

For applications to target discrimination, the capability of obtaining high-resolution measurements of the target's range-resolved laser radar cross section is emphasized. Submillimeter range resolutions are demonstrated in the laboratory. The analytical background is also included for predicting and understanding target signatures based on knowledge of the target's shape and the scattering properties of its surface materials.

Two approaches to high-resolution 3D imaging are considered that have many potential industrial applications. The first approach is an extension of the technique for measuring range-resolved laser radar cross section. The second approach relies on the wavelength dependence of laser speckle to provide range information and conventional optical imaging to provide lateral information. These techniques are analyzed theoretically and demonstrated in the laboratory. Together, they cover object sizes ranging from millimeters to meters.

## ACKNOWLEDGMENTS

This work was sponsored by the U.S. Army Space and Strategic Defense Command, the MIT Lincoln Laboratory Advanced Concepts Committee, and the MIT Lincoln Laboratory Civil Sector Team. The authors gratefully acknowledge the support of the Signature Studies and Analysis Group and the Radar Measurements Division at MIT Lincoln Laboratory.

The authors express gratitude for the many contributions of members of the Laser Speckle Laboratory: John R. Vivilecchia carried out a significant portion of the experimental work and assisted in the daily operation of the laboratory; Harold C. Payson developed signal-processing algorithms and suggested the reference-plane technique for 3D imaging using image speckle; Michael S. Mermelstein designed and developed a parallel processor for real-time data analysis and contributed to the implementation of a portable 3D imaging prototype; Emory D. Ariel was responsible for the mechanical design of targets and experimental apparatus; Peter A. Lo developed bispectral-analysis software; and John M. Fini verified much of the theoretical analysis.

The authors are grateful for the support, encouragement, and guidance of John A. Tabaczynski and Wade M. Kornegay, without whom this work would not have been possible. The contributions and support of many other individuals are gratefully acknowledged, including Marc D. Bernstein, Sidney L. Borison, Charles F. Bruce, Hsiao-Hua K. Burke, Vincent W.S. Chan, Thierry B. Copie, Kent R. Edwards, Joseph R. Guerci, William E. Keicher, David I. Klick, Herbert Kottler, Charles K. Meins, Jr., Harold Z. Ollin, Charles M. Rader, Kenneth R. Roth, Thomas M. Smith, Richard M. Spitzberg, David H. Staelin, Ernest Stern, and Berton C. Willard. Finally, the support, patience, and encouragement of Lyle G. Shirley's wife, Laurelyn, and family during the writing of this report are greatly appreciated.

## TABLE OF CONTENTS

Abstract	iii
Acknowledgments	v
List of Illustrations	ix
1. INTRODUCTION	1
2. SPATIAL PROPERTIES OF LASER SPECKLE	5
3. LASER RADAR CROSS SECTION AND RANGE-RESOLVED LASER RADAR CROSS SECTION	11
3.1 Definitions	11
3.2 Method of Calculation	12
3.3 On-Axis Illumination	15
3.4 Off-Axis Illumination	16
4. THEORY FOR WAVELENGTH DECORRELATION	29
4.1 Wavelength Dependence of Speckle	29
4.2 Spectral Density	31
4.3 Random-Process Representation	38
4.4 Coherent Detection	41
4.5 Phase Recovery	44
5. WAVELENGTH-DECORRELATION MEASUREMENTS	47
5.1 Laboratory Layout	47
5.2 Demonstration of Fundamental Concepts	49
5.3 Measurements of Range-Resolved Laser Radar Cross Section	54
5.4 Applications to Discrimination	61
6. 3D IMAGING	65
6.1 Speckle-Pattern Sampling	65
6.2 Image Speckle	104
7. SUMMARY	113
APPENDIX—ANGULAR-SCATTERING MEASUREMENTS	115
REFERENCES	119

## LIST OF ILLUSTRATIONS

Figure No.		Page
1	Transverse and longitudinal speckle size.	5
2	Effect of object shape on speckle patterns: photographs of laser-illuminated (a) 2.5-cm-long triconic, (b) 2.5-cm-diameter sphere, and (c) ring with an outer diameter of 2.5 cm and an inner diameter of 2.0 cm; their corresponding speckle patterns are shown in (d), (e), and (f), respectively; the ensemble-averaged autocorrelation functions (40 averages) of the speckle patterns are shown in (g), (h), and (i), respectively.	7
3	Computer-simulated normalized speckle intensity from a 20-wavelength-long linear array of randomly phased point-scatterers: (a) longitudinal slice of the speckle pattern cutting through the linear array; (b) speckle intensity versus logarithm of distance for a horizontal line lying in the longitudinal slice and beginning at the center of the linear array; (c) speckle intensity along a radial line 30° above the horizontal; (d) speckle intensity along a radial line 60° above the horizontal. The speckle intensity is normalized by dividing by the expected value of the intensity at each point.	8
4	Measured 3D speckle pattern from a ground-glass diffuser back-illuminated by a 25- $\mu\text{m}$ -diameter 0.633- $\mu\text{m}$ -wavelength HeNe laser spot. This image was formed by stacking a series of 150 CCD images of the speckle pattern, with a longitudinal displacement of 2 $\mu\text{m}$ between frames.	9
5	The coordinate system used to define laser radar cross section and range-resolved laser radar cross section.	12
6	Circularly shaped integration paths for calculating the range-resolved laser radar cross section $U(z)$ for a cone illuminated on axis.	14
7	Range-resolved laser radar cross sections for on-axis viewing: (a) top hat; (b) cone; (c) Lambertian sphere.	17
8	Coordinate system for describing the object height function $h(\xi, \eta)$ and the direction of illumination $(\alpha, \beta)$ .	18
9	Region of integration for calculating the laser radar cross section for off-axis illumination of a cone. As the aspect angle increases, the angular range of integration $\pm\phi_s$ in the projection plane decreases. This range of integration corresponds to the illuminated surface area of the cone.	19
10	Aspect-angle dependence of the laser radar cross section of a 10-cm-long Lambertian cone with a cone half-angle of 15°. The separate contributions from the cone and the disk base are indicated.	20

## LIST OF ILLUSTRATIONS (Continued)

Figure No.		Page
11	Range-resolved laser radar cross section of a 1-cm-radius Lambertian disk at various illumination angles.	21
12	Limits of integration for calculating the range-resolved laser radar cross section for off-axis illumination of a truncated cone: (a) shadow boundaries and truncation boundaries for three separate range planes cutting through the cone; (b) the corresponding integration paths in $\xi$ - $\eta$ space.	23
13	Range-resolved laser radar cross section for a truncated Lambertian cone viewed at various aspect angles. The cone half-angle is $15^\circ$ and the distance between the truncation planes is 10 cm. The range-reference point is located at the apex of the corresponding untruncated cone, which is located 5 cm to the left of the first truncation plane. There are no contributions from the disk-shaped regions formed by the intersection of the truncation planes with the cone.	24
14	Range-resolved laser radar cross section for a Lambertian cylinder viewed at various aspect angles. The length of the cylinder is 10 cm and its diameter is 4 cm. The range-reference point is located 5 cm outside of the cylinder to separate the various plots in range. There are no contributions from the disk-shaped endcaps.	26
15	Range-resolved laser radar cross section for a 1-cm-radius Lambertian hemisphere viewed at various aspect angles.	27
16	Wavelength-decorrelation signatures for composite objects: (a) Lambertian sphere-cone-disk combination; (b) Lambertian cylinder with disk endcaps; (c) and (d) aspect-angle dependence of the range-resolved laser radar cross section for parts a and b, respectively; (e) and (f) autocorrelation functions of the range-resolved laser radar cross section for parts a and b, respectively. The magnitude of these signatures is plotted on a logarithmic scale covering four decades for parts c and d and two decades for parts e and f.	28
17	Frequency dependence of the on-axis speckle intensity from a step target: (a) step target with phasors indicating contributions from each step for two frequencies; (b) path of resultant complex amplitude in the complex plane; (c) frequency dependence of intensity; (d) frequency dependence of phase.	30
18	Pictorial illustration of how a range-reference plane produces the range-resolved laser radar cross section.	44
19	Schematic of optical system.	47

## LIST OF ILLUSTRATIONS (Continued)

Figure No.		Page
20	Speckle intensity versus laser frequency. These plots illustrate that the statistical properties of the fluctuating speckle intensity are related to the size and the shape of the illuminated object. As the illuminated range extent $L$ increases, the decorrelation frequency $c/(2L)$ decreases. The spectral makeup of the curves depends on the shape of the object.	50
21	Triconic target model and corresponding theoretical range-resolved laser radar cross section for nose-on illumination.	51
22	Estimated spectral density of the fluctuating speckle intensity produced by illuminating a 10-cm-long triconic target nose-on with a frequency-scanning laser: (a) 1 average; (b) 10 averages; (c) 100 averages; (d) 1024 averages. These curves illustrate the smoothing effect of averaging the individual spectral-density estimates obtained from multiple pixels in the CCD array.	53
23	Comparison of the averaged spectral density displayed in Figure 22(d) with the autocorrelation function of the theoretical range-resolved laser radar cross section. Radial falloff in the intensity of the illuminating beam and non-Lambertian scattering from the surface of the triconic are accounted for in the theoretical curve.	54
24	A spherical target mounted in front of a range-reference ring. This type of setup provides a simple means for direct measurement of the range-resolved laser radar cross section.	56
25	Experimental and theoretical range-resolved laser radar cross section for off-axis illumination of a cone at $45^\circ$ . The cone has a length of 2.5 cm and a cone half-angle of $15^\circ$ .	57
26	Experimental and theoretical range-resolved laser radar cross section for off-axis illumination of a cylinder at $35^\circ$ . The cylinder has a length of 2.5 cm and a diameter of 1 cm.	58
27	Demonstration of submillimeter range resolution: (a) nine-step range-resolution target mounted in front of a range-reference ring; (b) experimentally measured range-resolved laser radar cross section. The step size increases by a factor of 1.4 between steps, beginning with a smallest step size of 0.5 mm.	59
28	Reconstructions of the range-resolved laser radar cross section of a triconic target by using bispectral analysis of the speckle intensity: (a) simulated data; (b) measured data. The smooth line in part a represents the theoretical curve.	60

## LIST OF ILLUSTRATIONS (Continued)

Figure No.		Page
29	Measured range-resolved laser radar cross section of a sphere for two different surface materials: (a) 3M 7210 retroreflective paint; (b) Krylon 1402 heat-resistant paint; (c) theoretical result for a Lambertian surface. Each value of range $z$ on the sphere corresponds to a unique value of the angle of incidence $\theta$ , which allows $f(\theta)$ to be measured.	61
30	Range-resolved laser radar cross section of a triconic target illuminated at various aspect angles $\alpha$ : (a) target dimensions; (b) $\alpha = 0^\circ$ ; (c) $\alpha = 65^\circ$ ; (d) $\alpha = 70^\circ$ ; (e) $\alpha = 90^\circ$ ; (f) $\alpha = 180^\circ$ .	64
31	Coordinate system for the analysis of 3D imaging showing the source point $P_s$ , scattering point $P_h$ , reference point $P_r$ , and observation point $P_d$ .	67
32	Interpretation of the 3D Fourier transform of a speckle-pattern-sampling data set: (a) object scene; (b) components in image space representing the 3D Fourier transform of the four terms in Eq. (110).	71
33	Ewald-sphere construction for the sampling of a scattering object's 3D Fourier space. Constant $\lambda$ contours lie on the surface of the Ewald sphere of reflection. The limiting sphere is obtained by varying the illumination direction.	73
34	Cross-range-resolved image of nine-step target with three masked steps: (a) object scene consisting of target and reference point being illuminated into the page; and (b) image obtained from 2D Fourier transform of single speckle frame.	88
35	3D image of nine-step target obtained by speckle-pattern-sampling technique. Range resolution and cross-range resolution are obtained from the wavelength dependence and the spatial dependence of the speckle pattern, respectively.	89
36	3D image of five-step target demonstrating a range resolution of better than $10 \mu\text{m}$ . The step sizes vary from $25 \mu\text{m}$ for the top step to $125 \mu\text{m}$ for the bottom step.	91
37	3D image of a 50-mm-long triconic obtained by the speckle-pattern-sampling technique.	92
38	Remote angle-of-incidence measurements for a flat plate being illuminated by a tunable laser at various angles. As the laser frequency offset $\Delta \nu$ increases, the speckle pattern shifts from the original position. The magnitude $\rho$ of the shift increases with angle of incidence.	95
39	Illustration of the shift-intersection concept for recovering the 3D image from the support of the autocorrelation function.	99

## LIST OF ILLUSTRATIONS (Continued)

Figure No.		Page
40	Photograph of a 25-point scattering array used to demonstrate the shift-intersection concept for 3D phase retrieval.	104
41	Conceptual diagram for reference-plane implementation of image-speckle technique.	106
42	3D image of firing-pin indentation on a cartridge casing obtained using the reference-plane implementation of the image-speckle technique.	107
43	Coordinate system for the two-source-point implementation of 3D imaging using the image-speckle technique.	109
44	3D measurement of a triconic using the two-source-point implementation of the image-speckle technique.	111
A-1	Measured $f(\theta)$ : (a) Newport HC-560 retroreflective paint; (b) Newport HC-563 white diffuse paint; (c) alodined aluminum; and (d) Krylon 1402 heat-resistant paint.	116

# 1. INTRODUCTION

This report deals with applications of tunable lasers to remote sensing of scattering objects with opaque diffuse surfaces. The objective is to extract information about the size, shape, and surface properties of the scattering object by observing variations of the radiation pattern caused by changing the laser frequency. In these applications the object is flood-illuminated by the laser beam. Because the illumination beam is coherent and the surface of the scattering object is rough on the scale of a wavelength of light, large phase irregularities occur in the scattered light coming from different scattering regions on the surface. Interference among the various contributions to the optical field produces a speckle pattern of bright and dark regions of intensity in the radiation pattern. As the laser is scanned in frequency, this speckle pattern appears to boil and decorrelates from the original pattern. This report investigates how this wavelength-dependent speckle pattern is related to the scattering object and demonstrates techniques for extracting information from the speckle pattern about the physical properties of the scattering object. Atmospheric turbulence effects are not treated here.

Researchers have recognized for many years that the wavelength dependence of scattered electromagnetic radiation carries information about the physical properties of the scattering object. In the field of crystallography, it was realized early that the 3D Fourier-transform space of a crystal lattice can be accessed through X-ray diffraction [1]. For a given direction of incidence and a given wavelength, the region of Fourier space being accessed lies on the surface of a sphere known as the Ewald sphere of reflection [2-4]. The Ewald sphere is offset in Fourier space in the direction of the incident beam so that one point on the surface of the sphere touches the origin of Fourier space. Varying the wavelength changes the radius of the sphere and varying the angle of incidence changes the offset direction of the sphere, so it is possible to sample a volume in Fourier space. Wolf appears to have been the first to recognize the connection between the Ewald sphere and optical scattering; he proposed 3D structure determination using holographic data [5,6]. This concept of sampling Fourier space is now well known in the field of inverse scattering [4-10].

With the advent of tunable lasers, the wavelength dependence of speckle became readily observable. George et al. carried out pioneering investigations that related the wavelength-dependent speckle to the scattering object [11-16]. More recently, various imaging techniques based on the wavelength dependence of laser speckle and on tunable laser radars have been proposed and implemented [17-38].

The work being reported here was carried out at MIT Lincoln Laboratory in a laboratory set up in 1990 to investigate applications of speckle in laser radar [31]. Recently, the scope of this work has been broadened to include nondefense-related applications, particularly those involving 3D imaging. Consequently, this report covers techniques motivated by a broad range of applications. One of the techniques developed for 3D imaging is notably similar to that of Marron et al. [33,34].

Section 2 contains background information on the spatial structure of laser speckle. This information is necessary for determining the detector-element size that should be used in a given application. The material contained in Sections 3-5 was developed with laser radar applications in mind. When this research began, laser speckle was generally considered a nuisance in laser radar because it degrades the target images obtained when conventional radar imaging techniques are applied to laser

radars. The short wavelength of laser radars, however, which causes speckle in the first place, actually makes it possible to achieve much higher-resolution images than those obtainable with microwave radars. For example, in this report, laboratory measurements with submillimeter range resolutions are demonstrated by using the extremely large frequency modulations obtainable with a tunable laser. For comparison, the ALCOR K<sub>a</sub>-band imaging radar has a range resolution of 25 cm [39].

The techniques described in Sections 3–5 are based on the wavelength decorrelation of laser speckle. The basic underlying quantity in these sections is the range-resolved laser radar cross section  $U(z)$  of the object for the particular viewing angle.  $U(z)$  is a natural quantity to consider for a monostatic laser radar, where the transmitter and the receiver are collocated. It is a useful quantity because it indicates how much of the object's total laser radar cross section  $\sigma$  comes from each value of range  $z$ . Thus,  $U(z)$  is rich in information about the object's size, shape, and surface-scattering properties. Section 3 describes mathematically how  $U(z)$  and  $\sigma$  are related to the shape of an object and to its surface-scattering properties. This section also illustrates the calculation of  $\sigma$  and  $U(z)$  for simple geometrical shapes.

Section 4 contains a theoretical treatment of the wavelength dependence of laser speckle. This section takes a statistical approach to the analysis by treating the fluctuations of the speckle intensity caused by scanning the laser frequency as a random process. By calculating the statistical properties, or statistical moments, of this random process, information can be deduced about the physical properties of the scattering object. In reality, the speckle intensity is deterministic in nature and depends on the exact microscopic detail of the surface roughness. Randomness enters this approach because the microscopic surface detail is treated as a random process. In other words, a particular object is thought of as a single realization of an ensemble of realizations of that object that are identical on a macroscopic scale but have microscopic differences in their surface detail. This statistical approach provides smooth estimates of the quantity being measured. Without ensemble averaging, interference between the different scattering cells on the surface causes the estimate to be speckled or to fluctuate widely in value from point to point.

Section 4 begins with a phenomenological discussion of the wavelength dependence of speckle. Next comes a derivation of the fundamental relation between the spectral density of the fluctuating speckle intensity and the autocorrelation function of the range-resolved laser radar cross section of the object. A random-process representation of the speckle signal is then developed to simplify further statistical analysis. Finally, various methods are described for measuring  $U(z)$  rather than just the autocorrelation function of  $U(z)$ .

Section 5 revisits the material introduced in Section 4 from a laboratory point of view and confirms the theoretical results. Some of the potential applications of the wavelength-decorrelation technique in target discrimination are also discussed. Because the measurements presented here are based on the statistical approach described in Section 4, macroscopic properties are measured that are independent of a particular realization of the scattering object. In determining these properties, it is necessary to have a collection of measurements available to represent different realizations of the random process from which to calculate statistical moments. Because in practice an ensemble of objects is not available, other means must be used to produce individual realizations of the speckle intensity. There are various ways of approximating individual realizations, but they all require taking data with respect to an additional parameter that has a small effect on the quantity being measured. For example, in measuring  $U(z)$  the

object can be viewed at slightly different angles, the speckle-pattern intensity can be measured in the neighborhood of the monostatic direction, or a long frequency scan can be segmented into shorter scans.

Section 6 was motivated by applications in advanced manufacturing and dimensional metrology, but the material also has relevance to laser radar. The basic underlying quantity here is the 3D distribution of scatterers, or the 3D image, of the scattering object. The mathematical framework for Section 6 is quite different than that for the earlier material because it is not based on statistics. Therefore, it is not necessary to read the theoretical treatment in Sections 3 and 4 to understand the material on 3D imaging in Section 6.

Section 6 considers two different approaches to 3D imaging that use the wavelength dependence of laser speckle. The first approach is a natural extension of the technique described in Sections 3–5 for measuring  $U(z)$ . As explained previously, one way to obtain an ensemble of realizations for determining  $U(z)$  is to sample the speckle pattern at various locations near the monostatic direction. Because the speckle intensity is measured at more than one location in this method, cross-range information as well as range information is available in the data. To extract both range and cross-range information, one must take into account the pixel location instead of simply using the individual pixels as a means for providing members of an ensemble of realizations that correspond to the monostatic direction. The difficulty with this 3D imaging approach is that some form of coherent detection or phase recovery is necessary to form the 3D image. This technique is attractive, however, for many applications where the object is easily accessible or the distance to the object is small. For these applications the phase information can be obtained by using a reference point located near the object or a reference beam that follows a separate propagation path.

The second approach to 3D imaging relies on the wavelength dependence of laser speckle to provide range information and conventional imaging to provide cross-range information. This technique is also attractive for many applications, but it does have the drawback that conventional imaging limits the depth of field for applications that require high lateral resolutions.

Finally, Section 7 summarizes results and makes recommendations for further development.

## 2 SPATIAL PROPERTIES OF LASER SPECKLE

Because the techniques described in this report are based on observing variations of speckle intensity, it is important to understand the spatial structure of speckle (see Figure 1). First, one needs to know the transverse speckle size along the detector plane to ensure that the detector elements are small enough to sample individual speckle lobes. It is also necessary to understand how quickly the speckle pattern varies longitudinally with changes of distance from the scatterer. This section describes the transverse and longitudinal structure of laser speckle and provides formulas for estimating the transverse and longitudinal speckle sizes.

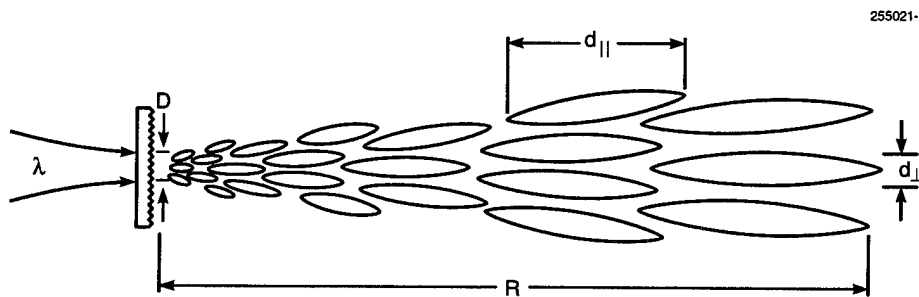


Figure 1. Transverse and longitudinal speckle size.

Let  $d_{\perp}$  denote the average transverse speckle size that would be observed on the interior surface of a sphere of radius  $R$  centered around the scattering object. If  $D$  represents the projected linear size extent of the illuminated portion of the scattering object for a given observation angle, then the average speckle size  $d_{\perp}$  in the direction along which  $D$  is measured is given by  $d_{\perp} = \lambda R/D$ . This relation shows that speckle size is proportional to the wavelength  $\lambda$  and the range  $R$  but inversely proportional to the size  $D$ . Consequently, if the object is elongated in one direction, the speckle is elongated in the other direction, and the statistics of the speckle pattern not only provide a measure of the size of the object but also carry information about its orientation and transverse shape.

Although the spatial structure of speckle depends mainly on the size and shape of the illuminated portion of the scattering surface, it is also affected by factors such as variations of the intensity profile within the illuminating beam and variations in the strength of the return from different regions of the scattering surface. The latter variation is where the microscopic structure of the rough surface enters. The microscopic structure of a rough surface determines the angular distribution of light scattered from the surface [16,40]. Because of this angular dependence, the return strength varies according to the viewing angle for each surface element on the scattering object. Section 3 describes more fully how the angular scattering distribution of the surface material enters speckle calculations.

Figure 2 shows the relation between the speckle shape and the transverse object shape for three different objects. For the triconic, the individual speckles are elongated in the direction perpendicular to the axis of the triconic. For the sphere, the speckles appear to wrap around one another like worms in a bucket. No direction is preferred, and the speckle shape is symmetric on average. For the ring, the borders of the individual speckles appear to be better defined. The average speckle size can be defined mathematically by taking the 2D autocorrelation function of the speckle pattern, which is displayed at the bottom of the figure for the three different objects. (Actually, the average of the autocorrelation is shown for 40 separate realizations of the speckle pattern for each object. The different realizations are obtained by rotating the object slightly.) Note that the autocorrelation function of the elongated speckle from the triconic is also elongated and that the autocorrelation functions of the rotationally symmetric objects are rotationally symmetric.

Let  $d_{\parallel}$  denote the average longitudinal speckle size that would be observed in the radial direction at the distance  $R$ . An expression for  $d_{\parallel}$  in the Fresnel zone is given in the literature [16,41]; namely,  $d_{\parallel} = 4\lambda R^2/D^2$ . Thus, the longitudinal speckle size grows as the square of the distance  $R$  rather than linearly with  $R$ , so there is a rapid elongation of the speckles with distance. Once the observation point is in the far field, the intensity of the speckle pattern does not change in the radial direction except for falling off as  $1/R^2$ .

The variation in longitudinal structure is illustrated through the computer-simulated speckle pattern displayed in Figure 3(a). The data are generated by adding the field contributions from a linear array of point-scatterers. The array is  $20\lambda$  in length and the spacing between points is  $\lambda/4$ . The scatterers are randomly phased by using a uniform distribution over  $2\pi$  radians. The intensity is calculated on a square grid by summing the field contributions from the individual point-scatterers and squaring the magnitude. The grid lies in the plane defined by the linear scattering array and the longitudinal direction. The size of the sampled area is  $40\lambda$  in the transverse direction and  $50\lambda$  in the longitudinal direction. For the purpose of visualization, the speckle intensity is normalized by dividing by the ensemble-averaged intensity value at each grid point. This normalization compensates for the decrease in intensity with distance.

Figure 3(a) shows that the dimensions  $d_{\perp}$  and  $d_{\parallel}$  are small at locations near the scatterer but not smaller than the wavelength  $\lambda$ . Also, the rule stating  $d_{\perp}$  is proportional to the range  $R$  appears to apply well into the near field. Note that the speckles rapidly elongate in the radial direction. The transition to the far field occurs at a range of approximately  $R = D^2/\lambda$ . For this example,  $R = 400\lambda$ . Figure 3(b) shows a calculation of the normalized speckle intensity as a function of the logarithm of the distance along a horizontal line passing through the center of the linear scattering array. This curve illustrates the transition to the far field and confirms that the normalized speckle intensity does not fluctuate past this point. Figures 3(c) and 3(d) contain similar curves for radial lines making angles of  $30^\circ$  and  $60^\circ$  with respect to the horizontal axis. The transition to the far field occurs more rapidly at these larger angles because the projected length of the scattering array decreases.

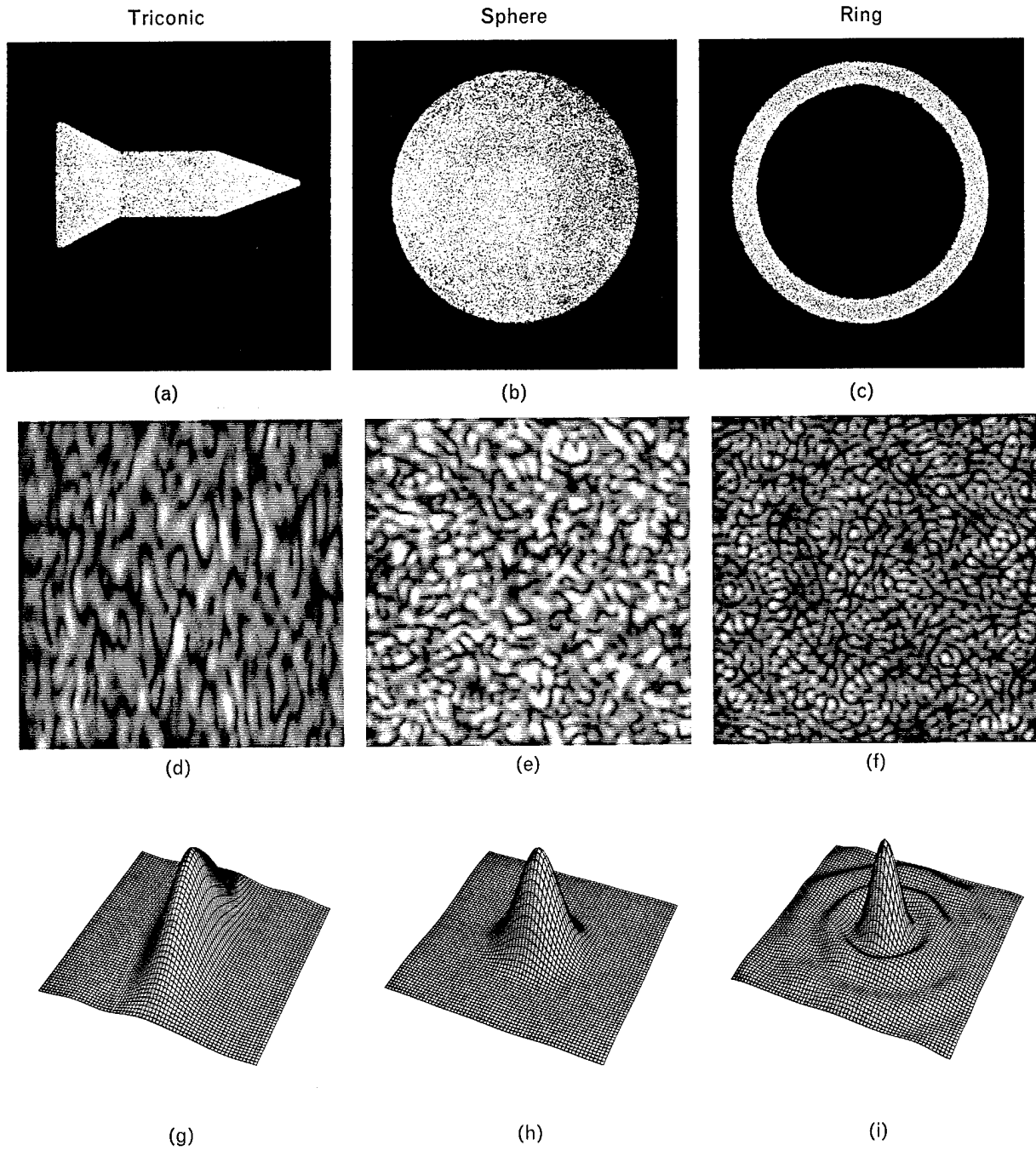


Figure 2. Effect of object shape on speckle patterns: photographs of laser-illuminated (a) 2.5-cm-long triconic, (b) 2.5-cm-diameter sphere, and (c) ring with an outer diameter of 2.5 cm and an inner diameter of 2.0 cm; their corresponding speckle patterns are shown in (d), (e), and (f), respectively; the ensemble-averaged autocorrelation functions (40 averages) of the speckle patterns are shown in (g), (h), and (i), respectively.

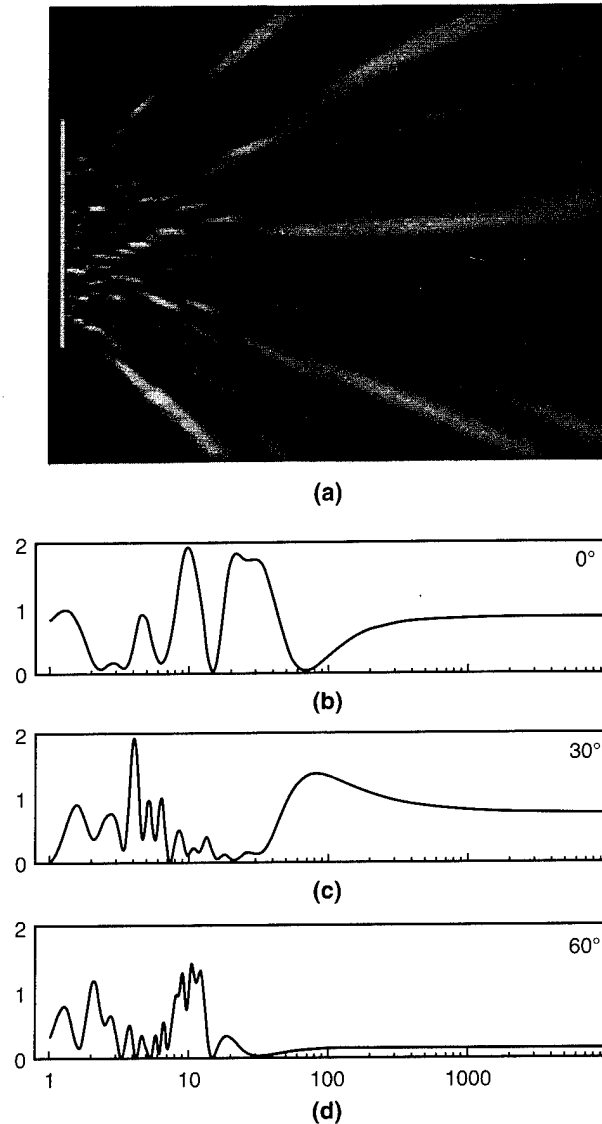
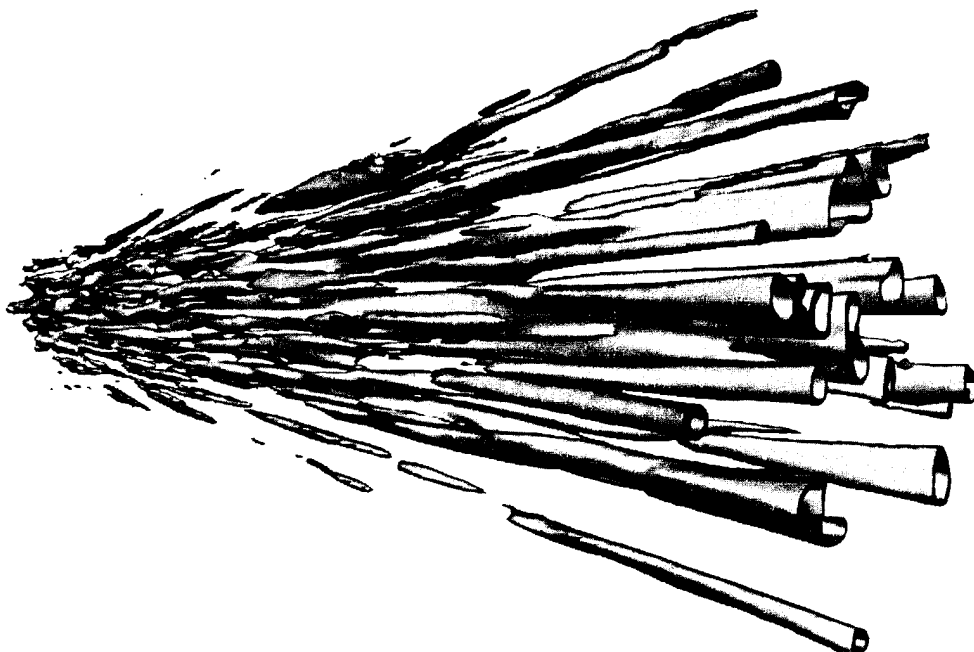


Figure 3. Computer-simulated normalized speckle intensity from a 20-wavelength-long linear array of randomly phased point-scatterers: (a) longitudinal slice of the speckle pattern cutting through the linear array; (b) speckle intensity versus logarithm of distance for a horizontal line lying in the longitudinal slice and beginning at the center of the linear array; (c) speckle intensity along a radial line  $30^\circ$  above the horizontal; (d) speckle intensity along a radial line  $60^\circ$  above the horizontal. The speckle intensity is normalized by dividing by the expected value of the intensity at each point.

To further illustrate the spatial properties of speckle, a 3D measured speckle pattern is shown in Figure 4. This speckle pattern was obtained by back-illuminating a ground-glass diffuser with a focused laser beam from an HeNe laser and sampling the resulting speckle pattern with a CCD array. The CCD

array was translated in the longitudinal direction between frames and the frames combined into a 3D array representing the speckle intensity as a function of position. The conical region containing the speckle pattern is  $300 \mu\text{m}$  in length and its diameter increases from  $25 \mu\text{m}$  to  $100 \mu\text{m}$ . In acquiring the data, it was necessary to use a microscope objective to magnify the speckle and to image the plane of interest onto the CCD array. To more easily visualize the speckle pattern in three dimensions, the intensity was normalized (as in Figure 3) and a threshold function applied to convert the speckles to solid objects. As expected, the transverse speckle size increases linearly with radial distance, and the speckle rapidly elongates with distance.

253955-3L



*Figure 4. Measured 3D speckle pattern from a ground-glass diffuser back-illuminated by a  $25\text{-}\mu\text{m}$ -diameter  $0.633\text{-}\mu\text{m}$ -wavelength HeNe laser spot. This image was formed by stacking a series of 150 CCD images of the speckle pattern, with a longitudinal displacement of  $2 \mu\text{m}$  between frames.*

In these two examples, the transverse size  $D$  of the scatterer was chosen to be small so that a small number of speckles would be present for visualization purposes. [Observe that approximately  $D/\lambda = 20$  speckles are at a given value of range in Figure 3(a). Thus,  $(D/\lambda)^2$  is the approximate number of speckles associated with a scatterer.] Let us estimate the speckle size for other situations. In a typical laboratory setup with  $D = 5 \text{ cm}$ ,  $R = 2 \text{ m}$ , and  $\lambda = 0.75 \mu\text{m}$ , the average transverse speckle size at the receiver plane is  $d_{\perp} = 30 \mu\text{m}$ , which matches well with the pixel size of a typical CCD detector. This range is still not in the far field, which occurs at  $R = 3300 \text{ m}$ . Therefore, the speckle is still fluctuating in the radial direction

and the longitudinal speckle size is  $d_{\parallel} = 4.8$  mm. This relatively slow variation of the speckle pattern with  $R$  allows the methods described in the following sections to be applied to objects with longitudinal motion components. In a space-based application, typical parameters might be  $D = 1$  m,  $R = 100$  km, and  $\lambda = 1$   $\mu$ m, which yields a transverse speckle size of  $d_{\perp} = 10$  cm. The far-zone transition for this set of parameters occurs at approximately  $R = 1000$  km, and the longitudinal speckle size at  $R = 100$  km is  $d_{\parallel} = 40$  km.

### 3. LASER RADAR CROSS SECTION AND RANGE-RESOLVED LASER RADAR CROSS SECTION

This section describes the basic relations involved in the calculation of an object's laser radar cross section  $\sigma$  and its range-resolved laser radar cross section  $U(z)$ . These quantities are fundamentally important in understanding and interpreting radar signatures. The laser radar cross section  $\sigma$  indicates the strength of the return signal, whereas the range-resolved laser radar cross section  $U(z)$  indicates how much of the return signal comes from each value of range  $z$ . Therefore,  $U(z)$  contains information about the size, shape, and surface-scattering properties of the object. Because  $U(z)$  can be measured by the wavelength-decorrelation method, the interest lies in relating it to the physical properties of a target. The following builds a theoretical framework and points out similarities in the methodology for calculating  $U(z)$  and  $\sigma$ . This methodology is then applied to the calculation of  $U(z)$  and  $\sigma$  for basic geometrical shapes.

#### 3.1 DEFINITIONS

Because of speckle, there is a basic distinction between microwave cross sections and laser radar cross sections. To smooth out the large fluctuations in intensity caused by the speckle, the laser radar cross section is defined as an ensemble-averaged quantity. Hence, the usual microwave-radar expression relating the cross section to the irradiance  $E$  (power per unit area) at the receiver is modified by placing ensemble-average brackets around the received irradiance

$$\sigma = 4\pi R^2 \frac{\langle E \rangle}{E_0} \quad (1)$$

The quantity  $E_0$  in Eq. (1) is the irradiance of the illuminating beam and  $R$  is the distance to the target, as shown in Figure 5. The laser radar cross section  $\sigma$  is interpreted as the cross-sectional area of a hypothetical isotropic scatterer that would produce the same averaged irradiance at the receiver as the actual scatterer. (An isotropic scatterer is one that scatters the incident light uniformly into  $4\pi$  steradians.)

Because the laser wavelength is small compared to the object size and to any feature of interest on the object, the scattering can be treated as a localized phenomenon, which simplifies the calculation of  $\sigma$ . In addition, because  $\sigma$  is defined as an ensemble-averaged quantity and because the surface is rough on a wavelength scale, the interference between the contributions arising from different regions of the surface averages out. Therefore,  $\sigma$  is obtainable by incoherently summing the contributions arising from individual surface patches.

The range-resolved laser radar cross section  $U(z)$  is also an ensemble-averaged quantity. Because  $\sigma$  is the incoherent sum of individual localized contributions,  $U(z)$  can be defined as the derivative of the laser radar cross section  $\sigma$  with respect to range:

$$U(z) = \frac{d\sigma}{dz} \quad (2)$$

Thus,  $U(z)$  is a density function that quantifies the contributions to the cross section as a function of range. Integrating  $U(z)$  over the entire range extent of the object yields  $\sigma$ . Both  $\sigma$  and  $U(z)$  are nonnegative functions;  $U(z)$  can be infinite at isolated points, as long as the integrated area under the curve is finite. Because  $\sigma$  has dimensions of area,  $U(z)$  has dimensions of length. Both quantities depend on the viewing angle.

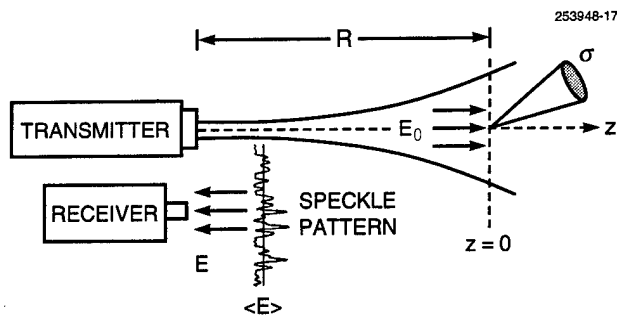


Figure 5. The coordinate system used to define laser radar cross section and range-resolved laser radar cross section.

### 3.2 METHOD OF CALCULATION

Two physical properties of the object affect  $\sigma$  and  $U(z)$ : the shape of the object and the angular-scattering distribution of its surface materials. The shape of the object is characterized by the function  $h_{||}(x, y)$ , which represents the height of the object boundaries above the  $z = 0$  plane as a function of the Cartesian coordinates  $x$  and  $y$  lying in this plane. Hence, this height function is measured along the direction of illumination and increases with distance from the source. If the function is multivalued, then the smallest value is used because it corresponds to the point closest to the source; the other values are associated with points that are shadowed by the closest point.

The standard radiometric quantity for specifying the angular-scattering distribution is the bidirectional reflectance distribution function (BRDF) [42,43]. The BRDF describes the scattering of light from a flat surface element as a function of both the illumination direction and the observation direction. Knowledge of the full BRDF is not necessary in our situation, however, because a monostatic radar configuration has been assumed. Instead, the monostatic reflectance distribution function  $f(\theta)$  can be used, which is a subset of the BRDF obtained by setting illumination and observation angles equal. [Writing  $f(\theta)$  assumes no preferred azimuthal axis so that the monostatic reflectance distribution function depends only the local angle of incidence  $\theta$ , defined as the angle between the normal vector to the surface and the direction of illumination.] The angle of incidence  $\theta$  varies with position on the surface and is related to the height function  $h_{||}(x, y)$  through

$$\cos\theta = \pm \frac{1}{\sqrt{h_{1,x}^2 + h_{1,y}^2 + 1}} \quad , \quad (3)$$

where the subscripts  $x$  and  $y$  denote partial derivatives of the height function with respect to these variables. The plus sign is chosen if the surface element points toward the source, and the minus sign is chosen if the surface element points away from the source.

The cross section  $\sigma$  is evaluated by incoherently summing the contributions arising from individual surface elements. If  $dA$  is the area of a given surface element, then the associated contribution to the cross section is

$$d\sigma = 4\pi f(\theta) \cos^2\theta dA \quad . \quad (4)$$

This result follows from the definition of cross section and the definition of the BRDF. One of the cosine factors arises from the illumination obliquity factor; the other is associated with the decreased projected area of the element as seen by the detector. The total cross section is obtained by integrating over the entire illuminated surface area. There are two conditions under which a surface patch will not be illuminated: (1) if its surface normal points away from the source, which occurs when  $\cos\theta < 0$ , or (2) if it is shadowed by some other region of the object. The second condition occurs when  $h_{1i}$  is multivalued and the given surface patch does not correspond to the lowest value of  $h_{1i}$ . If the object is convex, then all shadowing can be accounted for by applying the  $\cos\theta < 0$  rule.

In our situation, it is more convenient to perform the integration over the projected area  $A_{\perp}$  along the line of sight. If the surface-area differential  $dA$  is written in terms of  $dA_{\perp} = dx dy = dA \cos\theta$ , then one of the cosine factors is eliminated. Summing over the projected area  $A_{\perp}$  of the object results in

$$\sigma = 4\pi \iint_{A_{\perp}} f(\theta) \cos\theta dx dy \quad (5)$$

as the cross section for the particular viewing angle.

The assumptions that go into the derivation of Eq. (5) limit its use to the calculation of  $\sigma$  for diffusely scattering objects that are large in size compared to the optical wavelength. Contributions to the cross section arising from specular scattering points can be accounted for separately. In addition, interactions between different surface elements, such as multiple scattering, are not accounted for. Polarization effects are also ignored in Eq. (5), but they could be included by defining a polarization-dependent  $f(\theta)$  and  $\sigma$ .

The basic formula for calculating  $U(z)$  is similar in appearance to Eq. (5). The only difference is the inclusion of a  $\delta$ -function within the integral to limit the region of integration to the specified value of range  $z$ :

$$U(z) = 4\pi \iint_{A_{\perp}} f(\theta) \cos\theta \delta[z - h_{1i}(x, y)] dx dy \quad . \quad (6)$$

Figure 6 illustrates how the  $\delta$ -function reduces the region of integration to the contour formed by the intersection of the range plane with the boundary of the object. Equation (6) can be validated by substituting it into Eq. (2), which yields Eq. (5) for  $\sigma$ .

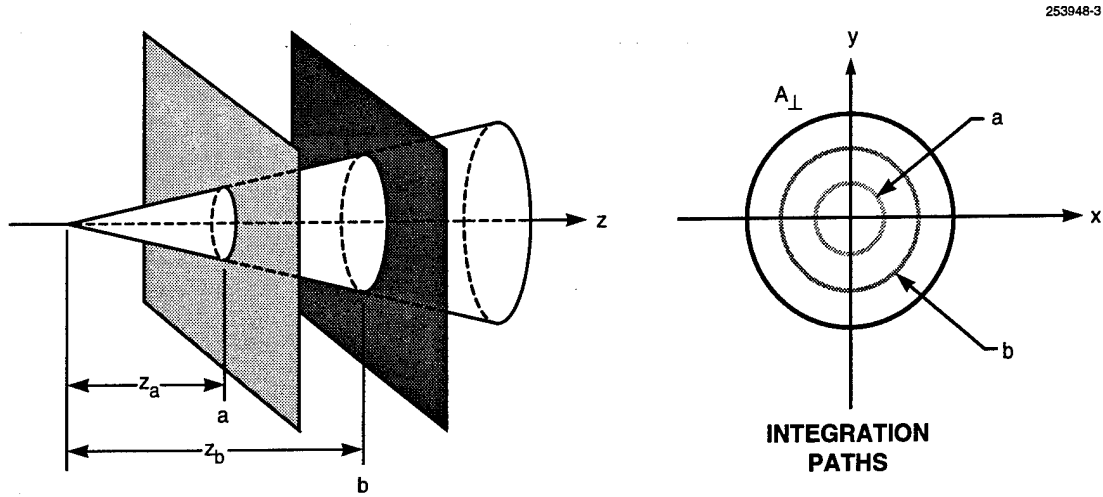


Figure 6. Circularly shaped integration paths for calculating the range-resolved laser radar cross section  $U(z)$  for a cone illuminated on axis.

To further illustrate the meaning of Eq. (6), consider two special cases. In the first case, suppose that the scattering object is a flat plate of area  $A$  that is illuminated at normal incidence. Then the height function is constant (say  $z_0$ ) on this plate, and the object's total cross section is confined to one value of range, that is,  $z = z_0$ . Equation (6) is easily evaluated in this case; the  $\delta$ -function does not depend on the variables of integration and can be removed from the integral, which leaves

$$U(z) = \sigma \delta(z - z_0) \quad , \quad (7)$$

where  $\sigma = 4\pi f(0)A$  is the laser radar cross section of the plate.

In the second case, exclude any situations covered by Eq. (7). Then Eq. (6) reduces to a line integral around the contour associated with the given height value of  $z$ . This line integral is obtained by changing variables from  $x$  and  $y$  to  $z$  and  $l$ , where  $l$  is the distance along the integration path. Then  $dx dy = \cot \theta dl dz$ , and the range integration can be performed by applying the  $\delta$ -function, which leaves

$$U(z) = 4\pi \int_{\text{contour}} f(\theta) \cos \theta \cot \theta dl \quad . \quad (8)$$

Because the height function may have multiple peaks and valleys, more than one contour line may exist for a given value of  $z$ .

### 3.3 ON-AXIS ILLUMINATION

The calculation of  $\sigma$  and  $U(z)$  for on-axis illumination of axially symmetric objects will now be illustrated. Although these calculations are among the simplest to carry out, the results are important because they apply to a number of common situations and because they illustrate the general behavior of  $\sigma$  and  $U(z)$ . Consider the laser radar cross section first. In radar measurements the radar is calibrated by using a standard target with a known cross section. The calibration standard for laser radars is typically either a diffuse disk illuminated at normal incidence or a diffuse sphere. Ideally, the surface of the calibration target is Lambertian, which corresponds to an angle-independent  $f(\theta)$  of value  $f = 1/\pi$ .

As calibration standards, the numerical values of  $\sigma$  for Lambertian spheres and Lambertian disks have special significance. The laser radar cross section of a Lambertian sphere is 8/3 times its projected geometrical cross section. Compare this value to that of the conventional radar cross section of a smooth, perfectly conducting sphere as calculated in the short-wavelength, physical-optics limit [44]; in this situation the cross section is equal to the geometrical cross section of the sphere. The conventional radar cross section of a smooth sphere can be attributed to the neighborhood of the specular point, whereas the laser radar cross section of a diffuse sphere is composed of contributions from the entire illuminated hemisphere. Distinguishing between laser radar cross section and conventional radar cross section stresses the point that it is not necessary to take the ensemble average when the surface of the object is smooth. The laser radar cross section and the conventional radar cross section, however, are equal in this situation, and no further distinction between the two will be made in the remainder of this discussion.

A Lambertian disk viewed at normal incidence has a laser radar cross section equal to four times its area  $A$ . But the laser radar cross section of a smooth, perfectly conducting disk at normal incidence depends on the wavelength  $\lambda$  through the relation  $\sigma = 4\pi A^2/\lambda^2$ . This strong wavelength dependence is caused by coherent addition of the specular reflections from the entire surface area of the disk.

The surfaces of a sphere and a disk are examples of two different classes of surfaces, namely, those having curvature in two dimensions and those having no curvature in either dimension. The surface of a cylinder is an example of an intermediate category; its surface has curvature in a single dimension. When viewing a smooth, perfectly conducting cylinder normal to its axis, there is a straight line on the surface where specular reflections occur. The coherent addition of these specular contributions produces a laser radar cross section that is inversely proportional to wavelength; that is,  $\sigma = 2\pi aL^2/\lambda$ , where  $a$  is the radius of the cylinder and  $L$  is its length. Contrast this relation with the wavelength-independent result that  $\sigma = 2\pi aL$  for a Lambertian cylinder viewed normal to its axis. In summary of these three situations, except for possible variations of  $f(\theta)$  with wavelength, the laser radar cross section of a diffuse object is independent of the wavelength, but the laser radar cross section of a smooth-surfaced object can exhibit a strong wavelength dependence for those viewing angles where there is coherent addition of specular components.

Now some elementary calculations of the range-resolved laser radar cross section are illustrated for axially symmetric objects that are viewed along the axis of symmetry. In these calculations Eq. (8) reduces to a simple form, derived by representing the object by a radius function  $r(z)$ . If  $r(z)$  increases monotonically, then each value of  $z$  maps into a single value of the angle of incidence  $\theta$ . Therefore, the quantities that depend on  $\theta$  can be removed from the integral, and the integration in Eq. (8) simply results

in the circumference  $2\pi r(z)$  of the object for the given range value. Consequently, for axially symmetric objects illuminated along the axis of symmetry, Eq. (8) takes the form

$$U(z) = 8\pi^2 r(z) f(\theta) \cos \theta \cot \theta \quad (9)$$

The angle of incidence  $\theta$  is related to the radius function  $r(z)$  by  $\cot \theta = dr/dz$ . If  $r(z)$  is not a monotonic function, then for certain ranges  $z$  there will be more than one value of  $r$  corresponding to  $z$ . If this is the case, the contributions from the different solutions are summed.

Let us apply Eq. (9) to the case of a cone viewed on axis. For a cone half-angle  $\alpha_c$ , a cone length equal to  $L$ , and the tip of the cone located at  $z = 0$ ,

$$U(z) = 8\pi^2 \sin \alpha_c \tan^2 \alpha_c f(\pi/2 - \alpha_c) z \quad \text{for } 0 \leq z \leq L \quad (10)$$

is obtained. Note that the range-resolved laser radar cross section of the cone increases linearly with range, regardless of the functional form of  $f(\theta)$ . This result is intuitive because the angle of incidence is constant and the circumference of the cone is proportional to  $z$ .

Equation (9) can also be applied to the calculation of the range-resolved laser radar cross section of a sphere. If the sphere has radius  $a$  and is located with its center at  $z = 0$ , then

$$U(z) = \frac{8\pi^2}{a} f[\cos^{-1}(-z/a)] z^2 \quad \text{for } -a \leq z \leq 0 \quad (11)$$

Observe that  $U(z)$  is a segment of a parabola when the surface of the sphere is Lambertian. The parabola has a maximum value of  $8\pi a$  at the pole where  $z = -a$  and falls to zero at the equator where  $z = 0$ . Interestingly, the on-axis cone and the Lambertian sphere have range-resolved laser radar cross sections that are linear and quadratic in range, respectively. Figure 7 contains plots of  $U(z)$  for a top hat and a cone, each viewed on axis, and a Lambertian sphere. These plots illustrate Eqs. (7), (10), and (11), respectively.

### 3.4 OFF-AXIS ILLUMINATION

The cross section  $\sigma$  and range-resolved laser radar cross section  $U(z)$  vary markedly with viewing angle. This angular dependence can produce distinctive signatures that are useful for identifying and characterizing objects; the capability to predict these signatures can aid in their interpretation. This section introduces methods for calculating the angular dependence of  $\sigma$  and  $U(z)$ .

Although Eq. (5) for calculating  $\sigma$  and Eq. (6) for calculating  $U(z)$  are general results, they are difficult to apply to angle-dependent problems because the functional form of  $h_{\eta}$  also depends on the aspect angle. Therefore, applying these results requires the appropriate height function of an object for each aspect angle. This difficulty is avoided by performing the integration in a rotated coordinate system  $(\xi, \eta, \zeta)$  that is natural (or preferred) for defining the object shape. Let us denote the height function in this new coordinate system by  $h(\xi, \eta)$  (see Figure 8). If there is an axis of symmetry, it is usually aligned with the  $\zeta$ -axis.

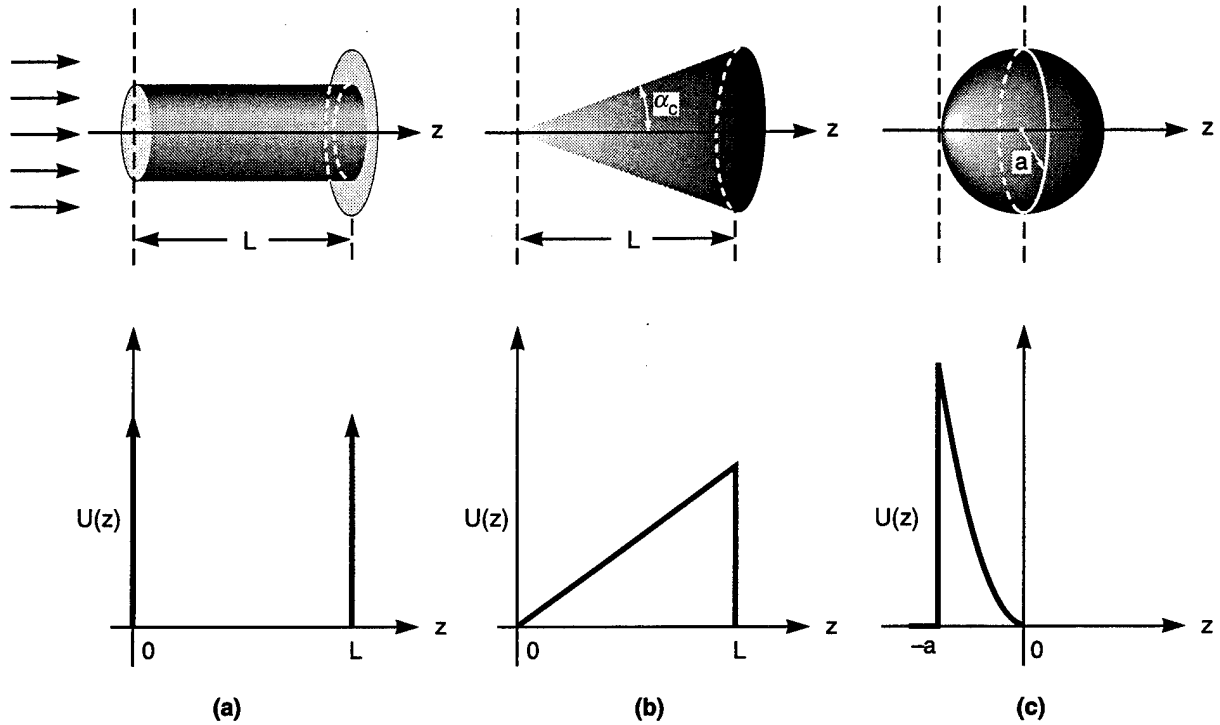


Figure 7. Range-resolved laser radar cross sections for on-axis viewing: (a) top hat; (b) cone; (c) Lambertian sphere.

In the rotated coordinate system the height function remains constant and the illumination direction varies. Let  $\alpha$  and  $\beta$  be the polar and azimuthal angles representing the direction of illumination, as illustrated in Figure 8. ( $\alpha$  is commonly referred to as the aspect angle for axially symmetric objects.) Then the expression analogous to Eq. (3) for calculating the angle of incidence  $\theta$  in terms of the new height function is

$$\cos\theta = \frac{\cos\alpha - \sin\alpha(h\xi\cos\beta + h\eta\sin\beta)}{\sqrt{h_\xi^2 + h_\eta^2 + 1}} \quad (12)$$

Note that Eq. (12) reduces to Eq. (3) when  $\alpha = 0$ .

The expression for  $\sigma$  in the rotated coordinate system is obtained by changing the variables of integration from  $x$  and  $y$  to  $\xi$  and  $\eta$  in Eq. (5), yielding

$$\sigma = 4\pi \iint_{A_h} f(\theta) \cos^2\theta \sqrt{h_\xi^2 + h_\eta^2 + 1} d\xi d\eta \quad (13)$$

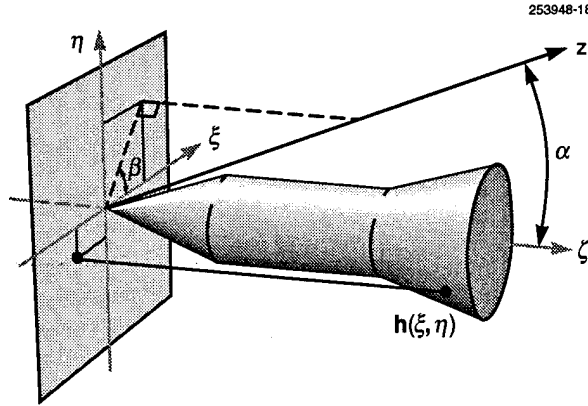


Figure 8. Coordinate system for describing the object height function  $h(\xi, \eta)$  and the direction of illumination  $(\alpha, \beta)$ .

The region of integration  $A_h$  corresponds to the projection of the illuminated surface area onto the  $\xi$ - $\eta$  plane (as depicted in Figure 9 for a cone). Observe that Eq. (13) simplifies to Eq. (5) when  $\alpha = 0$ . There is one complication in using Eq. (13) that does not arise in Eq. (5). In Eq. (5) shadowing is accounted for by retaining only the lowest value of  $h_i$  if it is multivalued. When using Eq. (13), it is necessary to separately determine when the old height function  $h_i$  for the given aspect angle is multivalued.

A similar integral exists for the range-resolved laser radar cross section. In the rotated coordinate system, Eq. (6) takes the form

$$U(z) = 4\pi \iint_{A_h} f(\theta) \cos^2 \theta \sqrt{h_\xi^2 + h_\eta^2 + 1} \times \delta[z - h(\xi, \eta) \cos \alpha - \sin \alpha (\xi \cos \beta + \eta \sin \beta)] d\xi d\eta \quad (14)$$

Again, the advantage of this form is that the height function  $h$  is independent of aspect angle. As expected, Eq. (14) reduces to Eq. (6) when  $\alpha = 0$ . Note that Eq. (14) is identical to Eq. (13), except for the inclusion of the  $\delta$ -function, which limits the integration to the contour formed by the intersection of the object boundary with the range plane. Note also that setting the argument of the  $\delta$ -function to zero provides the formula that describes the integration path.

Equations (13) and (14) can be difficult to evaluate analytically. Closed-form solutions can be found for many simple shapes, however, and these solutions aid in the prediction and interpretation of target signatures. Because complex objects can usually be described as a combination of simple component shapes, the analysis of simple components should be carried as far as possible. As long as cross-shadowing of one component by another is accounted for, the results determined for individual components can be used in modeling more complex object shapes.

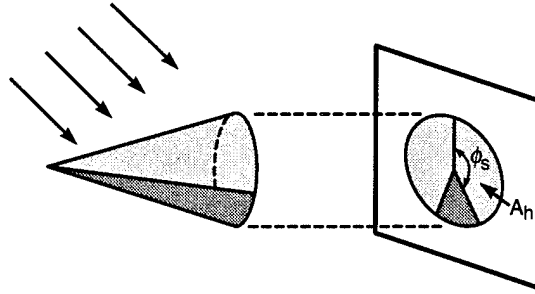


Figure 9. Region of integration for calculating the laser radar cross section for off-axis illumination of a cone. As the aspect angle increases, the angular range of integration  $\pm\phi_s$  in the projection plane decreases. This range of integration corresponds to the illuminated surface area of the cone.

Many component shapes have some form of symmetry. The remainder of this section considers off-axis illumination of the class of objects that are symmetric around an axis of rotation. One can characterize these objects by a height function  $h(r)$  that depends only on the radius  $r$ . Some important members of this class, including spheres, disks, cylinders, and cones, are treated below.

Let us first consider the laser radar cross section  $\sigma$ . Because the sphere is radially symmetric,  $\sigma$  is independent of aspect angle as long as the material covering the sphere is applied uniformly. Most other objects, however, exhibit a strong angular dependence in their cross section. For example, by Eq. (13), the cross section of a disk or any other flat object falls off as  $\cos^2\theta$ , not including any variations caused by  $f(\theta)$ . The Lambertian cylinder also has a simple dependence on aspect angle. Let the radius of the cylinder be denoted by  $a$  and the length by  $L$ . If the aspect angle  $\alpha$  is measured relative to the cylinder axis, then the cross section  $\sigma$  is given by  $2\pi aL \sin^2\alpha$ , not including contributions from end caps. The aspect-angle dependence of  $\sigma$  for a Lambertian cone is not as simple [30,45]. If  $\alpha_c$  is the half-cone angle,  $\alpha$  is the aspect angle relative to the axis of symmetry, and  $a$  is the radius at the base, then

$$\sigma = \begin{cases} 2\pi A_1 & \alpha \leq \alpha_c \\ A_1 \left[ \pi + 2 \sin^{-1} \left( \frac{\tan \alpha_c}{\tan \alpha} \right) \right] + 2A_2 & \alpha_c < \alpha < \pi - \alpha_c \\ 0 & \pi - \alpha_c \leq \alpha \leq \pi \end{cases} \quad (15)$$

where

$$A_1 = \frac{a^2}{\sin \alpha_c} (\sin^2 \alpha \cos^2 \alpha_c + 2 \cos^2 \alpha \sin^2 \alpha_c) \quad (16)$$

and

$$A_2 = 3a^2 \sin \alpha \cos \alpha \cos \alpha_c \sqrt{1 - \frac{\tan^2 \alpha_c}{\tan^2 \alpha}} \quad (17)$$

The cross section of a cone with a disk base would include a contribution from the disk for  $\pi/2 < \alpha \leq \pi$ . Figure 10 illustrates this angle dependence for a Lambertian cone with a Lambertian disk base.

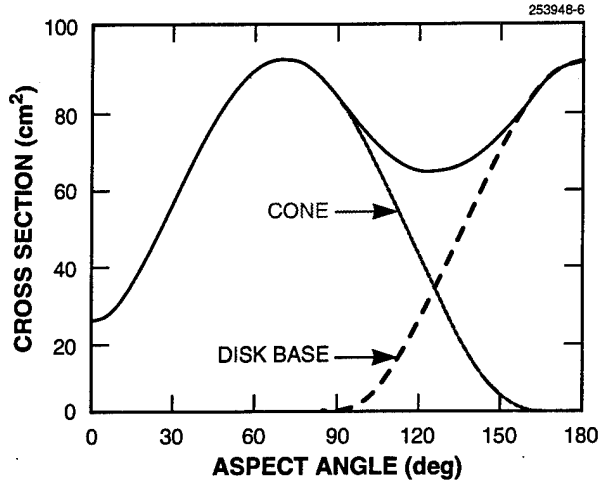


Figure 10. Aspect-angle dependence of the laser radar cross section of a 10-cm-long Lambertian cone with a cone half-angle of  $15^\circ$ . The separate contributions from the cone and the disk base are indicated.

Next, consider the range-resolved laser radar cross section  $U(z)$ . In general,  $U(z)$  is more difficult to calculate than  $\sigma$ , but the solutions for  $U(z)$  tend to be more interesting because of the dependence on range. A specialized form of Eq. (14) results when the object is axially symmetric. The steps involved in determining this form are (1) transforming the integral to polar coordinates  $r$  and  $\phi$ , (2) converting the  $\delta$ -function to an explicit function of  $r$ , and (3) performing the radial integration via the  $\delta$ -function. The result does not depend on  $\beta$ . Setting  $\beta = 180^\circ$  centers the range of integration around  $\phi = 0$ , which yields

$$U(z) = 8\pi \int_{\phi} \sum_i f(\theta) \cos^2 \theta \frac{r_i \sqrt{1 + h_r^2}}{|h_r \cos \alpha - \sin \alpha \cos \phi|} d\phi \quad (18)$$

Equation (18) requires some clarification. First, let us consider the meaning of the summation: For given values of azimuth angle  $\phi$ , range  $z$ , and aspect angle  $\alpha$ , more than one value of the radius  $r$  can lie on the integration path. These values of  $r$  correspond to the discrete solutions  $r_i$  of the integration-path equation

$$z = -r_i \sin \alpha \cos \phi + \cos \alpha h(r_i) \quad (19)$$

Each solution contributes to  $U(z)$ ; hence, the summation in Eq. (18). The symbol  $h_r$  in Eq. (18) denotes the derivative of  $h(r)$  with respect to  $r$ , evaluated at the point  $r = r_i$ .

The integration in Eq. (18) extends over values of the azimuth angle  $\phi$  ranging between 0 to  $\pi$  such that all of the following conditions are satisfied: (1) a solution to Eq. (19) exists, which implies that the range plane intersects the object; (2)  $\cos \theta > 0$ , which implies that the surface element faces the source; and (3) only the lowest-valued branch of the corresponding function  $h_1$  is taken when it is multivalued, which implies that the point is not shadowed by a point closer to the source. Integration over azimuth angles between  $\pi$  and 0 has been accounted for in Eq. (18) by using symmetry and doubling the result.

The formula for the angle of incidence  $\theta$  given in Eq. (12) reduces to

$$\cos \theta = \frac{h_r \sin \alpha \cos \phi + \cos \alpha}{\sqrt{1 + h_r^2}} \quad (20)$$

for axial symmetry. Equations (18)≡(20) provide the basic framework for calculating the angular dependence of the range-resolved laser radar cross section for axially symmetric objects. In the following sections, these results are used to write solutions for the aspect-angle dependence of  $U(z)$  for disks, cones, cylinders, and truncated spheres.

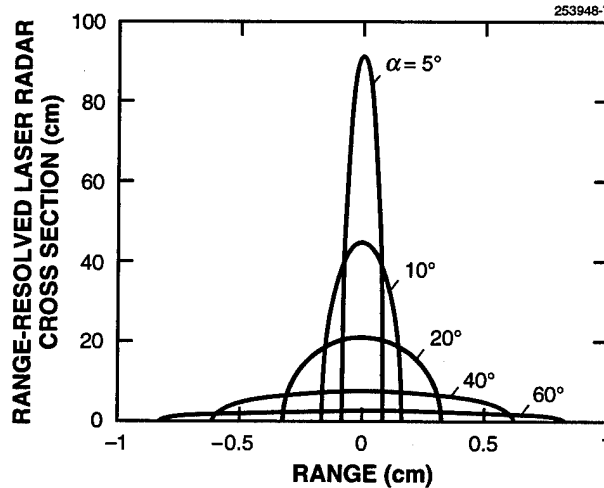


Figure 11. Range-resolved laser radar cross section of a 1-cm-radius Lambertian disk at various illumination angles.

### 3.4.1 Disk

Let a disk of radius  $a$  be positioned with its center at the origin. It is relatively simple to apply Eq. (18) to this situation because the height function has a constant value; namely,  $h(r) = 0$ . Consequently, there are no shadow boundaries to contend with, and the integration path is a straight line. The azimuthal

range of integration is determined by setting  $r_i = a$  in Eq. (19) and solving for  $\phi$ . The resulting form for  $U(z)$  is elliptical in shape:

$$U(z) = 8\pi f(\alpha) \cot^2 \alpha \sqrt{a^2 \sin^2 \alpha - z^2} \quad \text{for } |z| \leq |a \sin \alpha| \quad (21)$$

This result is intuitive because the range-resolved laser radar cross section of a disk is proportional to the length of the straight-line integration path, which varies elliptically. Equation (21) is illustrated in Figure 9.11. As the aspect angle  $\alpha$  approaches normal incidence, the peak value of  $U(z)$  increases without bound, and the width of the ellipse approaches zero. In this limit  $U(z)$  reduces to a  $\delta$ -function, as in Eq. 9.7).

### 3.4.2 Cone

For generality, allow the cone to be truncated and denote the radii at the two ends by  $a_1$  and  $a_2$ . If the tip of the corresponding nontruncated cone is assumed to be at the origin, then the cone is represented by the height function  $h(r) = r \cot \alpha_c$  for  $a_1 < r < a_2$ . With these definitions, Eq. (18) for the range-resolved laser radar cross section becomes

$$U(z) = 8\pi \sin \alpha_c |z| \int_{\phi_1}^{\phi_2} \left( \frac{\tan \alpha_c + \tan \alpha \cos \phi}{1 - \tan \alpha_c \tan \alpha \cos \phi} \right)^2 f(\theta) d\phi \quad (22)$$

and the local angle of incidence in Eq. (20) reduces to

$$\cos \theta = \cos \alpha_c \sin \alpha \cos \phi + \sin \alpha_c \cos \alpha \quad (23)$$

Although Eq. (22) can be integrated analytically for certain choices of  $f(\theta)$ , it is left in its integral form because it is compact, well suited to numerical integration, and valid for arbitrary choices of  $f(\theta)$ .

Before Eq. (22) can be applied, the limits of integration must be determined. This determination is often the most difficult part of the calculation of a range-resolved laser radar cross section because these limits generally vary with both the aspect angle  $\alpha$  and the range value  $z$ . But once these limits are determined, they can be applied to arbitrary choices of  $f(\theta)$ . As illustrated in Figure 9.12, two boundary types are associated with the azimuthal limits of integration for a cone. They are *shadow boundaries* and *truncation boundaries*. Shadow boundaries cause the region of integration  $A_h$  in Eq. (14) to be pie-shaped, as illustrated in Figure 12(b). The half-angle of the illuminated segment of the pie is denoted by  $\phi_s$ . Truncation boundaries occur when the range plane cuts through the circle of radius  $a_1$ , which is associated with the truncation plane, or through the circle of radius  $a_2$ , which defines the cone base. The corresponding azimuthal limits of integration are denoted as  $\phi_{b_1}$  and  $\phi_{b_2}$ , respectively. Note that  $\phi_s$  is independent of range but that  $\phi_{b_1}$  and  $\phi_{b_2}$  depend on range.

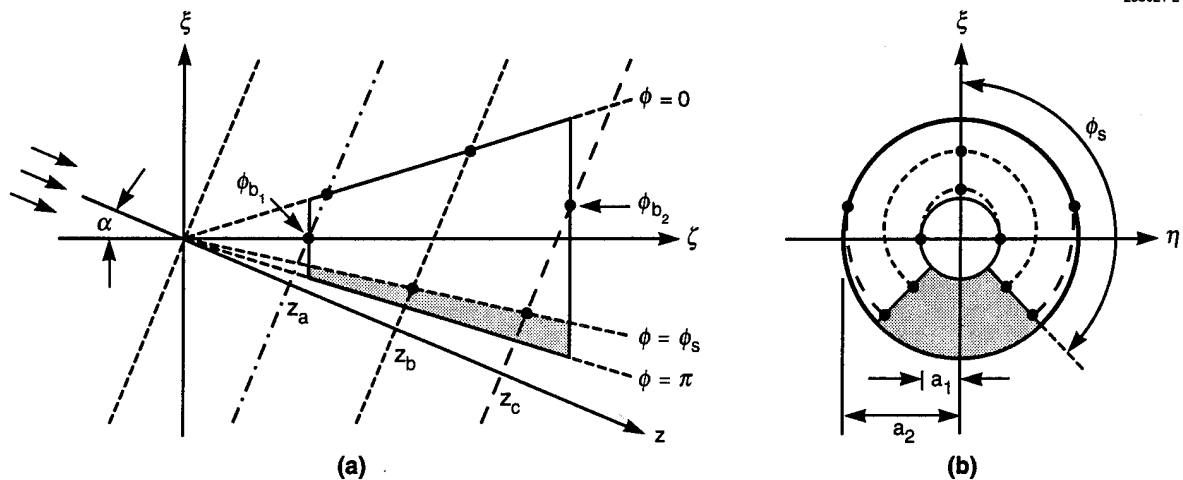


Figure 12. Limits of integration for calculating the range-resolved laser radar cross section for off-axis illumination of a truncated cone: (a) shadow boundaries and truncation boundaries for three separate range planes cutting through the cone; (b) the corresponding integration paths in  $\xi$ - $\eta$  space.

Before evaluating the shadow and truncation boundaries, an important feature of Eq. (22) should be observed: the explicit dependence on  $z$  occurs only in the linear factor in front of the integral. Therefore, as long as the limits of integration do not depend on  $z$ , the  $U(z)$  curve will increase linearly with range, just as it does for the on-axis cone described by Eq. (10). As already noted, the limits of integration can exhibit range dependence only for those values of range and for those aspect angles where the range plane intersects one of the truncation planes. For every truncated cone there is a range of aspect angles, beginning with  $\alpha = 0$ , such that there are no truncation boundaries. Thus, every truncated cone exhibits a linear dependence on  $z$  over some region of  $\alpha$ - $z$  space, and the longer the cone, the larger the angular region where this dependence occurs. This linear dependence on  $z$  produces a distinctive signature that can be used for identifying and characterizing conical objects.

Now we describe how the two types of boundaries are determined. Shadow boundaries can be obtained by setting  $\cos\theta$  equal to zero in Eq. (23) and solving for  $\phi$ :

$$\phi_s = \text{Re} \left[ \cos^{-1}(-\tan \alpha_c \cot \alpha) \right] \quad (24)$$

The reason for taking the real part is that the inverse cosine becomes complex when  $\alpha < \alpha_c$  and when  $\alpha > \pi \equiv \alpha_c$ . In the first case, the entire cone is illuminated so that no shadowing occurs, and Eq. (24) reduces to  $\phi_s = \pi$ . In the second case, the cone is completely unilluminated (only the inside of the cone is visible to the laser), so that complete shadowing occurs and Eq. (24) reduces to  $\phi_s = 0$ .

Truncation boundaries are determined by setting  $r_i$  equal to  $a_1$  or  $a_2$  in Eq. (19) and solving for  $\phi$ .

This yields

$$\phi_{b_n} = \text{Re} \left[ \cos^{-1} \left( \cot \alpha_c \cot \alpha - \frac{z}{a_n \sin \alpha} \right) \right], \quad (25)$$

where  $n$  assumes the value 1 or 2. Taking the real part in Eq. (25) allows us to define  $\phi_{b_n}$  for cases in which no intersection occurs between the range plane and the truncation boundary of the cone. The value assigned is the last value, 0 or  $\pi$ , that  $\phi_{b_n}$  had as the range plane moved away from the object.

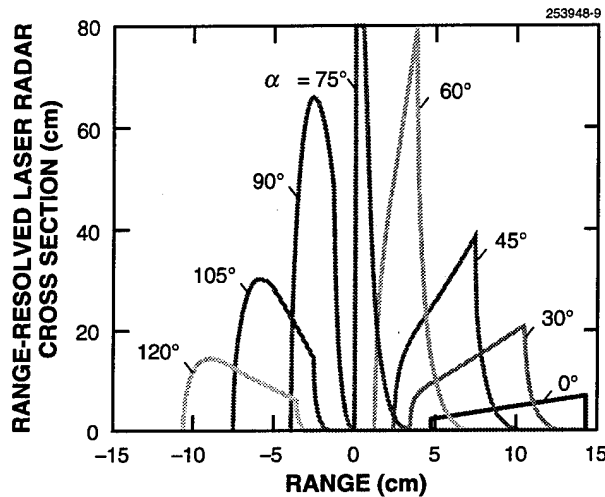


Figure 13. Range-resolved laser radar cross section for a truncated Lambertian cone viewed at various aspect angles. The cone half-angle is  $15^\circ$  and the distance between the truncation planes is 10 cm. The range-reference point is located at the apex of the corresponding untruncated cone, which is located 5 cm to the left of the first truncation plane. There are no contributions from the disk-shaped regions formed by the intersection of the truncation planes with the cone.

Now that the different boundary types have been analyzed, the next step is to choose the limits of integration that are appropriate for the given situation. By referring to Figure 12, one can show that the algorithm defined by

$$\phi_1 = \min(\phi_s, \phi_{b_1}, \phi_{b_2}) \quad (26)$$

and

$$\phi_2 = \min[\phi_s, \max(\phi_{b_1}, \phi_{b_2})] \quad (27)$$

correctly handles all possible situations. Figure 13 contains plots of Eq. (22) for the range-resolved laser radar cross section of a truncated Lambertian cone illuminated at various angles. The cone has the same shape as the one in Figure 12. The cone half-angle is  $15^\circ$ , the distance between truncation planes is 10 cm, and the distance from the first truncation plane to the apex of the corresponding untruncated cone is 5 cm. Note that as pointed out above, the  $U(z)$  curves have a large linear region if the aspect angle is small, but this linear region eventually disappears as the aspect angle increases.

### 3.4.3 Cylinder

The cylinder does not lend itself to direct analysis by Eq. (18) because  $h(r)$  is ill defined in the associated coordinate system. Equation (22) for a cone, however, can be applied to a cylinder by taking the limit as  $\alpha_c$  approaches zero. A slight complication occurs when doing so. Because the origin of the coordinate system is at the apex of the cone, the range values of interest shift to infinity. To adjust for this shift, the equation is transformed to a coordinate system having its origin at the truncation point where  $r = a_1$ . When the aspect angle  $\alpha = 0$ , the range offset between the origins of the two coordinate systems is simply the axial distance from the apex of the cone to the truncation plane  $\zeta_0 = a_1 \cot \alpha_c$ . But as  $\alpha$  increases, this offset is reduced by a factor of  $\cos \alpha$ . Thus, the coordinates in Eq. (22) are transformed by replacing  $z$  with  $z + a_1 \cot \alpha_c \cos \alpha$ . For a cylinder of length  $L$  and radius  $a$ , Eq. (22) reduces to

$$U(z) = 8\pi a \frac{\sin^2 \alpha}{|\cos \alpha|} \int_{\phi_1}^{\phi_2} \cos^2 \phi f[\cos^{-1}(\sin \alpha \cos \phi)] d\phi \quad , \quad (28)$$

where

$$\phi_{b_1} = \text{Re} \left[ \cos^{-1} \left( \frac{-z}{a \sin \alpha} \right) \right] \quad (29)$$

and

$$\phi_{b_2} = \text{Re} \left[ \cos^{-1} \left( \frac{L \cos \alpha - z}{a \sin \alpha} \right) \right] \quad . \quad (30)$$

The limits of integration are obtained by using Eqs. (26) and (27) with  $\phi_s = \pi/2$ . Note that  $U(z)$  for a cylinder is independent of range, regardless of the functional form of  $f(\theta)$ , as long as the range plane does not cross a truncation boundary. Thus, all cylinders have a region in  $z$ - $\alpha$  space where  $U(z)$  is independent of range; this region provides a distinctive range-resolved laser radar cross-section signature for cylindrical objects. Equation (28) is illustrated in Figure 14 for a 10-cm-long, 4-cm-diameter Lambertian cylinder illuminated at various angles  $\alpha$ . To separate the curves for the different values of  $\alpha$  from one another in range,  $U(z - \zeta_0 \cos \alpha)$  has actually been plotted, where  $\zeta_0 = 5$  cm. The range offset in the argument corresponds to measuring the range with respect to a point on the cylinder axis that is 5 cm outside of the cylinder.

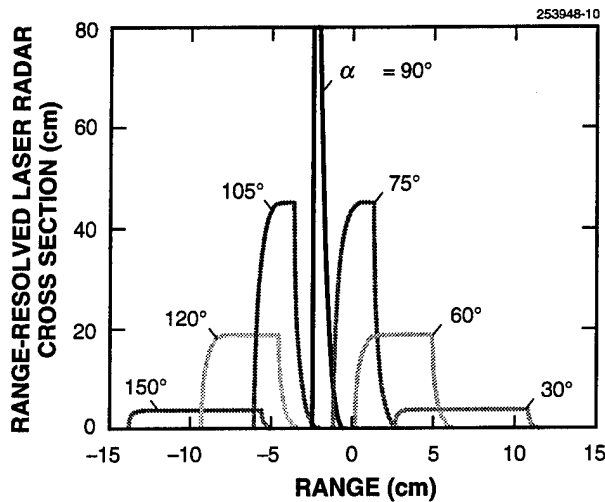


Figure 14. Range-resolved laser radar cross section for a Lambertian cylinder viewed at various aspect angles. The length of the cylinder is 10 cm and its diameter is 4 cm. The range-reference point is located 5 cm outside of the cylinder to separate the various plots in range. There are no contributions from the disk-shaped endcaps.

### 3.4.4 Truncated Sphere

Equation (11) gives the general solution of the range-resolved laser radar cross section for a complete sphere. Although this solution does not depend on aspect angle, the solution for a truncated sphere does. Because the truncated sphere is an important component for building up composite target models, its angle-dependent range-resolved laser radar cross section is also described. If the center of the sphere is located at the origin and that the truncation plane is at a height  $h$ , then the value of  $h$  ranges between  $-a$  and  $a$ , with  $-a$ ,  $0$ , and  $a$  corresponding respectively to a single point at the pole, a hemisphere, and a complete sphere. For some values of  $z$ , the truncation boundary limits the range of the azimuthal integration so that it no longer covers a complete circle. Equation (11) is modified to account for the truncation boundary by replacing  $\pi$  with the actual angular half-range of integration, which varies between  $0$  and  $\pi$ . The new form is

$$U(z) = \frac{8\pi}{a} f[\cos^{-1}(-z/a)] \operatorname{Re} \left[ \cos^{-1} \left( \frac{z \cos \alpha - h}{\sqrt{a^2 - z^2} \sin \alpha} \right) \right] z^2 \quad \text{for } -a \leq z \leq 0 \quad (31)$$

Spherical objects also have a distinctive signature. For any values of the truncation height  $h$ , there is an angular region, beginning with  $\alpha = 0$ , such that  $U(z)$  is independent of viewing angle over certain values of  $z$ . Equation (31) is illustrated in Figure 15.

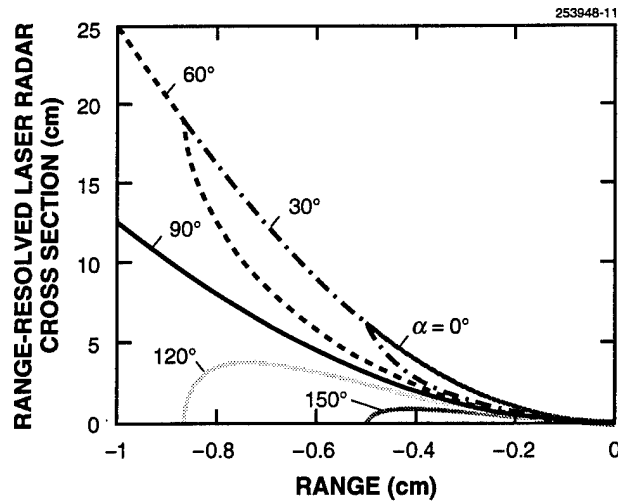


Figure 15. Range-resolved laser radar cross section for a 1-cm-radius Lambertian hemisphere viewed at various aspect angles.

### 3.4.5 Composite Objects

The preceding results are combined to obtain the aspect-angle-dependent range-resolved laser radar cross section for a Lambertian cylinder-disk combination and for a Lambertian sphere-cone-disk combination. The spherical and conical segments of the sphere-cone-disk are joined together such that the slope of the surface is continuous. Figure 16 shows 3D plots of the logarithm of the range-resolved laser radar cross section as a function of range and aspect angle for these two objects. The separate signatures for the disk, the cone, the cylinder, and the sphere are evident in these plots.

It has already been pointed out that it is easier to obtain the autocorrelation of  $U(z)$  than  $U(z)$  itself by the wavelength-decorrelation method. Figure 16 also shows the autocorrelation functions of  $U(z)$  for comparison. One can clearly distinguish between the two shapes, given the aspect-angle dependence of the autocorrelation function.

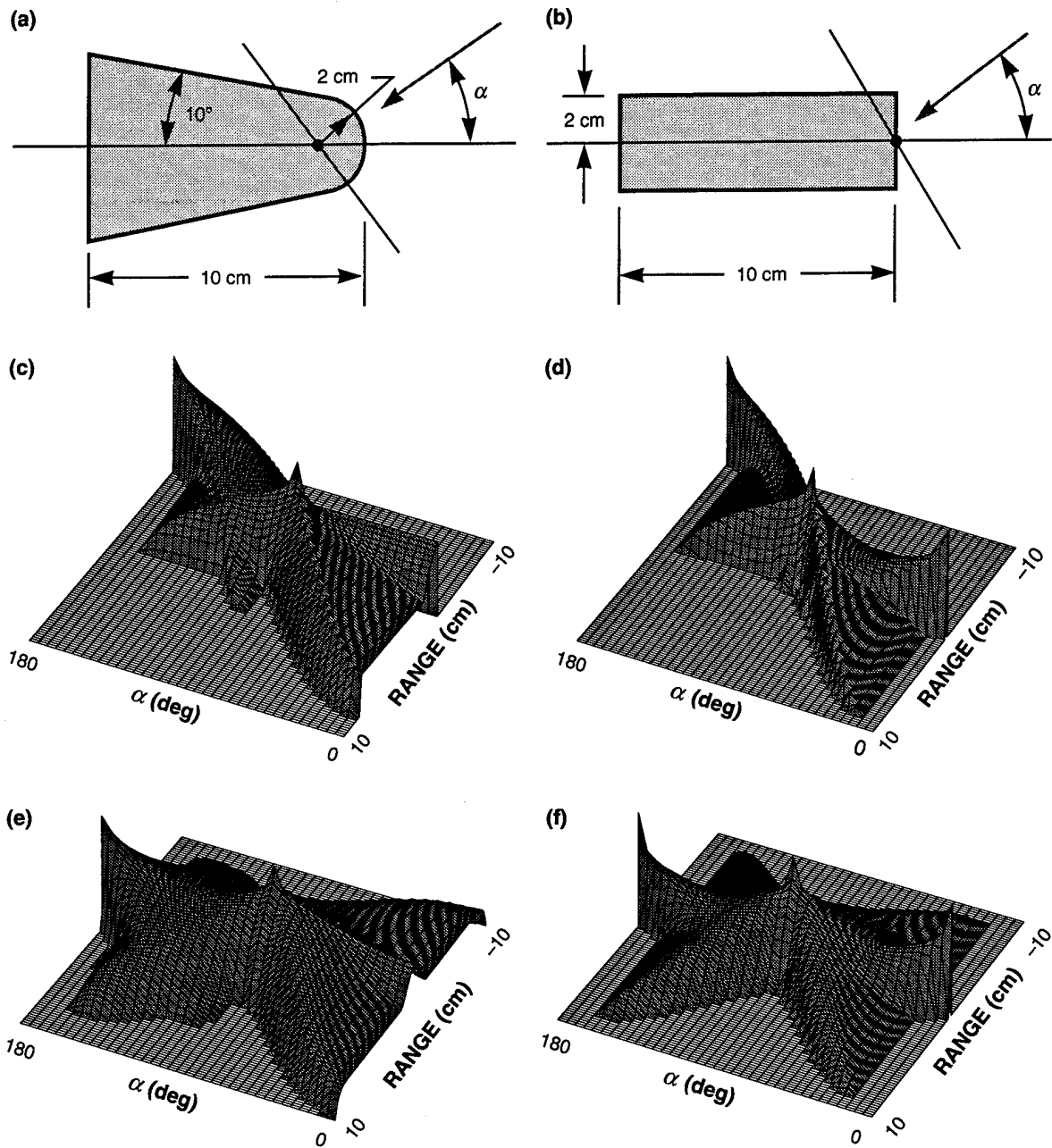


Figure 16. Wavelength-decorrelation signatures for composite objects: (a) Lambertian sphere-cone-disk combination; (b) Lambertian cylinder with disk endcaps; (c) and (d) aspect-angle dependence of the range-resolved laser radar cross section for parts a and b, respectively; (e) and (f) autocorrelation functions of the range-resolved laser radar cross section for parts a and b, respectively. The magnitude of these signatures is plotted on a logarithmic scale covering four decades for parts c and d and two decades for parts e and f.

## 4. THEORY FOR WAVELENGTH DECORRELATION

It has been shown how the range-resolved laser radar cross section  $U(z)$  relates to an object's shape and angular surface-scattering properties. The next step is to show theoretically how  $U(z)$  is related to the fluctuating speckle intensity caused by scanning the laser frequency. This section begins by explaining why speckle intensity fluctuates as laser frequency varies; it then develops the theoretical foundation for extracting information about the scattering object.

### 4.1 WAVELENGTH DEPENDENCE OF SPECKLE

If the objects shown in Figure 2 are illuminated with a tunable laser, the corresponding speckle patterns appear to boil, or decorrelate, from the original pattern as the laser frequency varies. The frequency shift, or decorrelation frequency  $\Delta\nu_D$ , required to decorrelate the speckle pattern depends on the size, shape, and orientation of the object. For example, the speckle pattern corresponding to the ring decorrelates very slowly compared to the other two patterns. This large decorrelation frequency is due to the fact that the ring has a very small range extent, being illuminated at normal incidence. In general, the decorrelation frequency  $\Delta\nu_D$  is inversely proportional to the range extent  $L$  of the illuminated portion of the object.

Refer to Figure 17 for a basic understanding of the wavelength dependence of speckle. In Figure 17(a) a seven-level step target is being flood-illuminated along the  $z$ -axis with a tunable laser. Our objective is to determine the frequency dependence of the speckle intensity at a distant point  $P$  lying on the negative  $z$ -axis. A scalar treatment of the optical field is sufficient for this purpose and for the analysis that follows. We also assume that the illuminating laser beam is monochromatic and suppress a harmonic time dependence. The complex amplitude of the optical field at the point  $P$  is the sum of the contributions from each of the seven levels. These contributions are represented by the phasors (solid lines) located below each level. The magnitude of these phasors represents the strength of the return, and the orientation represents the relative phase of each contribution. The relative phase is a combination of the phase due to wave propagation between scattering planes and a random component that accounts for the surface roughness. Figure 17(b) shows the resultant phasor obtained by placing the components end to end in the complex plane (solid lines). The optical intensity, or irradiance, is proportional to the magnitude-squared of the resultant, shown by the diamond in Figure 17(c). The phase of the resultant is given by the diamond in Figure 17(d).

Now consider the effect that changing the laser frequency  $\nu$  has on the complex amplitude and the intensity at point  $P$ . Let  $\phi$  represent the component of the phase (for a given level) that arises from wave propagation. If  $\phi$  is measured with respect to the  $z = 0$  plane (defined by the first level), the phase delay for propagation from this plane to a plane with range  $z$  is  $\phi = 2\pi z/\lambda = 2\pi z\nu/c$ , where  $c$  is the speed of light. For a given range  $z$ , a change in frequency of  $\Delta\nu$  introduces a phase shift, or phasor rotation, of

$$\Delta\phi = 2\pi \frac{2z}{c} \Delta\nu \quad (32)$$

for round-trip propagation between the two planes. Equation (32) can now be used to determine how much a given frequency change  $\Delta\nu$  rotates each phasor in Figure 17(a). The dashed phasors in this figure

correspond to  $\Delta\nu = c/(8L)$ , which is the frequency shift required to rotate the phasor at the  $Z = L$  plane by  $90^\circ$ . Because of the linear relation between phase shift and distance, the phasor at the  $L/2$  plane is rotated by  $45^\circ$  and the phasor at the  $L = 0$  plane is stationary. The new resultant is shown by the square in Figure 17(b).

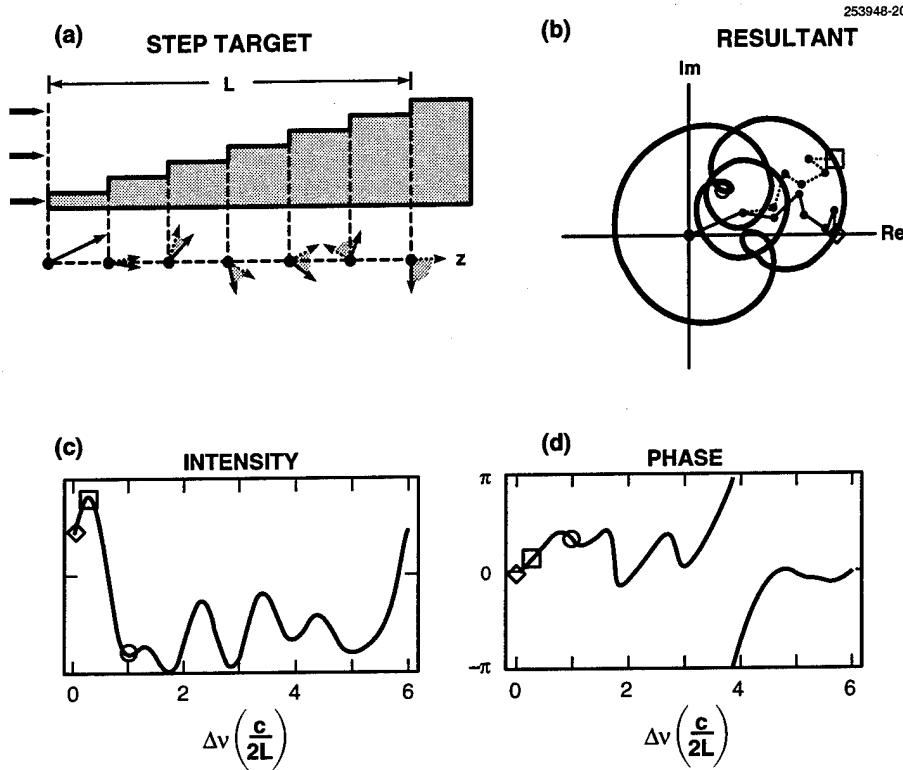


Figure 17. Frequency dependence of the on-axis speckle intensity from a step target: (a) step target with phasors indicating contributions from each step for two frequencies, (b) path of resultant complex amplitude in the complex plane, (c) frequency dependence of intensity, and (d) frequency dependence of phase.

Because the magnitude increases, so does the intensity in Figure 17(c). The phase in Figure 17(d) also increases because the resultant in Figure 17(c) rotates in the counterclockwise direction. Observe that a rotation of  $90^\circ$  at the  $z = L$  plane was insufficient to decorrelate the speckle intensity. The curved path in Figure 17(b) represents the trajectory that the resultant complex amplitude takes as the frequency varies. As illustrated by the circles in Figures 17(b)–17(d), a rotation of  $360^\circ$  is adequate for decorrelation. For this value, the phasor at  $z = L/2$  is  $180^\circ$  out of phase (even though the phasor at  $z = L$  is back in phase), producing a different resultant. If a  $360^\circ$  rotation is used as the basis for defining the decorrelation frequency, then  $\Delta\nu_D$  takes the value

$$\Delta\nu_D = \frac{c}{2L} \quad (33)$$

As an illustration of Eq. (33), the decorrelation frequency for an object with a range extent of 10 cm is 1.5 GHz. Note that  $\Delta\nu_D$  also corresponds to the longitudinal mode spacing of a laser cavity of length  $L$ . If the step target consisted of only two levels separated by the distance  $L$ , as in a laser cavity, the speckle intensity would go through one complete cycle, returning to the original value for each increment of  $\Delta\nu_D$ . The trajectory in Figure 17(b) closes on itself because there is a finite number of equally spaced levels. The number of oscillations in intensity that occur before the pattern repeats itself is the number of discrete steps, that is, six.

In the physical model that has been given for the frequency dependence of speckle, the resultant complex amplitude is the sum of the contributions from individual scattering planes. These contributions are represented by phasors that rotate as the frequency varies. The rotation rate of a given phasor is proportional to the distance  $z$  from the reference plane. Mathematically, this picture of the frequency dependence is equivalent to a Fourier transform of the distribution of the scattering strength along the  $z$ -axis. The kernel of the Fourier-transform integral is  $\exp(i\Delta\phi)$ , which varies according to range  $z$  by Eq. (32). The Fourier-transform relation will be discussed more thoroughly and the equations written explicitly in Section 4.3.

Another observation about the wavelength dependence of speckle is that the fluctuating speckle intensity produced by scanning the laser frequency is band-limited, or has a highest frequency of oscillation, so that the speckle intensity cannot change any faster than this highest-frequency component. Large oscillation frequencies correspond to large range offsets between scattering cells. Therefore, the cutoff frequency that bandlimits the speckle-intensity sequence is just the decorrelation frequency  $\Delta\nu_D$  that was derived for the total range extent  $L$  in Eq. (33). By the Nyquist sampling theorem, one must sample the speckle-intensity sequence at least twice during each of these highest-frequency oscillations. This leads to the conclusion that the laser-frequency step size between samples in the wavelength-decorrelation technique must obey the expression

$$\Delta\nu_{\text{step}} \leq \frac{c}{4L} \quad (34)$$

For example, an object with a range extent of 10 cm would require a laser-frequency step size of 750 MHz or less.

## 4.2 SPECTRAL DENSITY

The Introduction stated that there is a fundamental relation between the spectral density of the speckle signal and the autocorrelation function of the range-resolved laser radar cross section of the illuminated object. This relation will now be derived from basic principles. As in Section 3, the speckle intensity is quantified by using the irradiance  $E$ . The analysis is divided into two parts. First, a model is established for calculating the irradiance  $E(t)$  at the receiver in terms of the physical properties of the object; this model is then used to perform the statistical calculation of the spectral density.

The spectral density of  $E(t)$  is defined in terms of the Fourier transform of  $E(t)$ ,

$$\tilde{E}(f) = \int_{-\infty}^{\infty} E(t) \exp(-i2\pi ft) dt \quad , \quad (35)$$

by

$$G_E(f) = \frac{\langle |\tilde{E}(f)|^2 \rangle}{T} \quad , \quad (36)$$

where

$$T = \int_{-\infty}^{\infty} |w(t)|^2 dt \quad (37)$$

is the effective scan duration and  $w(t)$  is a dimensionless window function, ranging between zero and unity, that specifies the temporal shape and the duration of the transmitted signal irradiance. If  $w(t)$  turns on and off abruptly, then  $T$  is simply the scan duration in the usual sense. Typically,  $w(t)$  tapers to zero at the edges of the signal for the purpose of decreasing the side lobes. In this analysis, the scan duration is assumed to be long compared to the time it takes light to traverse the range extent of the object.

This model for the irradiance at the receiver differs from previous models for analyzing the wavelength dependence of speckle in that there is no prediction of angular-scattering effects from assumed surface statistics. Instead, these surface-correlation effects are taken into account directly through the functional dependence of  $f(\theta)$ , which can be readily measured in practice. This approach greatly simplifies the calculations. The resulting analysis, which is a hybrid between radiometry and physical optics, proceeds as follows.

First, the surface of the object is broken into  $N$  small uncorrelated area elements  $A_j$  and the principles of radiometry are used to calculate the contribution to the speckle-averaged irradiance at the receiver from each individual element. The magnitude of the complex amplitude at the receiver arising from an individual surface element on the object is obtained by taking the square root of the irradiance from that element. The phase is introduced by considering path lengths and assigning each scattering cell a random phase offset  $\phi_j$  that is uniformly distributed over  $2\pi$  radians. The  $N$  contributions  $V_j(t)$  to the total complex amplitude  $V(t)$  at the receiver are then added coherently, as in physical optics. Finally, the irradiance  $E(t)$  is obtained by squaring the magnitude of the complex amplitude.

This model for  $E(t)$  is based on the following reasoning. The area  $A_j$  of each surface element is large enough to determine the angular scattering (that is, large compared to the wavelength and the surface correlation length) but small enough so that the resultant complex amplitude  $V(t)$  at the receiver would not change significantly if the elements were further subdivided. For example, the range extent  $L_j$  of the individual surface elements must be small enough so that the corresponding decorrelation frequency  $\Delta\nu_D = c/(2L_j)$  from Eq. (33) is large compared with the total frequency scan of the laser. Because

objects of interest are large on a wavelength scale, the surface area can be divided into many individual cells that each satisfy these requirements.

The first step in calculating  $E(t)$  is to define the transmitted signal; its complex amplitude is expressed in the form

$$V_T(t) = \sqrt{E_0 w(t)} \exp[i\phi_T(t)] \quad . \quad (38)$$

In this equation  $E_0$  represents the final target irradiance after the transmitted beam has propagated over the distance  $R$ . As explained, variations in the transmitted irradiance with time are accounted for through the window function  $w(t)$ . The phase  $\phi_T(t)$  is obtained by assuming that the initial laser frequency is  $\nu_0$  and that  $\nu$  increases linearly in time at the rate  $\gamma$ , such that  $\nu = \nu_0 + \gamma t$ . Through application of the relation  $d\phi/dt = 2\pi\nu$ ,

$$\phi_T(t) = 2\pi \left( \nu_0 + \frac{\gamma t}{2} \right) t \quad (39)$$

is obtained, which completes the description of the transmitted signal.

Having defined the transmitted signal, the irradiance at the receiver can now be found. Because a monostatic and far-field configuration is assumed, one need only consider rays that propagate parallel to the  $z$ -axis. For the  $j$ th scattering cell, the round-trip propagation time from the transmitter back to the receiver is  $t_0 + t_j$ , where  $t_0 = 2R/c$  is the round-trip propagation time to the  $z = 0$  plane (from which the object height function is defined) and  $t_j = 2h_j/c$  is the round-trip propagation time between the  $z = 0$  plane and the  $j$ th scattering cell. The time dependence associated with the contribution  $V_j(t)$  is the same as the time dependence of the transmitted signal  $V_T(t)$  but at the earlier time  $t - t_0 - t_j$ . By the procedure outlined above, the total complex amplitude at the receiver is

$$V(t) = \sqrt{w(t-t_0)} \sum_{j=1}^N \sqrt{\langle E_j \rangle} \exp\{i[\phi_T(t-t_0-t_j) + \phi_j]\} \quad . \quad (40)$$

Equation (40) assumes that the pulse duration  $T$  is long compared to the largest value of  $t_j$  and that  $w(t)$  is slowly varying, except possibly at the edges, to replace  $w(t-t_0-t_j)$  by  $w(t-t_0)$  and move it outside of the summation. The expected irradiance  $\langle E_j \rangle$  from the  $j$ th scattering cell is found by substituting its cross section, obtained from Eq. (4), into Eq. (1) and rearranging terms to yield

$$\langle E_j \rangle = \frac{E_0}{R^2} f(\theta_j) \cos^2 \theta_j A_j \quad . \quad (41)$$

The irradiance  $E(t)$  at the receiver is the magnitude-squared of  $V(t)$  in Eq. (40).

To perform the statistical analysis, the magnitude-squared in the computation of  $E(t)$  must be expanded into a double summation. This is done by using two different summation indices [ $j$  for writing  $V(t)$  and  $k$  for writing its complex conjugate] and multiplying to yield

$$E(t) = w(t-t_0) \sum_{j=1}^N \sum_{k=1}^N \sqrt{\langle E_j \rangle \langle E_k \rangle} \exp\left\{i\left[\phi_T(t-t_0-t_j) - \phi_T(t-t_0-t_k) + \phi_j - \phi_k\right]\right\} \quad (42)$$

The significance of a linear scan becomes apparent when Eq. (39) for  $\phi_j(t)$  is substituted into Eq. (42); the quadratic terms cancel, which leaves a linear dependence of phase on time  $t$ :

$$\phi_T(t-t_0-t_j) - \phi_T(t-t_0-t_k) = 2\pi(t_k-t_j)\left[v_0 + \gamma(t-t_0)\right] + \pi\gamma(t_j^2 - t_k^2). \quad (43)$$

These linear phase factors correspond to frequency offsets in the Fourier-transform domain. The size of these offsets is proportional to the axial propagation time  $t_k - t_j$  and, hence, proportional to the range offset  $h_k - h_j$  between scattering cells. Thus, the intensity signal carries information about range. The other phase terms in Eq. (43), which do not depend on time, are unimportant and cancel out later in the analysis.

To proceed with the evaluation of the spectral density defined in Eq. (36), take the Fourier transform of Eq. (42), square its magnitude, apply the expected-value operator, and divide by the effective scan duration. This yields

$$\begin{aligned} G_E(f) &= \frac{1}{T} \sum_{j=1}^N \sum_{k=1}^N \sum_{l=1}^N \sum_{m=1}^N \sqrt{\langle E_j \rangle \langle E_k \rangle \langle E_l \rangle \langle E_m \rangle} \left\langle \exp\left[i(\phi_j - \phi_k - \phi_l + \phi_m)\right] \right\rangle \\ &\quad \times \exp\left[-i2\pi v_0(t_j - t_k - t_l + t_m)\right] \exp\left[-i\pi\gamma(t_j^2 - t_k^2 - t_l^2 + t_m^2)\right] \\ &\quad \times \tilde{w}(f + f_j - f_k) \tilde{w}^*(f + f_l - f_m) \quad , \end{aligned} \quad (44)$$

where the notation  $f_j = \gamma t_j$  has been used for compactness. Note that frequency offsets are related to range offsets through  $f_j = 2\gamma h_j/c$ . Again, the magnitude-squared has been expanded in Eq. (44) by doubling the number of summations, this time to four. The summation is expanded to write the spectral density as a linear combination of the function  $\exp[i(\phi_j - \phi_k - \phi_l + \phi_m)]$  so that the expected-value brackets can be moved inside the summation to act on this function alone.

The next step is to apply known statistical properties of the random process  $\phi_j$  to evaluate the new expected value and to simplify Eq. (44). Two assumptions about  $\phi_j$  specify its statistical properties: (1) It is uncorrelated from cell to cell and (2) it is uniformly distributed over  $2\pi$  radians. These assumptions completely specify  $\phi_j$  and make it possible to write the expected value in terms of Kronecker  $\delta$ -functions as

$$\left\langle \exp\left[i(\phi_j - \phi_k - \phi_l + \phi_m)\right] \right\rangle = \delta_{jk} \delta_{lm} + \delta_{jl} \delta_{km} - \delta_{jklm} \quad (45)$$

By definition, a Kronecker  $\delta$ -function is unity when its subscripts are equal, and zero otherwise. Equation (45) can be derived by applying the two assumptions listed above. By the first assumption, the expected value in Eq. (45) can be expressed as the product of the expected values of the individual factors, as long as the indices are all unequal. But, by the second assumption,

$$\left\langle \exp(i\phi_j) \right\rangle = 0 \quad , \quad (46)$$

and the product of the expected values is zero. The only way for the expected value in Eq. (45) to be nonzero is if the phases add to zero, in which case the expected value is unity. For the phases to add to zero for every realization of the random process, the indices for positive and negative phases must be equal in pairs. Equation (45) covers all the possibilities.

By applying Eq. (45) to Eq. (44), the quadruple summation can be reduced to

$$G_E(f) = \frac{|\tilde{w}(f)|^2}{T} \left[ \left( \sum_{j=1}^N \langle E_j \rangle \right)^2 - \sum_{j=1}^N \langle E_j \rangle^2 \right] + \sum_{j=1}^N \sum_{k=1}^N \langle E_j \rangle \langle E_k \rangle \frac{|\tilde{w}(f + f_j - f_k)|^2}{T} \quad (47)$$

The double summation can be further reduced by observing that

$$|\tilde{w}(f + f_j - f_k)|^2 = |\tilde{w}(f)|^2 * \delta(f + f_j - f_k) = |\tilde{w}(f)|^2 * [\delta(f - f_j) \star \delta(f - f_k)] \quad (48)$$

where the asterisk denotes convolution and the five-pointed star denotes cross-correlation. Equation (48) allows the double summation to be written as an autocorrelation of two single summations, convolved with the Fourier-transform magnitude-squared of the window function.

The next step is to interpret the meaning of the resulting three types of single summations. The first summation in Eq. (47) is the easiest to interpret. The sum of the ensemble-averaged contributions to the irradiance is simply the total irradiance, which can be expressed in terms of the object's cross section  $\sigma$  through Eq. (1), yielding

$$\sum_{j=1}^N \langle E_j \rangle = \frac{E_0}{4\pi R^2} \sigma \quad (49)$$

The magnitude of the second summation depends on the number of surface cells  $N$  used in modeling the object. Note that because the strength of the individual components  $\langle E_j \rangle$  falls off as  $1/N$  as the object is divided into smaller surface patches, the magnitude of the individual terms in the series goes as  $1/N^2$ . Because the series contains  $N$  terms, the magnitude of the summation is inversely proportional to  $N$ . Thus,

$$\lim_{N \rightarrow \infty} \sum_{j=1}^N \langle E_j \rangle^2 = 0 \quad (50)$$

and this term can be dropped because only objects that have many uncorrelated scattering cells are being considered. The third summation can be made to resemble Eq. (6) for the range-resolved laser radar cross section if it is converted to an integral by taking the limit of large  $N$ . The result is

$$\lim_{N \rightarrow \infty} \sum_{j=1}^N \langle E_j \rangle \delta(f - f_j) = \frac{E_0}{4\pi R^2} \frac{c}{2\gamma} U(z) \Big|_{z=\frac{c}{2\gamma}f} \quad (51)$$

The factor involving the speed of light  $c$  and the scan rate  $\gamma$  arises from converting the  $\delta$ -function from a function of frequency  $f$  to a function of range  $z$ .

The remaining quantity to be interpreted in Eq. (47) is the Fourier-transform magnitude-squared of the window function, divided by the effective scan duration  $T$ . In the limit of large  $T$ , this function becomes a  $\delta$ -function of frequency and the convolution does not blur the signature. It is convenient to define a related quantity that is a function of range  $z$ ; namely,

$$W_z(z) = \frac{2\gamma}{c} \frac{|\tilde{w}(f)|^2}{T} \Big|_{f=\frac{2\gamma}{c}z} \quad (52)$$

This quantity can be interpreted as the range-resolution impulse response of the system. In the limit as the scan bandwidth  $B = \gamma T$  approaches infinity, this impulse response also reduces to a  $\delta$ -function; that is,  $W_z(z) = \delta(z)$ . Again, the factor of  $2\gamma/c$  in Eq. (52) accounts for converting the  $\delta$ -function from a function of frequency to a function of range.

With these observations, Eq. (47) can be rewritten in the form

$$G_E(f) \Big|_{f=\frac{2\gamma}{c}z} = \left( \frac{E_0}{4\pi R^2} \right)^2 \frac{c}{2\gamma} \left[ W_z(z)\sigma^2 + W_z(z) * R_U(z) \right] \quad (53)$$

where the autocorrelation function is given by

$$R_U(z) = \int_{-\infty}^{\infty} U(z')U(z+z')dz' \quad (54)$$

It is not necessary to take the complex conjugate of the first  $U(z)$  in the definition of  $R_U(z)$ , as in the general definition of an autocorrelation function, because  $U(z)$  is always real. In Eq. (53), the spectral density of the fluctuating speckle irradiance consists of two terms: (1) a dc-like component that is proportional to the square of the object's total cross section  $\sigma$  and (2) a term that is proportional to the convolution of the system impulse function  $W_z(z)$  with the autocorrelation function  $R_U(z)$  of the object's range-resolved laser radar cross section  $U(z)$ . Both components are multiplied by a factor that accounts for the received signal strength.

As the length of the scan increases, the system impulse function becomes more localized. This localization causes the dc component in Eq. (53) to be more localized and also improves the resolution to which the autocorrelation function  $R_U(z)$  can be determined. Because the system impulse response reduces to a  $\delta$ -function in the large-bandwidth limit, the convolution can be dropped in this limit. In general, however, the width of the impulse response determines the range resolution. As an illustration of Eq. (52), let us assume that the window function turns on and off abruptly. Then  $T$  is simply the time it takes to complete the scan, and  $B$  is simply the total frequency scanned by the laser. The range-resolution impulse response evaluates to

$$W_z(z) = \frac{2B}{c} \text{sinc}^2\left(\frac{2B}{c}z\right) \quad (55)$$

where  $\text{sinc}(x) = \sin(\pi x)/(\pi x)$ . If the resolution  $\Delta z$  is defined to be the value of  $z$  where the sinc function has its first null, that is,  $x = 1$ , then

$$\Delta z = \frac{c}{2B} \quad (56)$$

As expected, the range resolution improves as the scan bandwidth increases. Equation (56) is used to define range resolution for arbitrary window shapes, where the effective bandwidth  $B$  corresponds to the effective scan duration  $T$  defined in Eq. (37).

The main advantage of the wavelength-decorrelation technique is that the high effective bandwidth of a tunable laser can be used to obtain range resolutions that far surpass conventional methods. For example, a range resolution of 1 mm can be achieved by scanning the laser over a bandwidth of 150 GHz. This bandwidth is a small frequency excursion for a tunable laser, and submillimeter range resolutions can readily be achieved.

A simple rule for relating the number of speckle oscillations that occur during a scan to the range resolution can now be obtained. Recall that a change in frequency of  $\Delta \nu_D$  corresponds to one oscillation of the speckle intensity. Consequently, a total of  $N_s = B/\Delta \nu_D$  oscillations of the speckle intensity occur for a frequency scan of length  $B$ . Likewise, for a range resolution of  $\Delta z$ , an object of range extent  $L$  can be divided into  $N_z = L/\Delta z$  range-resolution cells. The expression

$$N_s = \frac{B}{\Delta \nu_D} = N_z = \frac{L}{\Delta z} \quad (57)$$

is arrived at by combining Eq. (33) for the decorrelation frequency  $\Delta \nu_D$  that corresponds to a given range extent  $L$  with Eq. (56) for the range resolution  $\Delta z$  that corresponds to a given bandwidth  $B$ . Thus, the number of range-resolution cells  $N_z$  is equal to the number of speckle-intensity oscillations  $N_s$ . Equation (57) gives an intuitive way of determining how well an object is resolved in range.

Now return to Eq. (53). The dc component in this equation represents the fact that an intensity is nonnegative. If the signal were ac coupled or if the data were preprocessed by subtracting the mean, this component would be eliminated. Let us denote the zero-mean signal by a prime; that is,

$$E'(t) = E(t) - \langle E(t) \rangle \quad (58)$$

The Fourier transform of this signal also has zero mean and can be written in an analogous manner as

$$\tilde{E}'(f) = \tilde{E}(f) - \langle \tilde{E}(f) \rangle \quad (59)$$

It can be shown that the spectral density of the zero-mean signal takes the form

$$G_{E'}(f) \Big|_{f=\frac{2\gamma}{c}z} = \left( \frac{E_0}{4\pi R^2} \right)^2 \frac{c}{2\gamma} W_z(z) * R_U(z) \quad (60)$$

From either Eq. (53) or Eq. (60), the spectral density of the speckle irradiance provides a way to measure the autocorrelation function  $R_V(z)$  of an object's range-resolved laser radar cross section to a resolution determined by the scan bandwidth.

### 4.3 RANDOM-PROCESS REPRESENTATION

In the preceding calculation of the spectral density of the fluctuating speckle intensity, the complex amplitude  $V(t)$  is represented by Eq. (40), which is derived using a discrete scattering-cell model. We converted from summations to integrals allowing the number of cells  $N$  to approach infinity. An alternative approach introduced here streamlines further analysis of the statistical properties of the wavelength dependence of speckle. In this approach, a representation of the random process  $V(t)$  is constructed in which the limiting operation has already been performed. Thus, the new representation of  $V(t)$  is based on an underlying random process that is continuous, not discrete as is  $\phi_j$ .

The first step in constructing this new representation is to define an auxiliary complex amplitude  $V_s(t)$  that is similar to  $V(t)$  but stationary. Stationarity means that statistical moments, such as the average and the autocorrelation function, are independent of offsets in time. Because the nonstationarity in  $V(t)$  arises from the time dependence of the transmitted signal, it can be removed by dividing Eq. (40) by the time variation associated with  $V_T(t-t_0)$ . Thus,

$$V_s(t) = \lim_{N \rightarrow \infty} \sum_{j=1}^N \sqrt{\langle E_j \rangle} \exp\{i[\phi_T(t-t_0-t_j) - \phi_T(t-t_0) + \phi_j]\} \quad (61)$$

and

$$V(t) = \sqrt{w(t-t_0)} \exp\{i[\phi_T(t-t_0)]\} V_s(t) \quad (62)$$

To construct a representation for  $V_s(t)$  that does not require the limiting procedure, one must first know the statistical properties of  $V_s(t)$  that are to be duplicated. Because the complex amplitude is a superposition of many independent contributions and because none of these contributions dominates, the central limit theorem applies, and the real and imaginary parts of  $V_s(t)$  are normally distributed. A unique property of a normal, or Gaussian, random process is that it is completely determined by its first-order and second-order moments. The first-order moment is simply the mean, which by Eq. (46) is

$$\langle V_s(t) \rangle = 0 \quad (63)$$

Two types of second-order moments must be considered. One is the usual statistical autocorrelation function, defined as

$$R_{V_s}(t) = \langle V_s^*(t') V_s(t+t') \rangle \quad (64)$$

and the other does not include the complex conjugation. These two second-order moments behave quite differently. In particular, for  $V_s(t)$  the second type of moment vanishes, regardless of the arguments; that is,

$$\langle V_s(t')V_s(t+t') \rangle = 0 \quad . \quad (65)$$

Equation (65) indicates that  $V_s(t)$  is circular. Circularity means that the real and imaginary parts of the random process are uncorrelated and have equal variance [46–49]. Consequently, contours of constant probability are concentric circles centered on the origin of the complex plane. (A nonzero-mean random process can also be circular, but the contours of equal probability are centered around its mean.) In the theory of speckle, our assumptions about  $\phi_j$  lead to what is known as *Gaussian speckle* [46,47] or, more precisely, to a complex amplitude of the optical field that is represented by a zero-mean complex circular Gaussian random process.

Equation (65) follows directly from a similar property for the random process  $\phi_j$ ; namely,

$$\langle \exp[i(\phi_j + \phi_k)] \rangle = 0 \quad . \quad (66)$$

As in Eq. (45), the expected value in Eq. (66) vanishes when the indices are unequal, but here it also vanishes when the indices are equal because the two phases are not subtracted and do not cancel. If the phases were subtracted, then the expected value would be unity when the indices were equal. Therefore, this expected value can be expressed as a Kronecker  $\delta$ -function; that is,

$$\langle \exp[i(\phi_j - \phi_k)] \rangle = \delta_{jk} \quad . \quad (67)$$

Equation (67) can be used to evaluate the autocorrelation function  $R_{V_s}(t)$ , yielding

$$R_{V_s}(t) = \lim_{N \rightarrow \infty} \sum_{j=1}^N \langle E_j \rangle \exp(-i2\pi f_j t) \quad . \quad (68)$$

The next step is to express Eq. (68) in terms of the range-resolved laser radar cross section  $U(z)$ . This can be accomplished by noticing that the left side of Eq. (51) is the Fourier transform of the right side of Eq. (68) to within a sign flip in the frequency argument. Thus, the autocorrelation function  $R_{V_s}(t)$  can be written as

$$R_{V_s}(t) = \frac{E_0}{4\pi R^2} \tilde{U}(f_z) \Big|_{f_z = \frac{2\gamma}{c}t} \quad , \quad (69)$$

where the Fourier transform

$$\tilde{U}(f_z) = \int_{-\infty}^{\infty} U(z) \exp(-i2\pi f_z z) dz \quad (70)$$

is a function of spatial frequency. Because time and spatial frequency are related by a proportionality constant through

$$f_z = \frac{2\gamma}{c}t \quad , \quad (71)$$

the fluctuating speckle intensity can be represented either as a function of spatial frequency or as a function of time.

The random process  $V_s(t)$  has now been completely characterized. In summary, it is a stationary complex Gaussian random process that is zero mean [Eq. (63)] and circular [Eq. (65)] and whose autocorrelation function is proportional to  $\tilde{U}(f_z)$  [Eq. (69)]. The new representation of  $V_s(t)$  is obtained by requiring that all these specifications hold. This representation is

$$V_s(t) = \sqrt{\frac{E_0}{4\pi R^2}} \int_{-\infty}^{\infty} \sqrt{U(z)} g(z) \exp(-i2\pi f_z z) dz \Big|_{f_z = \frac{2\gamma t}{c}} \quad (72)$$

where  $g(z)$  is a stationary complex Gaussian random process that is zero mean,

$$\langle g(z) \rangle = 0 \quad (73)$$

circular,

$$\langle g(z') g(z+z') \rangle = 0 \quad (74)$$

and  $\delta$ -correlated,

$$\langle g^*(z') g(z+z') \rangle = \delta(z) \quad (75)$$

By using Eqs. (73), (74), and (75), one can verify that Eq. (72) satisfies Eqs. (63), (65), and (69), respectively. The new representation is known to be Gaussian because a linear combination of Gaussian random processes remains Gaussian.

The various components in Eq. (72) will now be interpreted. The factor in front of the integral accounts for the dependence of the received signal strength on the target irradiance and the target range. The integration represents a summation over the contributions to  $V_s(t)$  from different range planes. As described in Section 4.1, one can think of the individual contributions as phasors and of the integral as the phasor sum. The magnitude of the phasor for a given range plane is proportional to the square root of the laser radar cross section for that plane—hence the square root of  $U(z)$  in Eq. (72). The Gaussian random process  $g(z)$  introduces a random phase angle and a random magnitude to the phasor to account for the fact that the speckle from the individual range planes is Gaussian. The complex exponential introduces rotations of the phasors, with the rotation rate being proportional to the distance from the  $z = 0$  plane and proportional to the frequency shift  $\Delta\nu = \gamma t$  as explained in Section 4.1. In effect, scanning the laser frequency linearly in time results in a Fourier transformation of the quantity  $\sqrt{U(z)}g(z)$ . Equation (72) shows the fundamental role that Fourier transforms play in the wavelength dependence of speckle.

The random-process representation given in Eq. (72) is convenient for statistical calculations. It can be manipulated, either analytically or by computer simulation, to study input-output relations associated with a given signal-processing algorithm or to study higher-order statistics such as the bispectrum without first going through the discrete scattering-cell argument. To carry out this analysis, one must know the corresponding moments of the random process  $g(z)$ . These moments can be evaluated by applying the complex Gaussian moment theorem [50] to a  $\delta$ -correlated zero-mean random process. All odd-order

moments of  $g(z)$  vanish, as do all even-order moments that do not have an equal number of conjugated and nonconjugated variables. The remaining moments obey the general rule

$$\begin{aligned} \langle g^*(z_1)g^*(z_2)\cdots g^*(z_M)g(z_{M+1})\cdots g(z_{2M}) \rangle = \\ \sum_{\pi} \delta(z_1 - z_{M+p})\delta(z_2 - z_{M+q})\cdots \delta(z_M - z_{M+r}) \quad , \end{aligned} \quad (76)$$

where  $\pi$  denotes a summation over the  $M!$  possible permutations  $(p, q, \dots, r)$  of  $(1, 2, \dots, M)$ . Equation (76) reduces to Eq. (75) for  $M = 1$  and to

$$\langle g^*(z_1)g^*(z_2)g(z_3)g(z_4) \rangle = \delta(z_1 - z_3)\delta(z_2 - z_4) + \delta(z_1 - z_4)\delta(z_2 - z_3) \quad (77)$$

for  $M = 2$ . Equation (77) is analogous to Eq. (45) and is used in deriving Eq. (53) when using the continuous random process  $g(z)$  instead of the discrete random process  $\phi_j$ .

#### 4.4 COHERENT DETECTION

By Eq. (53), spectral analysis of the fluctuating speckle irradiance  $E(t) = |V(t)|^2$  provides the autocorrelation function  $R_U(z)$  of the object's range-resolved laser radar cross section  $U(z)$ . But Eq. (72) for the random-process representation of  $V_s(t)$  is written in terms of  $U(z)$ . This leads to the hypothesis that  $U(z)$  is recoverable through appropriate analysis of the complex-valued return signal  $V(t)$ . Because optical frequencies are so high (300 THz for a wavelength of 1  $\mu\text{m}$ ), however, the rapid phase fluctuations resulting from the harmonic time dependence of  $V(t)$  cannot be measured directly. Optical detectors generally measure the magnitude-squared of  $V(t)$ ; obtaining the phase of  $V(t)$  requires coherent detection.

The first inclination might be to use heterodyne detection to eliminate the high-frequency phase fluctuations that occur at the carrier frequency. (Heterodyne detection is a form of coherent detection where the return signal is mixed with a monochromatic reference beam that is shifted in frequency.) Heterodyne detection by itself, however, is insufficient; because the carrier frequency is changing, the reference-beam frequency must also be changing. To entirely eliminate rapid phase variations, the return signal  $V(t)$  must be mixed with a reference beam that is a copy of the transmitted signal, delayed by the round-trip transit time  $t_0$ . In terms of Eq. (62), this procedure corresponds to multiplying the complex exponential in Eq. (62) by its complex conjugate  $\exp[-i\phi_T(t - t_0)]$ . [Set the window function  $w(t)$  for the reference signal to unity.] This coherent-detection approach corresponds to matched filtering or stretched processing [25].

The random-process representation for the coherently detected signal can now be written. Because complex amplitudes are being dealt with rather than intensities, the notation for the window function is changed to the quantity  $a(t) = \sqrt{w(t)}$ . Then the coherently detected signal becomes

$$\begin{aligned} V_c(t) &= V(t)\exp[i\phi_T(t - t_0)] \\ &= \sqrt{\frac{E_0}{4\pi R^2}} a(t - t_0) \int_{-\infty}^{\infty} \sqrt{U(z)} g(z) \exp(-i2\pi f_z z) dz \Big|_{f_z = \frac{2\gamma}{c}} \quad . \end{aligned} \quad (78)$$

The spectral density for the coherently detected signal is

$$G_{V_c}(f) = \frac{\langle |\tilde{V}_c(f)|^2 \rangle}{T_a} \quad , \quad (79)$$

where the effective scan duration is

$$T_a = \int_{-\infty}^{\infty} |a(t)|^2 dt \quad . \quad (80)$$

By using the random-process representation given in Eq. (78) and by applying the fact that the underlying random process  $g(z)$  is  $\delta$ -correlated [Eq. (75)], the spectral density can be written in the form

$$G_{V_c}(f) \Big|_{f=-\frac{2\gamma}{c}z} = \frac{E_0}{4\pi R^2} \frac{c}{2\gamma} A_z(z) * U(z) \quad , \quad (81)$$

where

$$A_z(z) = \frac{2\gamma}{c} \frac{|\tilde{a}(f)|^2}{T_a} \Big|_{f=-\frac{2\gamma}{c}z} \quad (82)$$

is the range-resolution impulse response of the system. As before, the impulse response reduces to a  $\delta$ -function in the large scan bandwidth limit, and the convolution with the impulse response can be dropped in Eq. (81) in this limit. Thus, the spectral density of the coherently detected signal provides a measurement of the object's range-resolved laser radar cross section  $U(z)$ , not just the autocorrelation function  $R_V(z)$ .

Note that Eq. (81) contains a sign flip between the frequency  $f$  and the range  $z$  for coherent detection, but there is no sign flip in Eq. (60) for direct detection. Actually, Eq. (60) could have been written with the sign flip because the spectral density is an even function for direct detection. Thus, the relation between frequency and range

$$f = -\frac{2\gamma}{c}z \quad (83)$$

actually covers both situations. The sign flip in Eq. (83) occurs because Eq. (72) has a negative sign in the complex exponential, but a positive sign is needed to make the integral look like an inverse Fourier transform of a function of frequency.

We consider three general approaches to creating the coherent-detection reference signal required for direct measurement of  $U(z)$ . The first approach, and the one used in the measurements in Section 5, is to place a diffuse range-reference plane in the vicinity of the object so that it is also illuminated by the laser beam (see Figure 18). The range-reference plane produces a delayed copy of the transmitted signal at the receiver that mixes coherently with the return signal from the object. By Eq. (81), the spectral

density of this coherently detected signal provides a direct measurement of  $U(z)$ . It is also useful to consider the function of the range-reference plane from the point of view of direct detection. Assume that a range-reference ring is located behind the object at position  $z_0$ , as shown at the top of Figure 18. This reference ring produces a sharp spike, or a  $\delta$ -function, in the  $U(z)$  curve shown in the center of Figure 18. As usual, the spectral density of the directly detected signal produces the autocorrelation function of  $U(z)$ , but  $U(z)$  now contains the additional  $\delta$ -function component. In calculating the autocorrelation function for this combination graphically, one would choose a particular range-offset value (for example,  $z_a$ ), replicate the original  $U(z)$  function with this range offset, multiply the original curve and the shifted curve point by point to obtain a product curve, and integrate to obtain the area under this product curve. The result for the offset value  $z_a$  is shown in the curve at the bottom of Figure 18. This procedure may be repeated for different values of range offset to fill out the autocorrelation-function curve.

Figure 18 shows that for range-offset values between  $z_a$  and  $z_0$ , the  $\delta$ -function traces through the  $U(z)$  curve for the triconic and replicates its functional form. Observe that the range-reference plane must be separated from the target by a distance greater than the target's range extent  $L$ ; otherwise, the desired  $U(z)$  curve will overlap with the central autocorrelation curve  $R_U(z)$ . Because autocorrelation functions of real quantities are even functions, the replicated  $U(z)$  curves on either side of the origin are mirror images of each other. If the reference plane is located behind the target, as depicted in Figure 18, then the  $U(z)$  curve on the left side has the correct orientation; if the reference plane is located in front of the target, the curve on the right side must be chosen.

The use of a range-reference plane is limited to situations where the object is readily accessible. For inaccessible objects at relatively short ranges, it may be feasible to implement coherent detection by using the second approach. The reference beam is produced in this approach by splitting the laser beam before it is expanded and running the unexpanded beam through a delay line of appropriate length. Near the detector array the reference beam is expanded and collimated for uniform illumination of the array. Because the reference beam is self-contained, this method could be used in a remote-sensing application, where there is no physical access to the target. Because of the requirement for a delay path, this approach becomes increasingly difficult to implement as the propagation distance increases. An additional complication is that the required time delay varies if the object is moving radially.

The third approach is to produce a reference beam having a constant frequency shift relative to the transmitted beam, rather than sending the reference beam through a delay line. The size of the frequency shift for this approach would be equal to the product of the scan rate  $\gamma$  and the round-trip propagation time to the virtual range-reference plane. A disadvantage of this approach is that it requires a coherence length that is long compared with the distance to the target rather than the range extent of the target.

Because of the difficulties encountered with coherent detection at long ranges and because of the reduced hardware requirements for direct detection, development began on direct-detection-based methods for obtaining  $U(z)$ .

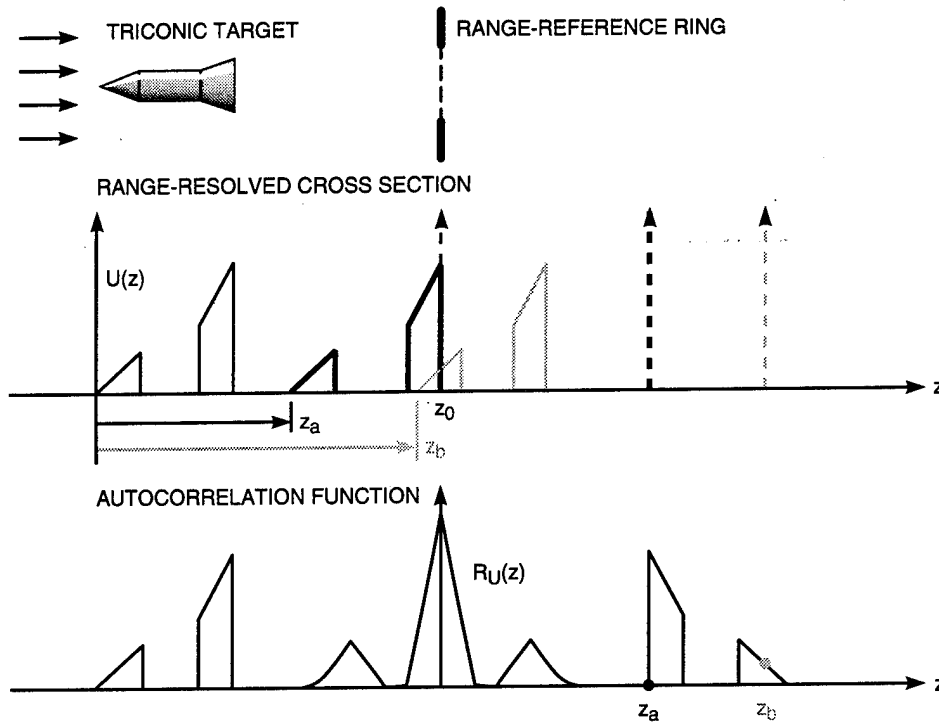


Figure 18. Pictorial illustration of how a range-reference plane produces the range-resolved laser radar cross section.

#### 4.5 PHASE RECOVERY

In considering how the direct-detection wavelength-decorrelation technique could be extended to the measurement of  $U(z)$ , note that by the autocorrelation theorem  $R_U(z)$  contains the same information as the magnitude of the Fourier transform of  $U(z)$ . If the phase  $\phi(f_z)$ , which is defined such that

$$\tilde{U}(f_z) = |\tilde{U}(f_z)| \exp[i\phi(f_z)] \quad , \quad (84)$$

were known, then  $\tilde{U}(f_z)$  would be completely determined and  $U(z)$  could be found through inverse Fourier transformation. Therefore, methods that yield  $U(z)$  must provide the Fourier phase information. It would be particularly interesting if  $\phi(f_z)$  could be found by processing the speckle intensity data. The hardware complexities and other difficulties associated with coherent detection could then be traded for more sophisticated signal processing.

Two general approaches exist for obtaining phase information from the intensity signal. The first approach is to take the autocorrelation function  $R_U(z)$ , obtained from calculating the spectral density, and attempt to recover the phase by applying well-known iterative phase-retrieval algorithms [51,52]. In these algorithms, known constraints are applied iteratively in the spatial and Fourier-transform domains. The

constraints in the spatial domain are that  $U(z)$  is a nonnegative function with finite support, that is, zero-valued outside of its range extent. In the Fourier-transform domain, the constraint is that the Fourier magnitude is known. Iterative phase retrieval has been applied to wavelength-decorrelation data with good success [37], but in general the method is not guaranteed to converge to the correct solution and does not use all available information. For these reasons other methods for recovering  $\phi(f_z)$  were investigated.

The second general approach is to analyze the original data by using more sophisticated signal-processing techniques in the hope that additional information about the phase can be extracted from the intensity signal. The basis for this optimism is that  $U(z)$  appears explicitly in Eq. (72) and information about the Fourier phase  $\phi(f_z)$  may have been lost in taking the magnitude-squared when the spectral density defined by Eq. (36) was calculated. By using the random-process representation of the signal from Section 4.3, any potential signal-processing algorithm can be tested to see if it yields more information about the Fourier phase. The first inclination might be to modify Eq. (36) by not taking the magnitude when squaring or to use different frequency arguments for the two factors. It can be shown, however, that the spectral density is the only second-order moment of  $\tilde{E}(f)$  that is nonzero. The next logical choice is to calculate a third-order moment.

The bispectral density is a third-order moment and the natural extension of the spectral density to two dimensions [53–55]. The application of bispectral signal processing to wavelength-decorrelation data is described in detail in the literature [37]. In summary, this work shows that bispectral analysis allows recovery of the Fourier phase of  $U(z)$  to within a linear phase factor and to within a global sign flip. The linear phase factor corresponds to an arbitrary range offset so that the distance to the target cannot be determined. The global sign flip corresponds to a sign ambiguity in the direction of increasing range.

Because the bispectral density is a higher-order moment than the spectral density, it will be estimated with less accuracy than the spectral density for the same number of realizations of the random process. Consequently, the Fourier phase will be determined less accurately than the Fourier magnitude. It was found that an effective application of bispectral analysis was in calculating an initial estimate of  $U(z)$  to be used in the iterative phase-retrieval algorithm.

An interesting parallel between spectral analysis and bispectral analysis points to another potential application of bispectral analysis. Just as calculating the spectral density of the fluctuating speckle intensity yields the autocorrelation function of  $U(z)$ , calculating the bispectral density of the fluctuating speckle intensity yields the real part of the triple correlation function of  $U(z)$ . The triple correlation function is an extension of the autocorrelation function to two dimensions and contains information about the Fourier phase that is lost in the autocorrelation function. Even a highly speckled estimate of the real part of the triple correlation function arrived at through a small number of realizations of the speckle intensity may be useful for pattern matching or automatic object-recognition algorithms.

## 5. WAVELENGTH-DECORRELATION MEASUREMENTS

Up to this point the report has concentrated on the theoretical aspects of wavelength decorrelation. Wavelength decorrelation will now be investigated from an experimental point of view, beginning by describing the laboratory setup, then verifying the fundamental concepts of wavelength decorrelation through a series of laboratory measurements. At the end of this section, some potential applications of the wavelength-decorrelation technique in target discrimination are explained.

### 5.1 LABORATORY LAYOUT

Figure 19 shows a schematic diagram of the optical setup. Because the objective was to prove the wavelength-scanning concept, off-the-shelf equipment was used whenever possible. The commercially available tunable laser that best fit the requirements was a Coherent, Inc., 899-29 Ti:sapphire ring laser pumped by a Coherent, Inc., Innova 200 argon-ion laser. The Ti:sapphire is an actively stabilized single-frequency ring laser that can produce a coherence length greater than 100 m. This coherence length is more than adequate because it is large compared to the range extent of targets of interest. (Because the wavelength-decorrelation technique can be implemented by using direct detection of the speckle intensity, the total propagation distance to and from the target can be much greater than the coherence length of the laser, which makes this technique attractive for remote-sensing applications.)

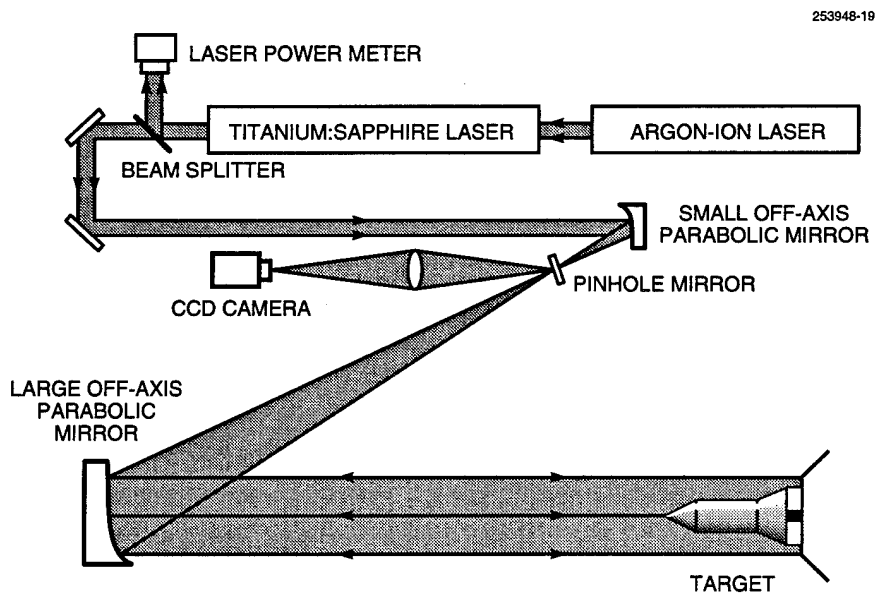


Figure 19. Schematic of optical system.

The Ti:sapphire laser can scan continuously in frequency over a range of approximately 30 GHz, which implies, by Eq. (56), a range resolution of 5 mm. It also operates in a computer-controlled frequency-stepping mode that uses an internal wavemeter for feedback. In this mode, it can be stepped over a range of more than 15 THz to yield a range resolution of better than 10  $\mu\text{m}$ . The stepping mode is slow compared to the scanning mode; the stepping mode was chosen, however, to demonstrate submillimeter range resolutions in the initial measurements.

After the beam exits the Ti:sapphire laser, it is directed into the beam-expanding telescope. A small fraction of the power is diverted into a power meter before entering the telescope to monitor any fluctuations in laser power during a scan. The telescope simulates far-field illumination by flood-illuminating the target with an expanded collimated laser beam. This telescope consists of a pair of off-axis parabolic mirrors that provide a beam-expansion ratio of 25 $\times$  and a maximum beam diameter of 22.5 cm. The expanded collimated beam illuminates a target assembly that incorporates a Newport Corp. PM500 computer-controlled rotation stage for precise angular positioning.

The telescope also serves as the collector for the receiver. Backscattered light from the target is collected by the large off-axis parabolic mirror (as shown in Figure 19) and reflected toward the pinhole mirror at the focal point of the telescope. The pinhole mirror directs the backscattered light into the detector leg of the telescope, at the same time passing the strong outgoing beam through the pinhole without scattering stray light into the detector. Thus, the pinhole mirror serves as a low-scatter, high-efficiency beamsplitter for observing the speckle pattern in the neighborhood of the monostatic observation direction. The pinhole also acts as an optical spatial filter, which is typically used for improving the spatial quality of a laser beam.

Because a far-field configuration is being simulated, the speckle pattern must be observed at the focal plane, or Fourier plane, of the large parabolic mirror. Here, parallel incoming rays converge to localized points of light, each having a position corresponding to the direction of propagation of the rays. Only rays that propagate parallel to the telescope axis (which include the outgoing beam and exactly retroreflected light) pass through the pinhole. Only backscattered light traveling in directions near the monostatic observation direction reaches the pinhole mirror.

The detector cannot be placed at the focal point because it would block the outgoing beam. Therefore, the pinhole mirror reflects the light away from the telescope axis so that the speckle pattern can be imaged onto the detector array with a lens, as depicted in Figure 19. Besides relaying the speckle pattern at the focal plane to the detector plane, the lens provides a magnification or demagnification  $M$  of the speckle pattern for optimal use of the detector array.

A Photometrics Ltd. scientific-grade CCD camera was selected for the detector because of its low noise, high linearity, and high dynamic range. The CCD contains  $512 \times 512$  pixels that are  $27 \mu\text{m} \times 27 \mu\text{m}$  in size. The speckle size on the CCD array is an important consideration; it must be larger than the pixel size so that speckle-intensity variations can be resolved. By replacing the distance  $R$  in the formula  $d_{\perp} = \lambda R/D$  for the speckle size  $d_{\perp}$  with the focal length  $f$  of the lens or mirror, this formula can be applied to the situation when the far field is simulated with a lens or a mirror. An additional factor of  $M$  must be included to account for magnification of the speckle pattern in the relay optics of the detector leg. Therefore, the appropriate expression for the speckle size at the detector plane is  $d_{\perp} = \lambda Mf/D$ . In our optical system, the focal length  $f$  of the primary mirror is 2 m, and the operating wavelength  $\lambda$  of the laser

is approximately  $0.75 \mu\text{m}$ . Consequently, for a transverse target size of  $D = 5 \text{ cm}$  and a magnification of  $M = 8$ , the average speckle size at the detector plane is approximately  $240 \mu\text{m}$ . Thus, the speckle lobes are well resolved, and the total number of speckles on the CCD array (or realizations of the random process) is greater than 1000 in this situation.

The disadvantage of the Photometrics CCD camera is that it requires over one full second to read out the entire array. This slow framing rate, along with the slow frequency-stepping rate of the laser, causes a typical 1024-point scan to take approximately 1 hr. Any motion of the speckle pattern arising from mechanical vibrations or air turbulence during this period will degrade the measurements. For this reason, the entire optical assembly is mounted on a vibration-isolated optical table, and the optical assembly is enclosed within a turbulence shroud. Future increases in the data-acquisition rate will greatly reduce the effects of turbulence and vibrations. For example, the system described is inefficient because the full  $512 \times 512$  array is read and then decimated to a  $32 \times 32$  array to sample each speckle approximately once on average. Little advantage is gained by processing the information from every pixel (as long as the light level is high) because uncorrelated estimates are necessary for averaging.

## 5.2 DEMONSTRATION OF FUNDAMENTAL CONCEPTS

The optical setup will now be used to demonstrate the basic relations between the wavelength dependence of speckle and the physical properties of the object being illuminated. The natural procedure for investigating wavelength decorrelation experimentally is to illuminate various objects with the tunable laser, observe the effect of varying the laser frequency on the speckle intensity, and look for any differences in behavior that might be linked to physical differences between the objects. It is assumed that the magnification of the lens in the detector leg is sufficient for producing a spatially well-resolved speckle pattern on the CCD array. Figure 20 illustrates the frequency dependence of the speckle intensity (at a single pixel in the CCD array) for three objects: a 4-cm-radius sphere, a 10-cm-long cone, and a 10-cm-long triconic. The cone and the triconic are illuminated nose-on. The frequency scan length is 100 GHz, which corresponds to a very small frequency modulation of approximately 0.025% of the carrier frequency.

Observe that the speckle intensity in Figure 20 fluctuates radically as the laser frequency varies. The term *wavelength decorrelation* applies because the speckle intensity decorrelates as the frequency or wavelength of the laser is changed. The decorrelation frequency  $\Delta\nu_D$  is a measure of the frequency offset at which one can no longer make a reasonable estimate of the new speckle intensity given the value of the original speckle intensity.

Let us investigate the differences among the three frequency scans. The most obvious distinction is the longer decorrelation frequency  $\Delta\nu_D$  for the sphere, which has an illuminated range extent  $L$  equal to 4 cm compared with the cone and triconic, which both have an illuminated range extent  $L$  equal to 10 cm. These plots indicate an inverse proportionality between range extent and decorrelation frequency and experimentally confirm Eq. (33); that is, the calculated decorrelation frequencies of  $\Delta\nu_D = 3.75 \text{ GHz}$  for the sphere and  $\Delta\nu_D = 1.5 \text{ GHz}$  for the cone and triconic agree well with the measured intensity scans.

Next, compare the details of the curves for the cone and the triconic. Although both objects have the same decorrelation frequency, a higher proportion of the high-frequency component is found in the curve

corresponding to the triconic. This fact suggests that a relation exists between the object shape and the spectral content of the fluctuating intensity sequence.

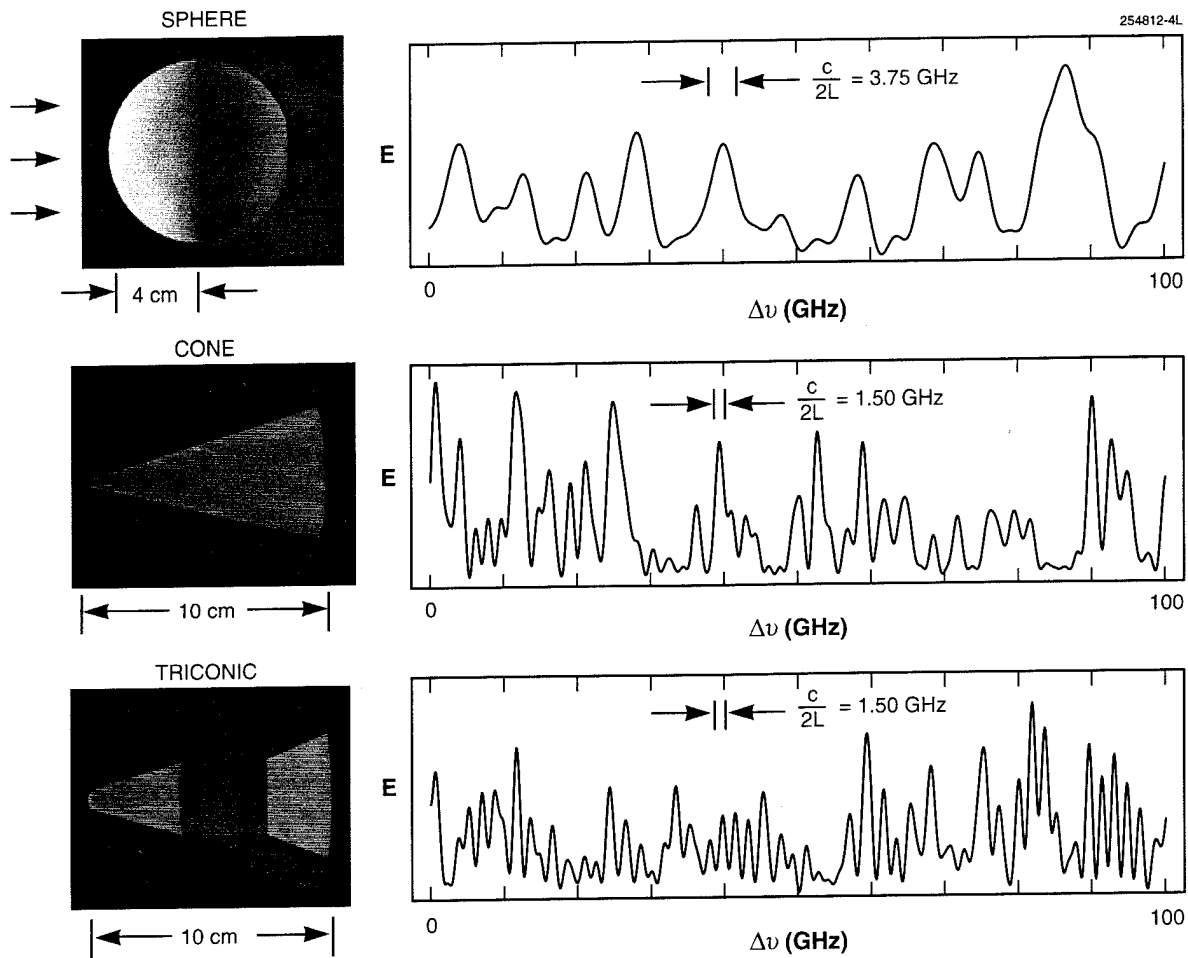


Figure 20. Speckle intensity versus laser frequency. These plots illustrate that the statistical properties of the fluctuating speckle intensity are related to the size and the shape of the illuminated object. As the illuminated range extent  $L$  increases, the decorrelation frequency  $c/(2L)$  decreases. The spectral makeup of the curves depends on the shape of the object.

To illustrate the information obtained through spectral analysis, the sharp-tipped triconic shown in Figure 21 will be used. The triconic is coated with retroreflective paint to provide a strong return signal relative to the scatter from the supporting structure. A triconic was chosen because it produces an interesting nose-on illumination signature that is also relatively easy to interpret. The lengths  $L_1$ ,  $L_2$ , and

$L_3$  of the three segments, beginning with the nose, are 3.5 cm, 4.0 cm, and 2.5 cm, respectively, and the cone half-angles  $\alpha_{c_1}$ ,  $\alpha_{c_2}$  and  $\alpha_{c_3}$  are  $20^\circ$ ,  $0^\circ$ , and  $25^\circ$ , respectively. For this series of measurements, the laser-frequency step size  $\Delta v_{\text{step}}$  is 500 MHz to satisfy the Nyquist condition for sampling, as given in Eq. (34). The total scan length  $B$  is 500 GHz, which yields a theoretical range resolution of approximately 0.3 mm.

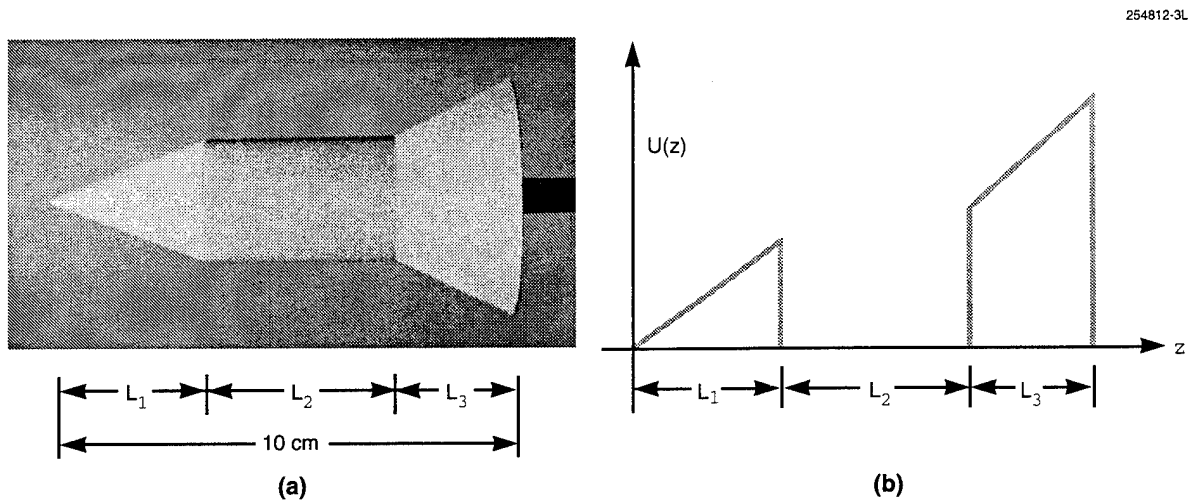


Figure 21. Triconic target model and corresponding theoretical range-resolved laser radar cross section for nose-on illumination.

Figure 22(a) is a plot of the estimated spectral density of the fluctuating speckle intensity obtained at a single pixel in the CCD array. Although the curve is highly speckled, several spectral features can be extracted. For example, the spectrum appears to have finite support, or to be zero-valued outside a certain range of frequencies, indicating that the fluctuating speckle signal is band-limited. There is also a region and its mirror image containing a null in the data. (This null arises because the lengths  $L_1$  and  $L_3$  of the two conical components of the triconic are both smaller than the length  $L_2$  of the cylindrical component.) A better estimate of the spectral density can be obtained by averaging the results from additional pixels. Figures 22(b), 22(c), and 22(d) contain plots for averages of 10, 100, and 1024 pixels, respectively. These plots demonstrate that the estimate of the spectral density smoothes out substantially as more averages are performed, but the smoothing effect is nonlinear. The degree of smoothing is actually proportional to the square root of the number of speckles sampled. As previously mentioned, calculating the spectral density for every pixel would not improve the estimate of the spectral density significantly because the intensity at neighboring pixels is correlated when the speckle is oversampled.

The final estimate of the spectral density shown in Figures 22(d) and 23 has an interesting shape that is related to the shape of the object. In interpreting this spectral density, first consider the meaning of

the abscissa. Normally, a spectral density is calculated for a function of time. Consequently, the spectral density is a function of frequency. Although the fluctuating speckle signal can be treated as a function of time, the more basic parameter is the laser-frequency offset  $\Delta\nu$ . If the scan is smooth and continuous, these two quantities are related through the scan rate  $\gamma$  by  $\Delta\nu = \gamma t$ . In our measurements, however, the frequency is stepped, and the time between steps varies from step to step. Therefore, the signal is treated as a function of laser-frequency offset. Consequently, this spectral density is a function of time because now a Fourier transform of a function of frequency is being taken. Note that the time of 0.67 nsec from the origin to the end of the curve in Figure 23 corresponds to the propagation time for light to travel the 20-cm distance from the tip of the cone to the base and back again. This fact indicates that the spectral-density curve contains range information. The range is obtained by multiplying half of the time offset by the speed of light; the factor of one-half accounts for the round-trip path length. The resulting range scale for the abscissa is shown at the bottom of Figure 23.

Now that the abscissa has been related to the range  $z$ , the information content carried by the shape of the curve is investigated. Because the strength of the intensity return from a radar is proportional to the target's cross section and because the spectral-density signature is a function of range  $z$ , this signature should contain information about the range-resolved laser radar cross section  $U(z)$  of the target. The spectral-density signature is clearly not a direct measurement of  $U(z)$ , however. Some properties of the spectral-density curve are now noted that help relate it to the range-resolved laser radar cross section: (1) It has a width equal to twice the range extent of the target, (2) it is an even function, and (3) its highest value occurs at the origin. These are all properties of autocorrelation functions. These observations lead experimentally to the hypothesis, already derived in Section 4, that the ensemble-averaged spectral density is proportional to the autocorrelation function  $R_U(z)$  of the range-resolved laser radar cross section  $U(z)$ .

To confirm this hypothesis experimentally,  $U(z)$  must be determined separately. Figure 21(b) contains a theoretical plot of  $U(z)$  for on-axis viewing of a Lambertian triconic with the appropriate dimensions. The null in the middle region occurs because the surface of the cylindrical segment is not illuminated for nose-on viewing. The theoretical autocorrelation function of this particular range-resolved laser radar cross section appears in the central region of the autocorrelation curve shown at the bottom of Figure 18. A close similarity is observed between this central region and the averaged spectral density shown in Figure 22(d).

To compare these functions more closely,  $f(\theta)$  must be known for the triconic at the angles of incidence for the two conical components; that is,  $\theta_1 = 70^\circ$  and  $\theta_3 = 65^\circ$ . A technique for measuring  $f(\theta)$  is illustrated in the Appendix. The figure in the Appendix shows the monostatic properties for a retroreflective paint that is similar in behavior to the 3M 7210 retroreflective paint used to coat the triconic. Note that the  $f(\theta)$  function curves upward at the edges and that  $f(70^\circ)$  is larger than  $f(65^\circ)$  by approximately 50%. Another consideration in comparing experiment with theory is beam uniformity. In this measurement, the illuminating beam was nearly Gaussian, with an intensity drop of approximately 25% at the perimeter of the target. After accounting for the effect of a nonconstant  $f(\theta)$  and the effect of beam nonuniformity on  $U(z)$ , the autocorrelation function of  $U(z)$  was calculated by computer. Figure 23 compares this autocorrelation function with the averaged spectral density in Figure 22(d). The excellent agreement between experiment and theory indicates that the phenomenology for wavelength decorrelation is well understood.

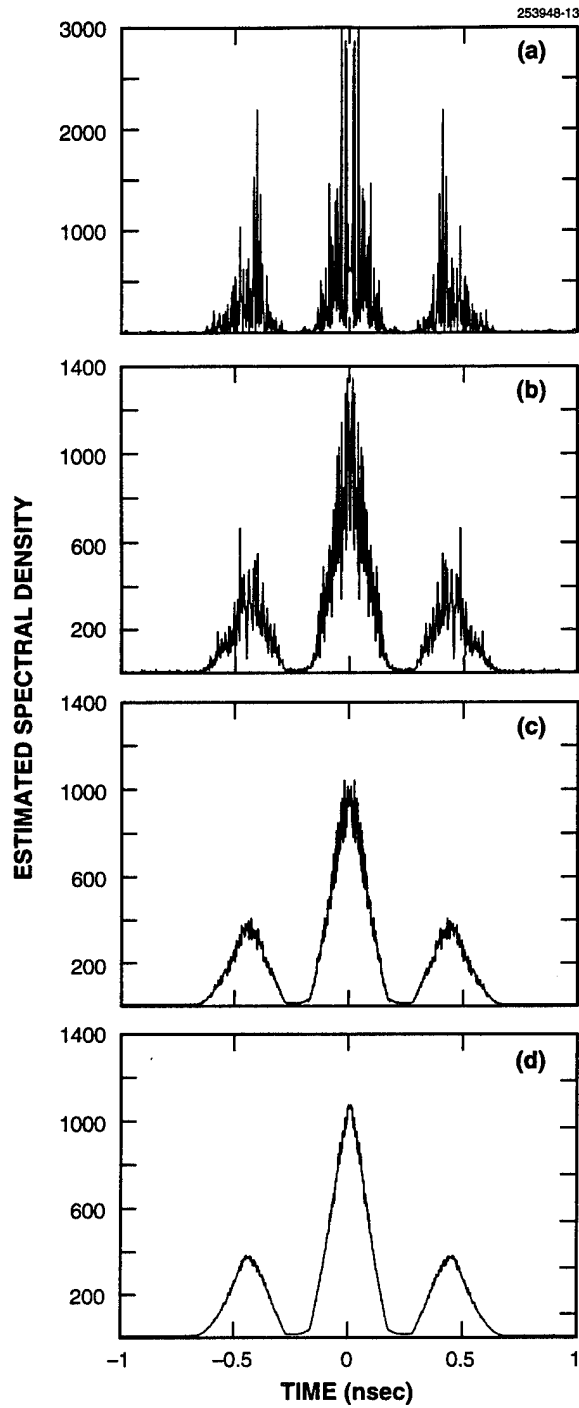


Figure 22. Estimated spectral density of the fluctuating speckle intensity produced by illuminating a 10-cm-long triconic target nose-on with a frequency-scanning laser: (a) 1 average; (b) 10 averages; (c) 100 averages; (d) 1024 averages. These curves illustrate the smoothing effect of averaging the individual spectral-density estimates obtained from multiple pixels in the CCD array.

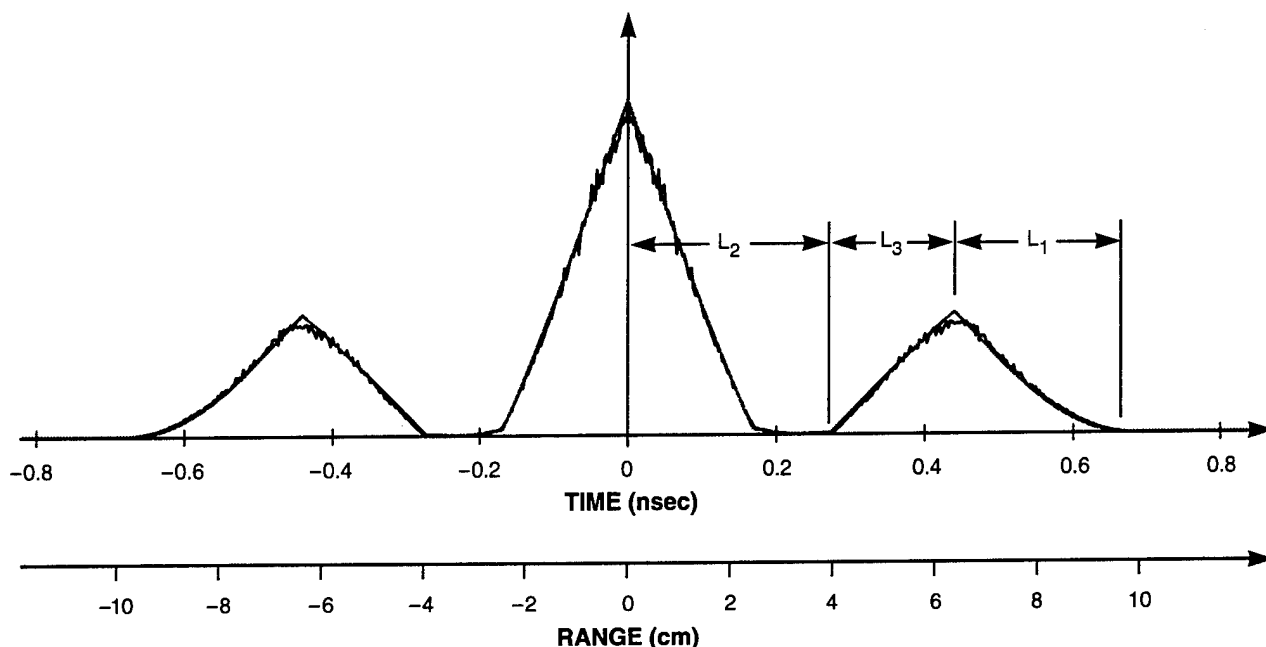


Figure 23. Comparison of the averaged spectral density displayed in Figure 22(d) with the autocorrelation function of the theoretical range-resolved laser radar cross section. Radial falloff in the intensity of the illuminating beam and non-Lambertian scattering from the surface of the triconic are accounted for in the theoretical curve.

### 5.3 MEASUREMENTS OF RANGE-RESOLVED LASER RADAR CROSS SECTION

We have shown both theoretically and experimentally that the wavelength-decorrelation technique allows measurement of the autocorrelation function  $R_U(z)$  of the range-resolved laser radar cross section  $U(z)$  of a target. As shown in the bottom of Figure 16,  $R_U(z)$  may be useful by itself for object-recognition purposes. We would also, however, like to be able to measure  $U(z)$  directly because  $U(z)$  can be more easily related to the physical properties of the object. As explained in the section on bispectral analysis, methods that yield measurements of  $U(z)$  must provide the Fourier phase  $\phi(f_z)$  in addition to the Fourier magnitude  $|\tilde{U}(f_z)|$  of the range-resolved laser radar cross section. Two techniques for measuring  $U(z)$ —a range-reference plane technique and bispectral signal processing—will now be demonstrated.

As described above, a range-reference plane provides a simple means for implementing the coherent-detection approach in a laboratory setting where the scattering object is physically accessible. Figure 24 is a typical laboratory setup with a range-reference ring located behind a spherical object. Figures 25 and 26 show experimental results obtained by using the range-reference-plane technique to measure  $U(z)$  for off-axis illumination of a cone and a cylinder, respectively. The laser-frequency step size is 1 GHz, and the total scan length is approximately 1 THz. This scan length results in a theoretical range resolution of 0.15 mm. Theoretical predictions of  $U(z)$  are shown for comparison; good agreement was achieved in the overall shape of these curves. The high-frequency oscillations in the data are the

result of approximating an ensemble average with a finite number of averages as well as with granularity in the retroreflective surface coating.

To further illustrate the high range resolution achievable using the wavelength-decorrelation technique, a step target with a number of flat surfaces separated by various distances, as shown in Figure 27(a), was constructed. This object has nine levels with a ratio of 1.4 between successive step heights. The individual steps range in value between 0.5 mm and 8.5 mm with a total range span of 24.6 mm. Figure 27(b) shows experimental results for a scan length of 2 THz. The resulting theoretical range resolution is 0.075 mm. All nine levels in the target are accounted for in the  $U(z)$  curve, and even the 0.5-mm step is well resolved, which clearly demonstrates submillimeter range resolution.

A disadvantage of using a range-reference plane is that the number of effective averages is less than one might initially expect. This lower number occurs because the surface of the reference plane must be diffuse, or rough on a wavelength scale. If the surface of the reference plane were optically smooth, it would produce a single bright spot at the detector plane, and the mixing between the reference signal and the target signal would be limited to a small region of the detector array. Although using a rough-surfaced reference plane does cause the reference signal to spread over the entire detector array, it also results in a speckled reference signal. Furthermore, because the reference plane has a small range extent when illuminated at normal incidence, the speckle-intensity pattern from the reference plane remains fairly constant over the entire frequency scan. It is known that the intensity distribution of a Gaussian speckle pattern obeys a decaying-exponential probability law [46]. Therefore, a large fraction of the area of the speckle pattern is dark, but there are also regions with intensity levels that are many times the mean. Consequently, the reference signal is weak over a large portion of the detector array. The strong reference signal from the bright regions will tend to dominate and reduce the effective number of speckle averages, resulting in higher fluctuations in the estimate of  $U(z)$  than would be otherwise expected.

The reference-plane technique can be modified so that the number of effective averages is not reduced. Ideally, the range-reference plane would be replaced by a single range-reference point; then there would be no speckle and no degradation in the averaging. The problem with using a single range-reference point is that it has zero laser radar cross section. Specular points from curved polished surfaces do have large cross sections, however, and the range-reference technique has also been implemented by using specular range-reference points with improved results.

The bispectral signal-processing technique will now be illustrated. As described in the section on bispectral analysis, information about the Fourier phase  $\phi(f_z)$  is actually carried by the fluctuating intensity signal, but this information is lost when the magnitude-squared of the Fourier transform is taken when calculating the spectral density. Bispectral signal processing, however, retains this phase information. Figure 28 presents reconstruction results for a 5-cm-long triconic target [37]. The estimates of  $U(z)$  (including postprocessing using one-dimensional phase retrieval) are indicated for both simulated and experimental data. These plots show good agreement with each other and with the theoretical plot of the range-resolved laser radar cross section for this particular object.

In addition to size and shape information, the range-resolved laser radar cross section also yields information about surface coatings [56]. Consider first the case in which the shape is known to be spherical. The setup shown in Figure 24 was used to measure  $U(z)$  for a 5-cm-diameter sphere. Figure 29 compares the results obtained for two different surface coatings, 3M 7210 retroreflective paint and Krylon 1402 heat-resistant paint. The theoretical  $U(z)$  curve for a Lambertian surface is shown for comparison.

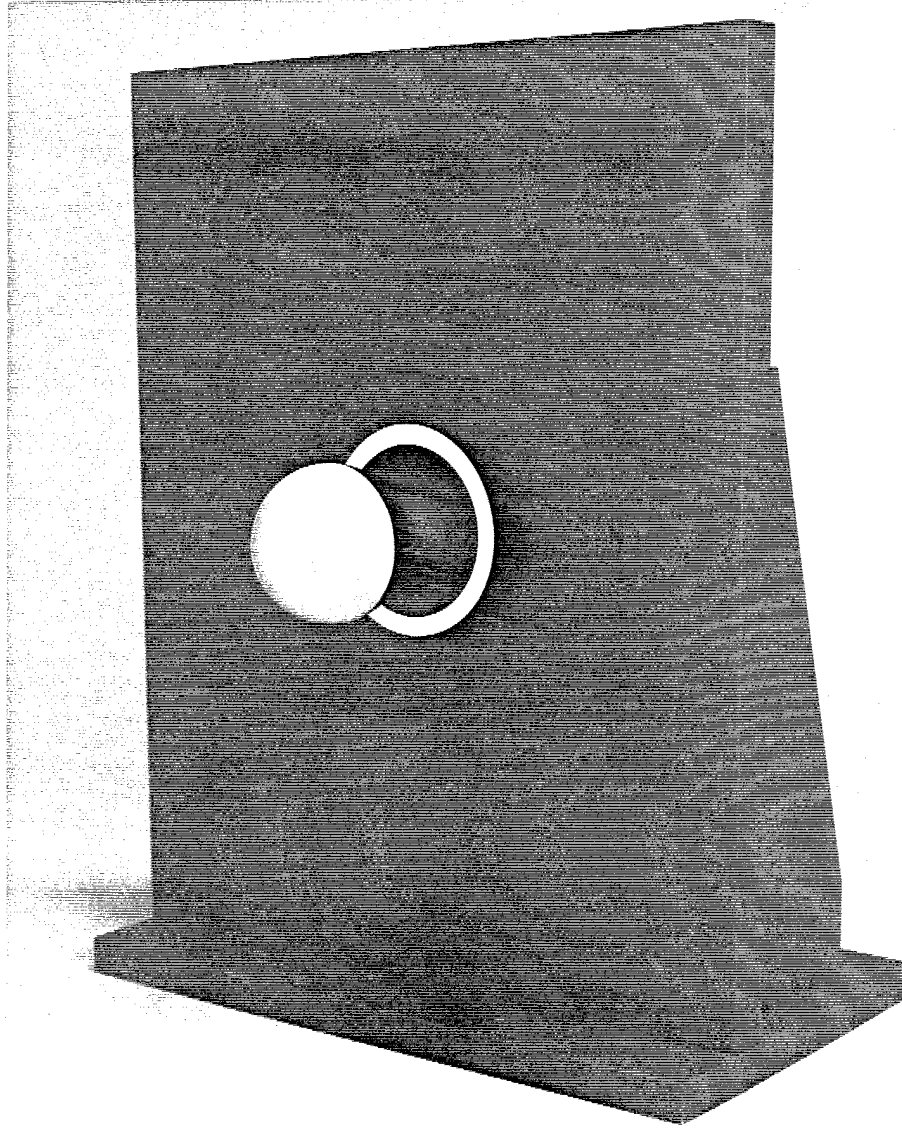


*Figure 24. A spherical target mounted in front of a range-reference ring. This type of setup provides a simple means for direct measurement of the range-resolved laser radar cross section.*

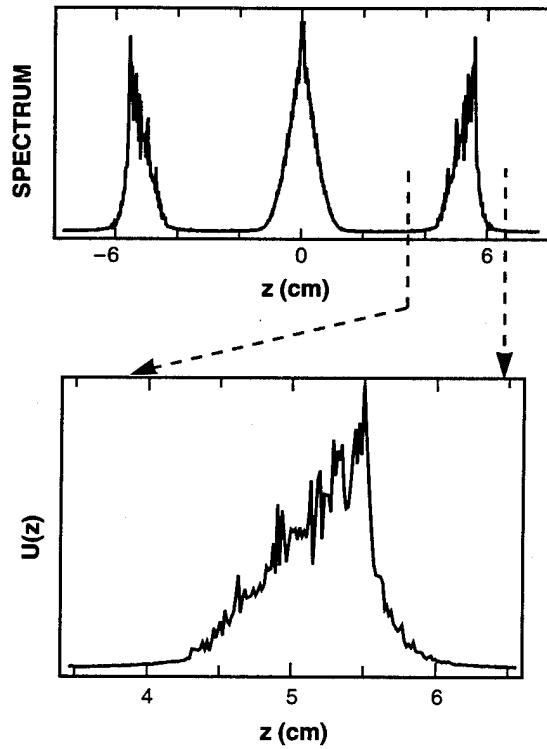
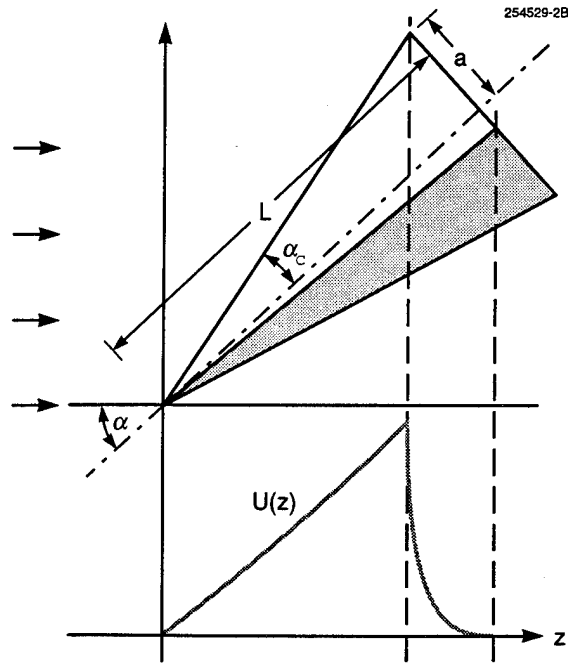


Figure 25. Experimental and theoretical range-resolved laser radar cross section for off-axis illumination of a cone at  $45^\circ$ . The cone has a length of 2.5 cm and a cone half-angle of  $15^\circ$ .

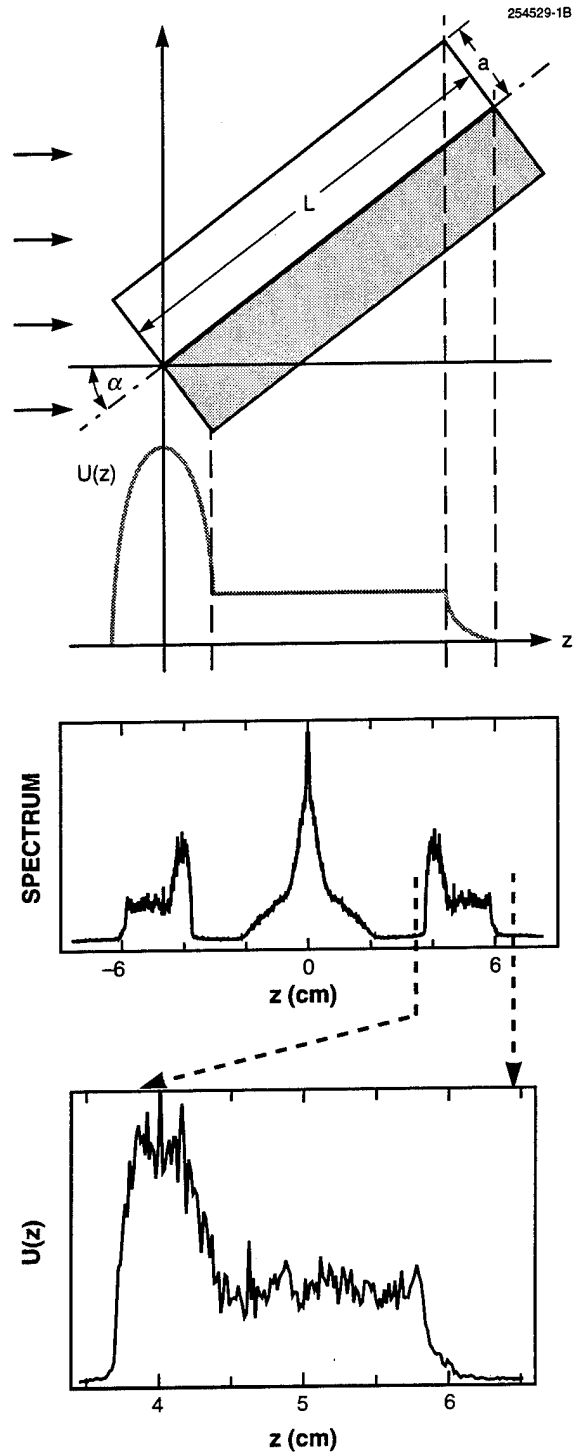
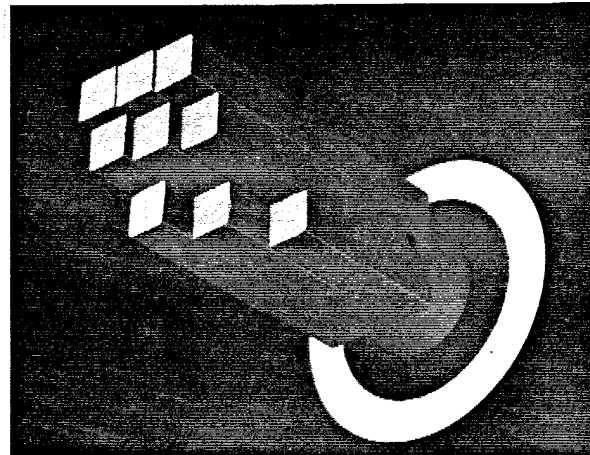
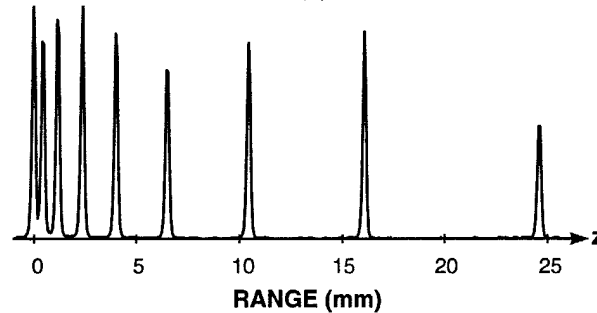


Figure 26. Experimental and theoretical range-resolved laser radar cross section for off-axis illumination of a cylinder at  $35^\circ$ . The cylinder has a length of 2.5 cm and a diameter of 1 cm.



(a)



(b)

Figure 27. Demonstration of submillimeter range resolution: (a) nine-step range-resolution target mounted in front of a range-reference ring; (b) experimentally measured range-resolved laser radar cross section. The step size increases by a factor of 1.4 between steps, beginning with a smallest step size of 0.5 mm.

There is a marked difference in the measured  $U(z)$  of the sphere for the two coatings. First,  $U(z)$  for the retroreflective paint is larger than  $U(z)$  for the heat-resistant paint by approximately 20 dB. Second, there is a difference in the shape of these two curves. In particular,  $U(z)$  for the heat-resistant paint rises sharply for values of  $z$  near the pole, where the angle of incidence  $\theta$  is small, which indicates that  $f(\theta)$  is larger for small angles of incidence. This result agrees with the independent measurement of  $f(\theta)$  presented in the Appendix, confirming that the wavelength-decorrelation technique can provide useful information about surface materials.

For the sphere, it is particularly easy to extract the surface-scattering information because each value of the range  $z$  maps into a single value of the angle of incidence  $\theta$ . This fact allows one to invert Eq. (11) for the range-resolved laser radar cross section of a sphere and to write  $f(\theta)$  explicitly as a function of  $U(z)$ :

$$f(\theta) = \frac{a}{8\pi^2 z^2} U(z) \Big|_{z=-a \cos \theta} \quad (85)$$

The above reasoning can also be applied to any axially symmetric object that is illuminated along the axis of symmetry. The range-resolved laser radar cross section then takes the general form given in Eq. (9), which can be solved for  $f(\theta)$ .

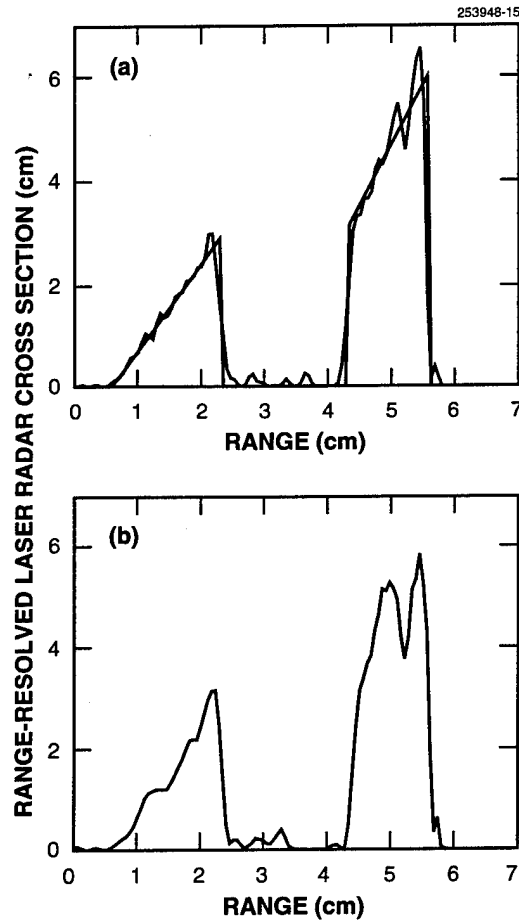


Figure 28. Reconstructions of the range-resolved laser radar cross section of a triconic target by using bispectral analysis of the speckle intensity: (a) simulated data; (b) measured data. The smooth line in part a represents the theoretical curve.

In the above situations, on-axis illumination of an axially symmetric target made it possible to determine  $f(\theta)$  from a single measurement of  $U(z)$ . An axially symmetric object is not needed, however, to

obtain useful information about  $f(\theta)$ . As a general rule, the object shape determines the position in range of the discontinuities in the  $U(z)$  curve, and differences in the angular-scattering properties from object to object produce slower variations and differences in the magnitude of the  $U(z)$  curve. Therefore, if two objects are known to have the same shape, variations in  $U(z)$  between these two objects can be related to differences in their surface-scattering properties. In addition, if the shape is known, surface properties can be estimated by determining the dominant angles of incidence contributing to a given value of range.

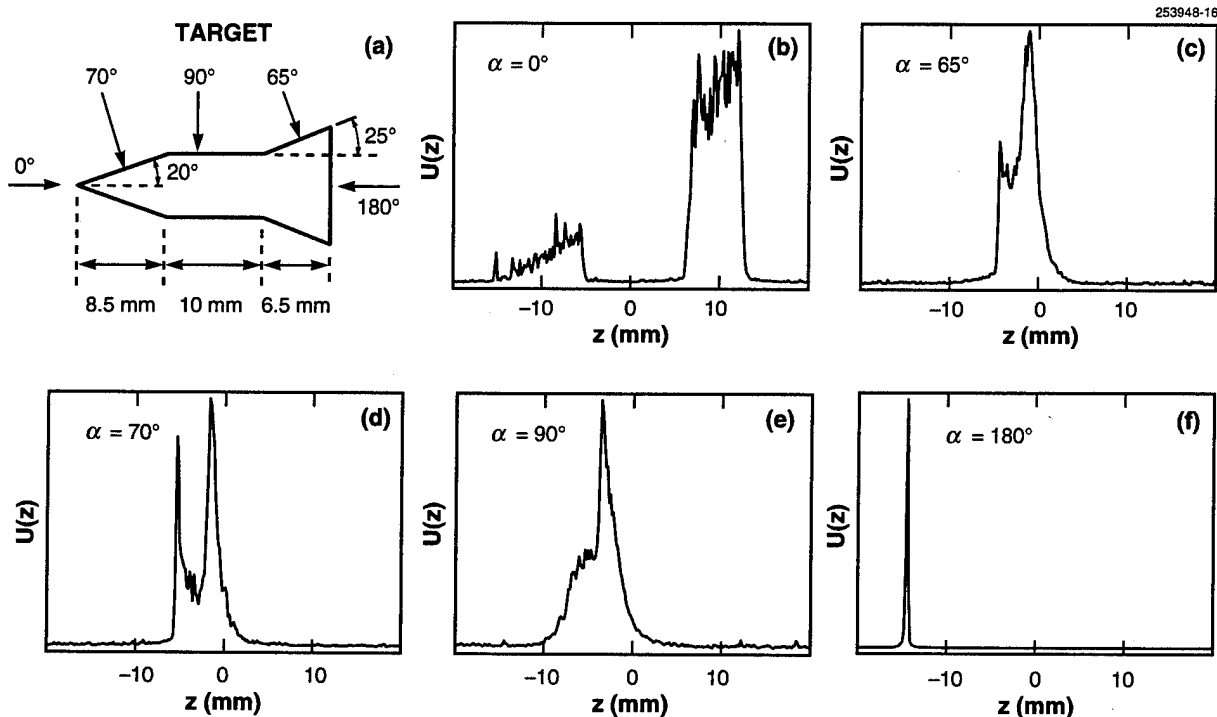


Figure 29. Measured range-resolved laser radar cross section of a sphere for two different surface materials: (a) 3M 7210 retroreflective paint; (b) Krylon 1402 heat-resistant paint; (c) theoretical result for a Lambertian surface. Each value of range  $z$  on the sphere corresponds to a unique value of the angle of incidence  $\theta$ , which allows  $f(\theta)$  to be measured.

#### 5.4 APPLICATIONS TO DISCRIMINATION

The wavelength-decorrelation technique offers information about the details of a target that can be used for target-discrimination or target-recognition purposes. In the simplest implementation of wavelength decorrelation, a single detector could be used to estimate the range extent  $L$  of the target by measuring the decorrelation frequency  $\Delta\nu_D$  and relating it to  $L$  through Eq. (33). Variations of  $L$  with time could then be related to the target's shape and angular dynamics.

Variations of the speckle intensity with laser frequency carry much more information about the target than its range extent  $L$  alone. For example, by simply calculating the power spectrum of the intensity variations from a single detector, a speckled estimate of the autocorrelation function of  $U(z)$  similar to the curve shown in Figure 22(a) is obtained. Even though curves from a single detector are highly speckled, it does appear that they will be useful in many pattern-recognition or target-classification applications. For example, these curves could be compared with a library of autocorrelation functions for various targets at different viewing angles, as illustrated by the curves shown in Figures 16(e) and 16(f). If speckle smoothing is required, it can be achieved by filtering out the high-frequency content (with an accompanying loss of resolution). Smoothing can also be achieved without giving up range resolution by using an array of detectors, as illustrated by the results in Figure 22. Figure 22(b) shows a significant improvement for a number as small as 10 detector elements.

The next level of sophistication in extracting target information from speckle intensity is to determine the functional form of the range-resolved laser radar cross section  $U(z)$  rather than just its autocorrelation function. For relatively short propagation distances, coherent-detection-based techniques may be feasible. For long propagation distances, however, direct-detection-based techniques such as iterative phase retrieval or bispectral analysis may be required for recovering the Fourier phase. Both of these phase-recovery techniques are based on ensemble-averaged quantities (or smoothed quantities) and therefore require sampling many speckle lobes to reduce statistical fluctuations to acceptable levels. The minimum acceptable number of detector elements required for estimating  $U(z)$  for discrimination applications has not yet been determined.

As mentioned in Section 4, another approach to discrimination based on bispectral analysis has reduced requirements on the number of detector elements. This approach is to develop automatic-target-recognition algorithms based on features in the triple correlation space of  $U(z)$ . The advantage of this approach is that it retains the Fourier-phase information carried by the intensity signal, but it does not require the additional steps and the large number of detector elements necessary for smoothing the triple correlation function in the process of recovering the Fourier phase.

Given that the range-resolved laser radar cross section  $U(z)$  can be determined, its functional form offers information about the size, shape, and surface-scattering properties of a target that is useful for discrimination purposes. Some ways of extracting target information from the functional form of  $U(z)$  will now be discussed. Section 3 showed that basic geometric shapes (such as the sphere, the disk, the cone, and the cylinder) have distinctive signatures. These signatures might be used as a means of identifying targets by their shape or determining the component shapes making up a target. For example, one could distinguish between the conical target in Figure 25 and the cylindrical target in Figure 26 from their measured range-resolved laser radar cross sections. In general, a cone and a cylinder can be identified by the sloped straight line and the flat straight line, respectively, in their  $U(z)$  signatures.

Let us look more closely at how the theoretical  $U(z)$  curves in Figure 25 and Figure 26 are related to the shape of the target. In Figure 25, the discontinuity in the slope of the  $U(z)$  curve occurs at the range value  $z$  where the range plane no longer intersects a complete cone. As  $z$  increases past this point, the curve decreases rapidly at first, then falls off gradually to zero at the value of  $z$  corresponding to the last illuminated region of the cone. Similar statements apply to the cylinder in Figure 26. Observe that the disk-shaped end cap on the cylinder produces a large, elliptically shaped hump in the  $U(z)$  curve. The end

points of this hump clearly mark the boundaries of the disk in range. As a general result, then, discontinuities in the slope of the  $U(z)$  curve, or discontinuities in the  $U(z)$  curve itself, are related to physical points or regions on the surface of a target. The position of these discontinuities in range can be used to extract information about target dimensions. Thus, much can be learned about the size and shape of a target from the functional form of its range-resolved laser radar cross section measured at a single aspect angle. As described, knowledge of the functional form of  $U(z)$  also provides information about the angular-scattering properties of surface materials. This information can help determine the type of surface materials covering different regions of the target.

In many instances, the aspect angle of the target changes as a function of time. As the number of aspect angles increases, the shape and dimensions of the target can be determined with more certainty and increasingly complicated targets characterized. Figure 30 shows a set of measurements of  $U(z)$  for a 2.5-cm-long triconic target model illuminated at angles of  $0^\circ$ ,  $65^\circ$ ,  $70^\circ$ ,  $90^\circ$ , and  $180^\circ$ . These particular angles were chosen because they correspond to on-axis illumination of the triconic and to broadside illumination of each of the segments of the triconic. The abrupt jumps in  $U(z)$  correspond to the reflections from the perpendicular surface components. Because features of a range-resolved laser radar cross-section signature can be related to physical properties of the target, these features might serve as a basis for automatic-target-recognition algorithms.

The applications to discrimination described thus far are based on knowledge of the range-resolved laser radar cross section  $U(z)$  or on quantities that can be derived from  $U(z)$ , such as the range extent  $L$ , the autocorrelation function of  $U(z)$ , and the triple correlation function of  $U(z)$ . Because  $U(z)$  is an ensemble-averaged quantity that is independent of the microscopic surface detail of a particular target, it is necessary to obtain different realizations of the random process to determine  $U(z)$ . It has been shown that an effective means for obtaining these realizations is to use additional detector elements located in the vicinity of the monostatic direction. Although this approach provides the necessary realizations for ensemble averaging, additional information about the 3D structure of the target can be extracted if one keeps track of the position in space of the detector elements (see Section 6).

Additional applications to discrimination based on the material in Section 6 are now described. One of the simplest techniques (see Section 6.1.2 on remote orientation sensing of planar surfaces) is to observe any global translation of the speckle pattern that occurs as the wavelength is scanned. For a nonrotating target, the direction and speed of speckle translation provide information about the orientation of the target with respect to the radar line of sight. From the direction of speckle motion, one can determine which end of the target is closer to the laser radar and which way the target is pointing azimuthally. From the speed of speckle motion, one can estimate the target's aspect angle.

The next level of sophistication in the signal processing is to form a 3D data array by stepping the laser in frequency and sampling the speckle pattern at each frequency. The 3D Fourier transform of this data set yields the 3D autocorrelation function of the target shape (see Section 6.1.1). This autocorrelation function is rich in target information; in particular, its support is closely related to the shape of the target. Given a library of target shapes, it would be relatively straightforward to match the support of the measured autocorrelation function to the support of the autocorrelation function of objects in the library. This procedure could determine the target orientation and target size as well as confirm the target identity through verifying its shape.

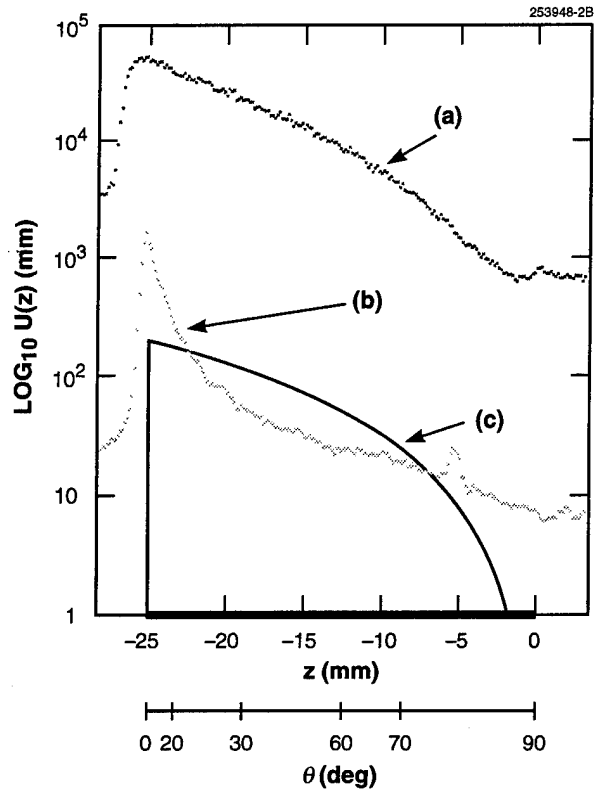


Figure 30. Range-resolved laser radar cross section of a triconic target illuminated at various aspect angles  $\alpha$ : (a) target dimensions; (b)  $\alpha = 0^\circ$ ; (c)  $\alpha = 65^\circ$ ; (d)  $\alpha = 70^\circ$ ; (e)  $\alpha = 90^\circ$ ; (f)  $\alpha = 180^\circ$ .

Finally, a 3D target image can be formed by using coherent detection to retain the Fourier-phase information or by recovering this information through advanced signal processing. A concept for 3D phase retrieval based on the support of the autocorrelation function is described in Section 6.1.3.

Because of the slow data acquisition rate of the laboratory system, measurements have been limited to stationary targets. Much faster scans are necessary for rotating targets. Whether the wavelength-based techniques described here will someday be applied to moving targets at large distances will depend on future developments in the area of high-power frequency-agile lasers.

## 6. 3D IMAGING

This section will demonstrate two general techniques for 3D imaging based on the wavelength dependence of speckle. The first technique, referred to as speckle-pattern sampling, is based on the concept of sampling the 3D Fourier space of the object. The second technique, referred to as the image-speckle technique, obtains lateral image information through conventional imaging and range information from the wavelength dependence of speckle formed at the image plane.

### 6.1 SPECKLE-PATTERN SAMPLING

Speckle-pattern sampling is a direct extension of the wavelength-decorrelation technique for measuring  $U(z)$ . As with wavelength decorrelation, speckle-pattern sampling obtains range information from the wavelength dependence of speckle. The difference is in the way that the signal is processed from different pixels within the detector array. Wavelength decorrelation is based on a statistical approach where the signal from individual pixels serves to produce an ensemble of realizations of a random process for averaging purposes. Speckle-pattern sampling, on the other hand, is a direct approach; it keeps track of the pixel location and uses this information to resolve the object laterally.

Because speckle-pattern sampling is a direct approach, the resulting 3D image is speckled in nature. This speckle, however, does not present a significant problem in most cases because we are trying to determine the location of the scattering point, that is, the size and shape of the object's surface rather than the scattering amplitude of individual points on the surface. Speckle may cause dropouts in the reconstruction of the surface, but an effective means of reducing the number of dropouts is to subdivide the data into two or more smaller sets and to form 3D images from each set (with a corresponding loss of resolution). These images can then be combined to reduce the total number of dropouts. In this sense, speckle-pattern sampling becomes statistical in nature, but the number of realizations possible in practice is very limited because of the amount of data required for each image.

A basic speckle-pattern sampling measurement proceeds as follows: the speckle pattern is measured with a CCD array at each of a set of equally spaced laser frequencies, the individual frames are stacked to form a 3D data array, and a 3D Fourier transform is performed on this data array. This process yields the 3D autocorrelation function of the 3D image of the object. Just as the range-reference-plane implementation of wavelength decorrelation allows the determination of  $U(z)$  rather than its autocorrelation function, a reference point can be used in speckle-pattern sampling to produce the 3D image rather than the autocorrelation function of this image.

The preceding description of a speckle-pattern-sampling measurement applies to low-resolution 3D imaging. As the frequency-scan length of the laser and the solid angle subtended by the detector array increase, the resolution of the 3D image increases, and there is mixing of the wavelength dependence and the spatial dependence of the speckle pattern. More sophisticated data acquisition and signal processing are then required.

Section 6.1.1 contains a general treatment of speckle-pattern sampling; this treatment not only covers these high-resolution effects but it also treats near-field effects caused by noncollimated illumination and detector arrays located in the near-field of the object. Section 6.1.1 also illustrates the

technique through a series of 3D imaging measurements based on speckle-pattern sampling. Section 6.1.2 describes and demonstrates a simplified technique based on the speckle-pattern sampling concept for remote measurement of the normal vector to a surface. Section 6.1.3 describes the basis for a 3D phase-retrieval technique that has the potential for eliminating the need for a reference point in some applications. This technique is illustrated for a discrete set of scattering points.

### 6.1.1 3D Imaging

The mathematical framework for 3D imaging will now be developed. In Figure 31,  $P_s$  is a monochromatic point source of wavelength  $\lambda$  at  $(x_s, y_s, z_s)$  and  $P_r$  is a reflective reference point located near the object at  $(x_r, y_r, z_r)$ . The objective here is to write the resultant complex amplitude  $V(x_d, y_d, z_d; \lambda)$  for the optical field at the observation point  $P_d$  due to scattering from the object's surface  $h$ . To do so, consider first the contribution from a scattering point  $P_h$  located at  $(x_h, y_h, z_h)$  on the surface. Assume that single scattering dominates so that light travels from  $P_s$  to  $P_h$  to  $P_d$  without being scattered from  $P_h$  to other points on the surface before reaching  $P_d$ . The phase delay at  $P_d$  due to this propagation pathlength is obtained by adding together the distance  $R_{sh}$  from  $P_s$  to  $P_h$  and the distance  $R_{hd}$  from  $P_h$  to  $P_d$  and multiplying the sum by the wavenumber  $k = 2\pi/\lambda$ . The resulting contribution to the complex amplitude at  $P_d$  is

$$V_h(x_d, y_d, z_d; \lambda) = g(x_h, y_h, z_h) \exp\left[-i \frac{2\pi}{\lambda} (R_{sh} + R_{hd})\right] \quad , \quad (86)$$

where  $g(x_h, y_h, z_h)$  is a complex scattering function whose magnitude represents the strength of the contribution from  $P_h$  and whose phase accounts for any phase change caused by scattering. The complex amplitude  $V(x_d, y_d, z_d; \lambda)$  resulting from the entire surface is obtained by summing the individual contributions from all scattering points. Because the scattering function is zero-valued at locations where there are no scattering points, this summation can be written as an integral over all space:

$$V(x_d, y_d, z_d; \lambda) = \int \int \int_{-\infty}^{\infty} g(x_h, y_h, z_h) \exp\left[-i \frac{2\pi}{\lambda} (R_{sh} + R_{hd})\right] dx_h dy_h dz_h \quad , \quad (87)$$

where

$$R_{sh} = \sqrt{(x_s - x_h)^2 + (y_s - y_h)^2 + (z_s - z_h)^2} \quad (88)$$

and

$$R_{hd} = \sqrt{(x_h - x_d)^2 + (y_h - y_d)^2 + (z_h - z_d)^2} \quad (89)$$

If the height profile of the scatterer is represented by  $h(x, y)$ , then the scattering function can be written in the form

$$g(x, y, z) = a(x, y) \delta[z - h(x, y)] \quad , \quad (90)$$

where  $a(x, y)$  is the complex amplitude of the given contribution to  $V(x_d, y_d, z_d; \lambda)$ . Our primary objective in 3D imaging is to recover the functional form of  $h(x, y)$ ; recovery of  $a(x, y)$  is a more difficult problem that is actually of less interest.

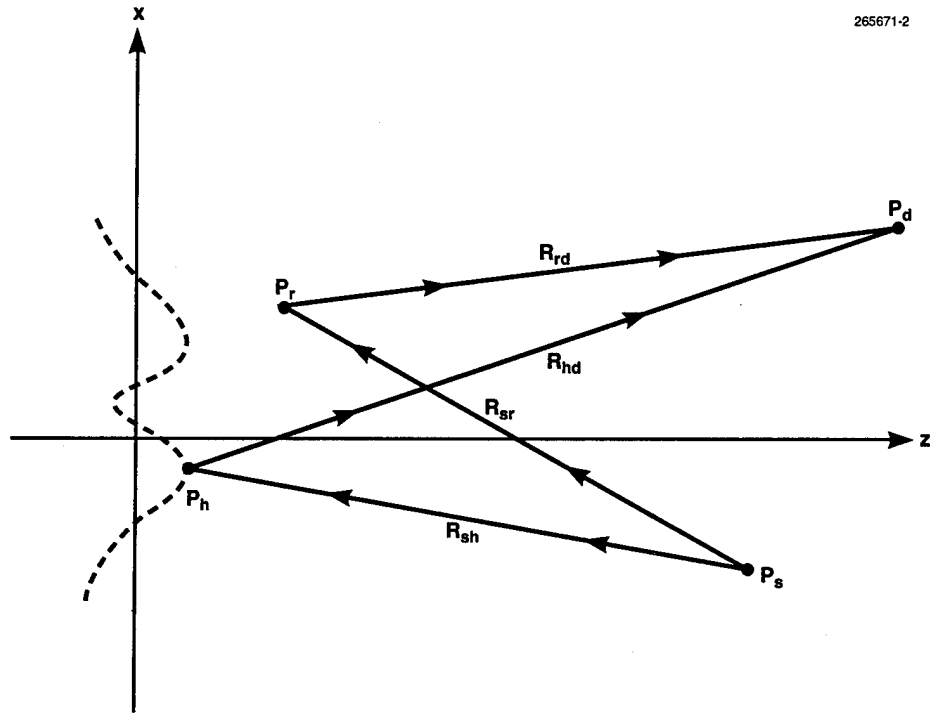


Figure 31. Coordinate system for the analysis of 3D imaging showing the source point  $P_s$ , scattering point  $P_h$ , reference point  $P_r$ , and observation point  $P_d$ .

Some comments are in order about the interpretation of Eq. (90). First, let us consider shadowing effects. Shadowing of one surface region by another is accounted for by requiring that  $a(x, y)$  be zero-valued for points on the surface that are not simultaneously illuminated by  $P_s$  and viewed by  $P_d$ . Therefore, there is an implicit dependence in  $a(x, y)$  on the position of points  $P_s$  and  $P_d$ . This dependence of  $a(x, y)$  on  $P_s$  and  $P_d$  also includes the factors  $1/R_{sh}$  and  $1/R_{hd}$  to account for the falloff of field strength with distance from the source point  $P_s$  to the scattering point  $P_h$  and from  $P_h$  to the observation point  $P_d$ , respectively. (In most practical situations, the points  $P_s$  and  $P_d$  are far enough from the object so that one can replace  $R_{sh}$  by  $R_s$  and  $R_{hd}$  by  $R_d$ , where  $R_s$  is the distance from  $P_s$  to the origin and  $R_d$  is the distance from the origin to  $P_d$ .) Besides the dependence on distance,  $a(x, y)$  also includes a factor that accounts for the angular dependence of the scattering strength. [In the spirit of Sections 3 and 4, this angular

dependence of scattering could be written in terms of the BRDF of a surface patch at  $P_h$ , but this level of detail is unnecessary for the reconstruction of  $h(x, y)$ .]

The complex amplitude  $V_r(x_d, y_d, z_d; \lambda)$  corresponding to the reference point  $P_r$  is obtained by substituting

$$g(x, y, z) = g_r \delta(x - x_r) \delta(y - y_r) \delta(z - z_r) \quad (91)$$

into Eq. (87). Without loss of generality,  $P_r$  can be placed at the origin of the coordinate system. Then the distances  $R_{sr}$  and  $R_{rd}$  in the complex exponential can be replaced by  $R_s$  and  $R_d$ , which are the distances from  $P_s$  to the origin and from the origin to  $P_d$ , respectively. The resulting expression for the contribution to the complex amplitude from the reference point  $P_r$  is

$$V_r(x_d, y_d, z_d; \lambda) = g_r \exp\left[-i \frac{2\pi}{\lambda} (R_s + R_d)\right] \quad (92)$$

The total complex amplitude at the observation point  $P_d$  is the sum of  $V$  from Eq. (87) and  $V_r$  from Eq. (92). The quantity measured at the observation point is the magnitude squared of this total complex amplitude:

$$I(x_d, y_d, z_d; \lambda) = |V(x_d, y_d, z_d; \lambda) + V_r(x_d, y_d, z_d; \lambda)|^2 = I_1 + I_2 + I_3 + I_4 \quad (93)$$

where

$$I_1 = |g_r|^2 \quad (94)$$

$$I_2 = |V(x_d, y_d, z_d; \lambda)|^2 \quad (95)$$

$$I_3 = g_r^* \exp\left[i \frac{2\pi}{\lambda} (R_s + R_d)\right] V(x_d, y_d, z_d; \lambda) \quad (96)$$

and

$$I_4 = I_3^* \quad (97)$$

Proceeding further with the analysis and exploring the meaning of the four terms in Eq. (93) requires approximation of the distances given by the square roots in Eqs. (88) and (89). First consider the distance  $R_{hd}$  between the scattering point and the observation point in Eq. (89). If  $R_{hd}$  is written in the form

$$R_{hd} = R_d \sqrt{1 + \frac{x_h^2 + y_h^2 + z_h^2 - 2x_h x_d - 2y_h y_d - 2z_h z_d}{R_d^2}} \quad (98)$$

expanded in a binomial series, and the terms kept up to second order in  $R_h$ , where  $R_h$  is the distance from the origin to the scattering point, the approximation

$$R_{hd} \approx R_d - \frac{x_h x_d + y_h y_d + z_h z_d}{R_d} + \frac{x_h^2 + y_h^2 + z_h^2}{2R_d} - \frac{(x_h x_d + y_h y_d + z_h z_d)^2}{2R_d^3} \quad (99)$$

is obtained. A corresponding expression for the distance  $R_{sh}$  between the source point and the scattering point is obtained by replacing the subscript  $d$  with the subscript  $s$  in Eq. (99).

The first two terms on the right side of Eq. (99) correspond to the usual far-field approximation, except that the integration is normally limited to the  $x$ - $y$  plane so that  $z_h = 0$ . The combination of the first three terms can be made to look like the standard Fresnel approximation

$$\sqrt{(x_h - x_d)^2 + (y_h - y_d)^2 + z_d^2} \approx z_d + \frac{(x_h - x_d)^2 + (y_h - y_d)^2}{2z_d} \quad (100)$$

by setting  $z_h = 0$  and approximating  $R_d$  by  $z_d$  in some instances. The standard Fresnel approximation is inherently paraxial in nature, that is, valid only for small values of  $x_d$  and  $y_d$ . The advantage of Eq. (99) is that it is equally valid for all observation directions, being a wide-angle Fresnel approximation.

Let us compare the range of validity of the far-field approximation and wide-angle Fresnel approximation. A validity condition for the far-field approximation can be obtained by requiring that second-order terms in  $R_h/R_d$  introduce phase errors of less than  $\pi/2$  for any direction of observation and any offset direction of  $R_h$  from the origin:

$$R_d > \frac{2R_h^2}{\lambda} \quad (101)$$

The corresponding condition for the wide-angle Fresnel approximation is obtained by requiring that fourth-order terms in  $R_h/R_d$  satisfy the same restrictions:

$$R_d^3 > \frac{R_h^4}{2\lambda} \quad (102)$$

Large observation distances are required to satisfy the far-field condition for practical object sizes. For example, with a wavelength of  $\lambda = 0.8 \mu\text{m}$ , an observation distance of  $R_d = 250 \text{ m}$  is required for  $R_h = 10 \text{ mm}$ . The wide-angle Fresnel approximation, however, is valid at a distance of  $R_d = 185 \text{ mm}$ .

Equation (99) and the corresponding expression for  $R_{sh}$  can now be substituted into Eq. (87) to proceed with the evaluation of the terms  $I_1$ - $I_4$  in Eqs. (94)-(97). Rather than using the full wide-angle Fresnel approximation at this point, we begin with the far-field approximation as given by the first two terms in Eq. (99). Although the far-field approximation places severe restrictions on object size for practical observation distances, it does provide the framework for introducing the basic principles of 3D imaging. The size restrictions can be overcome in practice by illuminating the object with collimated light and placing a Fourier-transform lens in front of the detector array to simulate far-field observation. Later the full wide-angle Fresnel approximation will be used to study near-field effects and to show that good images can be obtained much further into the near field than would be expected by Eq. (101).

With the far-field assumption, Eq. (87) becomes

$$V(x_d, y_d, z_d; \lambda) = \exp\left[-i\frac{2\pi}{\lambda}(R_s + R_d)\right] \int_{-\infty}^{\infty} \int_{-\infty}^{\infty} \int_{-\infty}^{\infty} g(x_h, y_h, z_h) \times \exp\left\{-i\frac{2\pi}{\lambda}\left[x_h\left(\frac{x_s}{R_s} + \frac{x_d}{R_d}\right) + y_h\left(\frac{y_s}{R_s} + \frac{y_d}{R_d}\right) + z_h\left(\frac{z_s}{R_s} + \frac{z_d}{R_d}\right)\right]\right\} dx_h dy_h dz_h \quad (103)$$

The coordinates  $(x_s, y_s, z_s)$  for the source point and  $(x_d, y_d, z_d)$  for the observation point occur in Eq. (103) in terms of the direction cosines  $l_s = x_s/R_s$ ,  $m_s = y_s/R_s$ ,  $n_s = z_s/R_s$ ,  $l_d = x_d/R_d$ ,  $m_d = y_d/R_d$ , and  $n_d = z_d/R_d$ . Therefore, except for the implicit dependence of  $g(x, y, z)$  on  $R_s$  and  $R_d$  to account for the falloff of field strength with distance, the integral in Eq. (103) is independent of observation distance  $R_d$  and source-point distance  $R_s$ , as long as these points are in the far field. Note that the integral in Eq. (103) is the 3D Fourier transform of  $g(x, y, z)$ , allowing us to rewrite Eq. (103) as

$$V(x_d, y_d, z_d; \lambda) = \exp\left[-i\frac{2\pi}{\lambda}(R_s + R_d)\right] \tilde{g}(f_x, f_y, f_z) \quad (104)$$

where the tilde represents a Fourier transform and the spatial frequencies  $f_x$ ,  $f_y$ , and  $f_z$  are related to the direction cosines and the wavelength by

$$f_x = -\frac{l_s + l_d}{\lambda} \quad (105)$$

$$f_y = -\frac{m_s + m_d}{\lambda} \quad (106)$$

and

$$f_z = -\frac{n_s + n_d}{\lambda} \quad (107)$$

In writing these equations note that the values of  $f_x$ ,  $f_y$ , and  $f_z$  are not independent; any two of the three direction cosines determines the third direction cosine through the relations  $l_d^2 + m_d^2 + n_d^2 = 1$  and  $l_s^2 + m_s^2 + n_s^2 = 1$ . Substitution of Eq. (104) into Eqs. (95) and (96) yields

$$I_2 = |\tilde{g}(f_x, f_y, f_z)|^2 \quad (108)$$

and

$$I_3 = g_r^* \tilde{g}(f_x, f_y, f_z) \quad (109)$$

Equation (93) then takes the form

$$I(x_d, y_d, z_d; \lambda) = |g_r|^2 + |\tilde{g}(f_x, f_y, f_z)|^2 + g_r^* \tilde{g}(f_x, f_y, f_z) + g_r \tilde{g}^*(f_x, f_y, f_z) \quad (110)$$

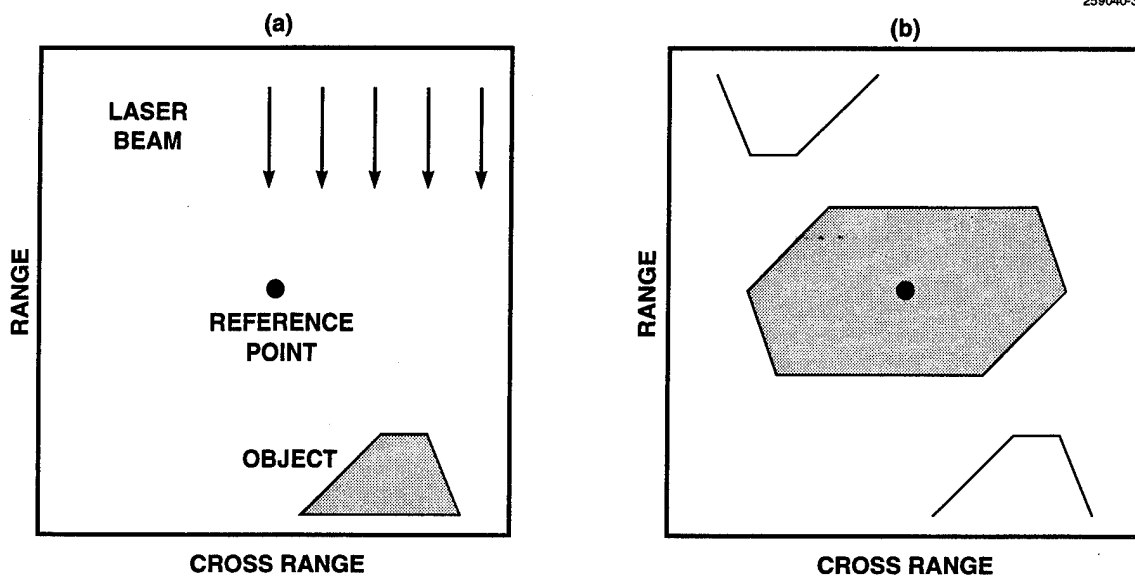


Figure 32. Interpretation of the 3D Fourier transform of a speckle-pattern-sampling data set: (a) object scene; (b) components in image space representing the 3D Fourier transform of the four terms in Eq. (110).

The significance of the four terms  $I_1-I_4$  in Eq. (110) is explained by performing an inverse Fourier transform to convert from Fourier space to object space. The inverse Fourier transforms of the individual terms are illustrated in Figure 32. The scattering surface, shown in Figure 32(a), is located below and to the right of the reference point. Because  $I_1$  is a constant, its inverse Fourier transform is a 3D  $\delta$ -function located at the origin of object space in Figure 32(b). By the autocorrelation theorem, the inverse Fourier transform of  $I_2$  is the 3D autocorrelation function of  $g(x, y, z)$ . The support of this autocorrelation function is shown in the region surrounding the origin in Figure 32(b). The inverse Fourier transform of  $I_3$  gives the desired quantity  $g(x, y, z)$ , multiplied by  $g_r^*$ , which occurs in the lower right-hand quadrant. Because  $I_4$  is the complex conjugate of  $I_3$ , its inverse Fourier transform is  $g_r g^*(-x, -y, -z)$ . This term corresponds to the inverted image in the upper left-hand quadrant of Figure 32(b).

It is evident from Figure 32 that the desired image will be separated from the central autocorrelation function and from the inverted image if the object is far enough away from the reference point. Given that this condition is satisfied, the image can be isolated by selecting the appropriate region of the inverse Fourier transform. It is sufficient for the object to be removed from the reference point by the object's illuminated range extent or by its cross-range extent in any cross-range direction. Another approach is to use a strong reference point just outside of the object that produces  $I_3$  and  $I_4$  terms that swamp out the autocorrelation term  $I_2$ . Yet another technique for isolating the image term is to incorporate a phase shift  $\phi$  in the reference beam [33] and to measure the speckle pattern using two different phase-shift values  $\phi = 0$  and  $\pi$ . By subtracting these two frames for each value of  $\lambda$ , the  $I_1$  and  $I_2$  terms cancel, leaving terms  $I_3$  and  $I_4$ . The advantage of this approach is that the reference point can be located closer to the object so that

Fourier space can be sampled at a lower sampling rate while achieving the same resolution. Still more sparse sampling of Fourier space is possible if the reference point can be located inside of the object or can be made to appear so. Then by using the additional phase-shift values of  $\phi = \pi/2$  and  $3\pi/2$ , the  $I_4$  term can also be eliminated.

Having shown that the undesired terms can be eliminated, let us concentrate on the  $I_3$  term from here on. By Eqs. (105)–(107), the Fourier space of  $I_3$  can be sampled by varying the observation directions  $l_d$  and  $m_d$  and the wavelength  $\lambda$ . To find the values of  $l_d$ ,  $m_d$ , and  $\lambda$  necessary for sampling a given point in Fourier space, Eqs. (105)–(107) are used to write  $\lambda$  in terms of the spatial frequencies  $f_x$ ,  $f_y$ , and  $f_z$ :

$$\lambda = -2 \frac{l_s f_x + m_s f_y + n_s f_z}{f_x^2 + f_y^2 + f_z^2} \quad (111)$$

Then by rewriting Eqs. (105) and (106) as

$$l_d = -l_s - \lambda f_x \quad (112)$$

and

$$m_d = -m_s - \lambda f_y \quad (113)$$

$\lambda$  from Eq. (111) can be substituted into Eqs. (112) and (113) to express all three quantities  $l_d$ ,  $m_d$ , and  $\lambda$  in terms of the desired spatial frequencies  $f_x$ ,  $f_y$ , and  $f_z$ . Once  $I_3$  has been sampled correctly in Fourier space,  $I_3(f_x, f_y, f_z)$  can be inverse Fourier transformed to obtain the image:

$$P(x, y, z) = \int_{-\infty}^{\infty} \int_{-\infty}^{\infty} \int_{-\infty}^{\infty} I_3(f_x, f_y, f_z) \exp[i2\pi(f_x x + f_y y + f_z z)] df_x df_y df_z \quad (114)$$

As previously mentioned, this image is given by

$$P(x, y, z) = g_r^* g(x, y, z) \quad (115)$$

for far-field sampling of  $I_3$ , which is the basic result on which 3D imaging is founded.

The remainder of Section 6.1.1 treats the sampling of Fourier space in greater detail, discusses image resolution, categorizes aberrations resulting from incorrect sampling of Fourier space, describes the effect of near-field sampling of  $I_3$  on the image in Eq. (115), and demonstrates 3D imaging through a series of measurements.

**Ewald Sphere.** Equation (111) is of particular interest because it is the basis for the Ewald-sphere construction (Figure 33) mentioned in Section 1; for a constant wavelength  $\lambda$ , Eq. (111) describes the surface of the Ewald sphere of reflection, which is a sphere of radius  $1/\lambda$  in  $(f_x, f_y, f_z)$  space with one point of the surface of the sphere passing through the origin and the center of the sphere offset in the direction of incoming illumination from  $P_s$ . One way of sampling Fourier space is to keep  $\lambda$  constant and to vary the direction of illumination, then, as shown by the limiting sphere in Figure 33, it is possible to sample a volume in Fourier space of twice the radius of the Ewald sphere of reflection.

In the applications considered here, however, the illumination direction is fixed and Fourier space is sampled by changing the radius of the sphere through control of the laser wavelength  $\lambda$ . For the purpose of this discussion, assume that the source point lies on the positive  $z$ -axis; then  $l_s = m_s = 0$  and  $n_s = 1$  and Eq. (111) simplifies to

$$\lambda = -\frac{2f_z}{f_x^2 + f_y^2 + f_z^2} \quad (116)$$

259040-2

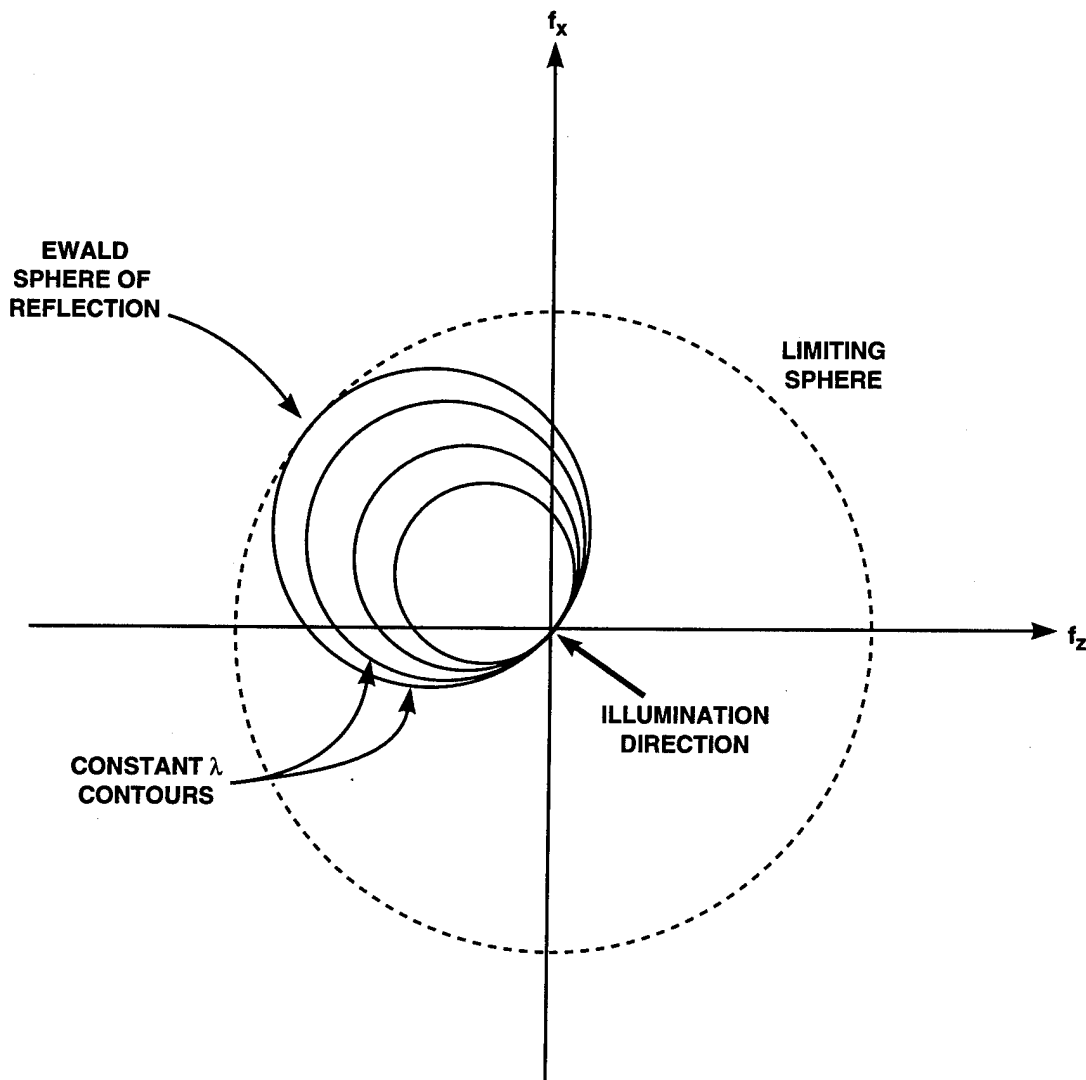


Figure 33. Ewald-sphere construction for the sampling of a scattering object's 3D Fourier space. Constant  $\lambda$  contours lie on the surface of the Ewald sphere of reflection. The limiting sphere is obtained by varying the illumination direction.

Let  $\lambda_0$  be the nominal wavelength about which  $\lambda$  is varied, then by Eq. (116) the spatial frequency  $f_{z_0}$  where the Ewald sphere corresponding to  $\lambda_0$  touches the negative  $f_z$  axis is  $f_{z_0} = -2/\lambda_0$ . Thus, in sampling 3D Fourier space there is an offset in the  $f_z$  direction of twice the radius of the Ewald sphere. To produce uniform steps in  $f_z$  in the sampling of Fourier space, one must be able to vary the radius of the Ewald sphere in a linear manner. Consequently, we control the laser frequency  $\nu = c/\lambda$ , which is proportional to the sphere radius, rather than the wavelength  $\lambda$ . Furthermore, in practice it is more convenient to monitor the frequency shift  $\Delta\nu$  from the frequency  $\nu_0 = c/\lambda_0$  than the absolute frequency  $\nu = \nu_0 + \Delta\nu$ . Given these preferences, the radius of the Ewald sphere is written as

$$\frac{1}{\lambda} = \frac{1}{\lambda_0} + \frac{\Delta\nu}{c} \quad (117)$$

Equation (116) can now be recast in the form

$$\Delta\nu = -\frac{c}{2} \left( \Delta f_z + \frac{f_x^2 + f_y^2}{f_{z_0} + \Delta f_z} \right), \quad (118)$$

where  $\Delta f_z = f_z - f_{z_0}$  is spatial-frequency offset from  $f_{z_0}$ . Equation (118) gives the frequency shift  $\Delta\nu$  required to sample a given point in Fourier space.

Finally, the position  $(x_d, y_d)$  of the observation point can be related to the spatial frequencies  $f_x$  and  $f_y$  by writing Eq. (112) as

$$f_x = -\frac{l_d}{\lambda} = -\frac{x_d}{\lambda R_d} \quad (119)$$

and Eq. (113) as

$$f_y = -\frac{m_d}{\lambda} = -\frac{y_d}{\lambda R_d} \quad (120)$$

For completeness, Eq. (107) is rewritten as

$$f_z = -\frac{1+n_d}{\lambda} = -\frac{1}{\lambda} \left( 1 + \sqrt{1 - \frac{x_d^2 + y_d^2}{R_d^2}} \right) \quad (121)$$

**Resolution.** In a 3D imaging measurement, Fourier space is sampled by measuring the speckle pattern over the surface of the detector array as the laser frequency is stepped. The larger the scan length and detector-array size, the larger the volume of sampled Fourier space and the better the resolution that is achievable. As the volume of sampled Fourier space increases, however, the range and cross-range information begin to mix and cause aberrated images if unaccounted for. We now use Eqs. (118)–(120) to address the issue of image resolution and to investigate aberrations caused by improper sampling of Fourier space.

First, let us assume a low-resolution measurement defined as one producing images with range and cross-range resolution-cell lengths that are large compared with the wavelength  $\lambda$ . For these measurements, the ranges of  $\Delta v$ ,  $x_d$ , and  $y_d$  in Eqs. (118)–(120) are limited. Consequently, the quadratic term in Eq. (118) can be neglected and the  $\lambda R_d$  factor in Eqs. (119) and (120) can be considered constant. With these assumptions, expressions for the resolution-cell size can be written by calculating the width of the 3D point-spread function corresponding to the size of the sampled region of Fourier space. Let the length of the frequency scan be denoted by  $B$  and the length of the detector array in the  $x$  and  $y$  directions be denoted by  $w_x$  and  $w_y$ , respectively. Then from Eqs. (118)–(120), the ranges of Fourier space that are sampled in the  $f_x$ ,  $f_y$ , and  $f_z$  directions, respectively, are  $F_x = w_x/(\lambda_0 R_d)$ ,  $F_y = w_y/(\lambda_0 R_d)$ , and  $F_z = 2B/c$ . The corresponding resolutions (obtained by Fourier transforming a 3D rect function having these widths in the three dimensions and selecting values of the arguments of the resulting sinc functions that correspond to the first null) are

$$\Delta x = \frac{1}{F_x} = \frac{\lambda_0 R_d}{w_x} \quad , \quad (122)$$

$$\Delta y = \frac{1}{F_y} = \frac{\lambda_0 R_d}{w_y} \quad , \quad (123)$$

and

$$\Delta z = \frac{1}{F_z} = \frac{c}{2B} \quad . \quad (124)$$

Equation (124) is equivalent to Eq. (56), which was derived previously in the treatment of the wavelength-decorrelation technique. The resolutions given by Eqs. (122)–(124) also correspond to the spacing between planes in image space that result from using FFTs to calculate the 3D Fourier transform.

For comparison of the transverse resolution given by Eqs. (122) and (123) with conventional imaging, rewrite Eq. (122) in terms of the half angle  $\theta_d$  of light received by the detector array as

$$\Delta x = \frac{\lambda_0}{2 \sin \theta_d} \quad . \quad (125)$$

If  $\theta_d$  is interpreted as the cone half angle of light received by a microscope objective, then Eq. (125) is the standard expression relating image resolution to the numerical aperture  $N.A. = \sin \theta_d$  of a microscope. Thus, conventional imaging and speckle-pattern sampling have similar resolution capabilities for general images.

Speckle-pattern sampling, however, actually provides the capability for enhanced resolution of objects consisting of a small number of separated points. For example, the distance between a reference point and an object point can be measured to a resolution better than the grid spacing given by Eqs. (122)–(124) by taking advantage of the phase information inherent in the interference pattern. One approach to extracting this information is to subdivide the voxel representing the image of the point by calculating a discrete Fourier transform (DFT) at points inside this voxel and to search for the location

where the maximum value of the DFT occurs, thus determining the location of the scattering point. A similar procedure can be employed for opaque diffuse scattering objects considered in this report that are represented by a height function  $h(x, y)$ . Improved range resolutions have been demonstrated by performing a DFT in the  $z$  direction on data sets where speckle frames have been Fourier transformed in the  $x$  and  $y$  directions using a 2D FFT.

Finally, let us consider sampling requirements for nonaliased imaging. Equation (34) for the maximum frequency-step size allowed for an object of range extent  $L$  (including the reference point) is repeated here for convenience:

$$\Delta v_{\text{step}} \leq \frac{c}{4L} \quad (126)$$

Corresponding expressions for the maximum pixel dimensions  $p_x$  and  $p_y$  of the detector array in the  $x$  and  $y$  directions (assuming no decimation of pixels in a frame) are given in terms of the cross-range extents  $D_x$  and  $D_y$  of the object (including the reference point) as

$$p_x \leq \frac{\lambda_0 R_d}{2D_x} \quad (127)$$

and

$$p_y \leq \frac{\lambda_0 R_d}{2D_y} \quad (128)$$

**Aberrations.** Equations (118)–(120) are now examined for the effects of continuing to sample on a rectangular grid in measurement space as resolution increases. Techniques are also described for correcting the resulting aberrations in the 3D image. These aberrations are divided into three types, referred to as *wavelength aberration*, *detector-plane distortion*, and *depth-of-field aberration*.

**Wavelength aberration:** Wavelength aberration and detector-plane distortion are tied to the  $\lambda R_d$  scaling factor in Eqs. (119) and (120) that relates position  $(x_d, y_d)$  in the detector plane to spatial frequencies  $(f_x, f_y)$  in Fourier space. Any variation of this scaling factor during the process of sampling Fourier space causes image degradation. Wavelength aberration is image degradation caused by varying  $\lambda$  during a measurement to achieve range resolution. This variation is minimal for the short frequency scans used for low-range-resolution measurements but becomes a problem as the range resolution increases. In terms of the measured speckle pattern, wavelength aberration manifests itself as a wavelength-dependent speckle size. As  $\lambda$  increases, the entire speckle pattern expands about the  $z$ -axis. This expansion causes speckle lobes to shift outward with a rate proportional to the radial distance  $r$  from the origin of the observation plane.

To investigate the effect of wavelength aberration on 3D images, consider its effect on a single scattering point located at  $(x_h, y_h, z_h)$ . Through Eq. (117), the phase error in the Fourier kernel introduced by wavelength aberration can be written as

$$\Delta\phi = 2\pi \frac{\Delta\nu}{c} \frac{x_h x_d + y_h y_d}{R_d} \quad (129)$$

This phase error varies during a measurement according to the values of the parameters  $x_d$ ,  $y_d$ , and  $\Delta\nu$  used to sample Fourier space. The maximum extent of this variation is obtained by setting  $x_d = w_x$ ,  $y_d = w_y$ , and  $\Delta\nu = B$  and taking the absolute value of the coordinates of the scattering point. Relating  $w_x$ ,  $w_y$ , and  $B$  to the resolutions  $\Delta x$ ,  $\Delta y$ , and  $\Delta z$  through Eqs. (122)–(124) and requiring that the variation of the phase error be less than  $\pi/2$  results in the following condition for insignificant wavelength-aberration effects:

$$\frac{|x_h|}{\Delta x} + \frac{|y_h|}{\Delta y} < \frac{\Delta z}{2\lambda_0} \quad (130)$$

As a representative case, we take a point along the  $x$ -axis and set  $y_h = 0$  to obtain

$$|x_h| < \frac{\Delta x \Delta z}{2\lambda_0} \quad (131)$$

Thus, for a range resolution of  $\Delta z = 100 \mu\text{m}$  and a wavelength of  $\lambda_0 = 0.8 \mu\text{m}$ , there can be only  $|x_h|/\Delta x = 62.5$  resolution cells between the scattering point and the reference point before wavelength-aberration effects begin to become significant.

Now, let us investigate the effect of wavelength aberration by considering the 2D image formed by Fourier transforming a single speckle frame. If a speckle frame is acquired at the mean frequency  $\nu_0 = c/\lambda_0$ , then the scaling factor that places this image point at the correct position  $(x_h, y_h)$  in the transverse plane is  $\lambda_0 R_d$ . The application of this same scaling factor to frames at a different wavelength  $\lambda$ , however, produces the erroneous image position  $(x_h \lambda_0/\lambda, y_h \lambda_0/\lambda)$ , which is written in terms of the frequency offset  $\Delta\nu$  as  $[x_h(1 + \Delta\nu/\nu_0), y_h(1 + \Delta\nu/\nu_0)]$ . Thus, scanning the laser frequency causes the 2D image point to move along a radial line in the transverse plane, and the total blur widths in the  $x$  and  $y$  directions for a frequency scan of bandwidth  $B$  are

$$x_{\text{blur}} = x_h \frac{B}{\nu_0} = x_h \frac{\lambda_0}{2\Delta z} \quad (132)$$

and

$$y_{\text{blur}} = y_h \frac{B}{\nu_0} = y_h \frac{\lambda_0}{2\Delta z} \quad (133)$$

The total length of the radial blur line caused by wavelength aberration is given by

$$r_{\text{blur}} = r_h \frac{B}{\nu_0} = r_h \frac{\lambda_0}{2\Delta z} \quad (134)$$

where  $r_h = (x_h^2 + y_h^2)^{1/2}$  is the transverse distance between the scattering point and the reference point. The full 3D image has the same transverse structure.

Equations (132)–(134) show that the size of the blur caused by wavelength aberration is proportional to the transverse distance of the scattering point from the reference point. Therefore, the location of the reference point in the transverse plane plays an important role in determining the severity of wavelength-aberration effects and the optimal location for the reference point is near the center of the object. A comparison of Eqs. (131) and (132) shows that the blur size corresponding to the condition for insignificant wavelength aberration is  $x_{\text{blur}} = \Delta x/4$

The second forms of Eqs. (132)–(134) explicitly show an inverse relation between the range resolution  $\Delta z$  and the degradation in cross-range resolution caused by wavelength aberration. These results indicate that it is necessary to correct for wavelength aberration to simultaneously achieve high range resolution and high cross-range resolution for an object with large cross-range extent.

There are two general techniques for achieving wavelength-aberration compensation: digital compensation of speckle-size changes and optical compensation by varying the size of the speckle pattern at the detector plane. The second technique can be implemented by using a lens to adjust the speckle size, as described in Section 5, or by varying the distance to the detector plane such that  $R_d \lambda$  is fixed. For example, a range resolution of  $\Delta z = 100 \mu\text{m}$  at  $\lambda_0 = 0.8 \mu\text{m}$  corresponds to a change in wavelength of 0.4% of the nominal wavelength. Thus, wavelength-aberration correction could be accomplished by changing the distance  $R_d$  from the reference point to the detector plane by 0.4% during the frequency scan.

**Detector-plane distortion:** Detector-plane distortion is also governed by Eqs. (119) and (120). This aberration corresponds to a nonconstant value of  $R_d$ , typically as a result of sampling on a flat detector plane with constant  $z_d$  value rather than on the interior surface of a sphere of radius  $R_d$ . Another way of describing this difference is that the radial position  $r_d$  of pixels goes as  $\tan \theta_d = r_d/z_d$  for flat detector arrays, rather than as  $\sin \theta_d = r_d/R_d$ , as required by Eqs. (119) and (120).

Detector-plane distortion is insignificant for measurements with low cross-range resolution because the maximum value of  $\theta_d$  is so small that the difference between  $\sin \theta_d$  and  $\tan \theta_d$  is negligible. One can determine when detector-plane distortion begins to become a problem by looking at the phase error it introduces in the interference pattern from the reference point and a scatterer at location  $(x_h, y_h, z_h)$ . If wavelength aberration has been corrected, the phase error caused by detector-plane distortion is

$$\Delta\phi = \frac{2\pi}{\lambda_0} (x_h x_d + y_h y_d) \left( \frac{1}{\sqrt{x_d^2 + y_d^2 + z_d^2}} - \frac{1}{z_d} \right) \quad (135)$$

The maximum variation of the phase error is determined by calculating  $\Delta\phi$  at detector coordinates of  $(-w_x/2, -w_y/2)$  and  $(w_x/2, w_y/2)$  and taking the difference. The following condition for negligible detector-plane distortion is obtained by converting to resolutions  $\Delta x$  and  $\Delta y$  through Eqs. (122) and (123), allowing a maximum phase variation of  $\pi/2$ , expanding the result in a series for small  $\lambda_0/\Delta x$  and  $\lambda_0/\Delta y$ , and keeping lowest order terms:

$$\frac{|x_h|}{\Delta x} + \frac{|y_h|}{\Delta y} < \frac{2}{\lambda_0^2} \left( \frac{1}{\Delta x^2} + \frac{1}{\Delta y^2} \right)^{-1} \quad (136)$$

As a representative case, assume the scattering point lies on the  $x$ -axis and that  $\Delta x = \Delta y$ , yielding

$$|x_h| < \frac{\Delta x^3}{\lambda_0^2} \approx \frac{\lambda_0}{8 \sin^3 \theta_d} \quad (137)$$

Equation (137) indicates that the effects of detector-plane distortion are more pronounced for object points that are farther away from the reference point and that these effects are negligible unless high resolution is required over large fields of view. For example, with  $\lambda_0 = 0.8 \mu\text{m}$  and  $\Delta x = 40 \mu\text{m}$ , a field of view of  $x_h = 100 \text{ mm}$  is achievable without deleterious effects from detector-plane distortion. The number of resolution cells possible without distortion is given by the ratio  $|x_h|/\Delta x = 2500$ , which is as high as the number of pixels per side likely in a detector array. Consequently, detector-plane distortion is not a problem for this situation. Detector-plane distortion becomes a problem, however, for microscopic applications with high cross-range resolutions. For example, with  $\Delta x = 4 \mu\text{m}$ , the maximum field of view without distortion effects is  $|x_h| = 100 \mu\text{m}$  and the ratio  $|x_h|/\Delta x$  is 25, which severely limits the number of resolution cells in the transverse direction.

Correction of detector-plane distortion can be accomplished digitally, optically, or through the use of specialized detector arrays. A well-designed 3D imaging system would simultaneously correct for wavelength aberration and detector-plane distortion. In many practical situations, a Fourier-transform lens could be used to simulate far-field detection. This approach provides the opportunity to correct for detector-plane distortion in the design of the Fourier-transform lens and to address wavelength aberration. One approach is to design a zoom Fourier-transform lens with variable focal length  $f$  that is varied during the frequency scan such that  $\lambda f$  is constant. Another approach is to design a Fourier-transform lens that is achromatic in the sense that  $\lambda f$  is constant [57-58].

In designing a Fourier-transform lens, the object is assumed to be at infinity and the entrance pupil is at the scattering object. Parallel rays passing through the entrance pupil at an angle  $\theta_d$  must produce a sharp focus at a point of height  $f \sin \theta_d$  on the detector plane. There is no requirement that the object be placed at the front-focal plane for this application because phase errors due to curvature do not affect the measured intensity.

Depth-of-field aberration: This aberration results from sampling Fourier space on the surface of the Ewald sphere rather than on straight parallel planes. Depth-of-field aberration is embodied in the second term in Eq. (118). This term, written as

$$\Delta v_{\text{offset}} = -\frac{c}{2} \left( \frac{f_x^2 + f_y^2}{f_{z_0} + \Delta f_z} \right) \quad (138)$$

gives the frequency offset value  $\Delta v_{\text{offset}}$  that is necessary at the given values of  $f_x, f_y$ , and  $\Delta f_z$  to sample 3D Fourier space on a plane rather than on the surface of the Ewald sphere. The result of depth-of-field aberration is to degrade image points having large range offsets  $z_h$  from the reference point; hence, the

term depth-of-field aberration. The first step in calculating the maximum range offset that can be achieved without degradation from this aberration is to write an expression similar to Eqs. (129) and (135) for the phase error that this aberration causes in  $I_3$  for a scattering point at  $(x_h, y_h, z_h)$ :

$$\Delta\phi = 2\pi \frac{z_h}{\lambda_0} \left(1 - \frac{z_d}{R_d}\right) = 2\pi \frac{z_h}{\lambda_0} \left(1 - \sqrt{1 - \frac{x_d^2 + y_d^2}{R_d^2}}\right) \quad (139)$$

The maximum phase error occurs at  $x_d = w_x/2$  and  $y_d = w_y/2$ . By requiring this phase error to be less than  $\pi/2$ , writing  $w_x$  and  $w_y$  in terms of the transverse resolutions  $\Delta x$  and  $\Delta y$ , expanding the result in a series for small  $\lambda_0/\Delta x$  and  $\lambda_0/\Delta y$ , and keeping the lowest order terms,

$$|z_h| < \frac{2}{\lambda_0} \left( \frac{1}{\Delta x^2} + \frac{1}{\Delta y^2} \right)^{-1} \quad (140)$$

is obtained. A simplified expression is obtained by setting  $\Delta x = \Delta y$ :

$$|z_h| < \frac{\Delta x^2}{\lambda_0} \approx \frac{\lambda_0}{4 \sin^2 \theta_d} \quad (141)$$

Note the similarity between Eq. (141) and Eq. (137). Because Eq. (141) goes as  $\sin^{-2} \theta_d$  rather than  $\sin^{-3} \theta_d$ , depth-of-field aberration is more sensitive to the value of the cross-range resolution than is detector-plane distortion.

Depth-of-field aberration is a result of the fact that the region of Fourier space sampled by a single speckle frame lies on a curved surface—the Ewald sphere of reflection—in Fourier space. For a small enough range of spatial frequencies  $f_x$  and  $f_y$ , the sampled region approximates a plane and depth-of-field aberration is negligible. The range of spatial frequencies over which this planar approximation is valid is determined by how rapidly the 3D Fourier transform fluctuates in the  $f_z$  direction. Because this fluctuation is slower for objects with smaller range extents, the planar approximation is valid over larger ranges of  $f_x$  and  $f_y$  (and hence smaller values of  $\Delta x$  and  $\Delta y$ ) for these objects. This behavior is summarized by the condition for negligible depth-of-field aberration in Eq. (141).

Equation (141) places stringent requirements on the maximum range extent allowable without degradation from depth-of-field aberration. For example, with  $\lambda_0 = 0.8 \mu\text{m}$ , a cross-range resolution of  $\Delta x = 4 \mu\text{m}$  yields a maximum range extent of  $|z_h| = 20 \mu\text{m}$ . With  $\Delta x = 40 \mu\text{m}$ , the maximum range extent increases to  $|z_h| = 2 \text{mm}$ . By relaxing the cross-range resolution to  $\Delta r = 400 \mu\text{m}$ , a range extent of  $|z_h| = 200 \text{mm}$  is achievable without depth-of-field aberration compensation. This depth-of-field behavior is no different than that from conventional imaging, where the lateral resolution determines the depth of field, or from raster scanning with a laser spot, where a tight laser focus at one plane implies a large spread in the spot size at other planes. An advantage of forming 3D images by speckle-pattern-sampling is that this aberration can be corrected in the data processing to yield high-resolution images over large volumes in image space.

Equation (138) provides the key for correcting depth-of-focus aberration. The compensation technique builds up the information required for each flat plane in Fourier space from previous speckle

frames. The correct frequency offset value for each pixel is calculated by Eq. (138) and the corresponding frame-offset number is determined. An interpolation filter is used because previous frames will generally not provide the exact frequency offset that is required for each pixel. [If the total  $f_z$  sampling range is a small fraction of the nominal spatial frequency  $f_{z_0}$ , then the  $\Delta f_z$  dependence in Eq. (138) can be dropped and the frequency offset for a given  $(f_x, f_y)$  will remain constant over the entire frequency scan.] As lateral resolution improves, sampling over larger ranges of  $f_x$  and  $f_y$  is required, and the frequency-offset value increases, making the compensation technique more difficult to implement. This technique, however, greatly improves image quality for images having range extents beyond the aberration-free limits.

**Near-Field Effects.** In developing the basic principles of 3D imaging, the observation point  $P_d$  and the source point  $P_s$  have been assumed to be located in the far field of the scattering object. Consequently, only the first two terms have been kept in the approximation for  $R_{hd}$  given by Eq. (99) and the corresponding expression for  $R_{sh}$ . Because of the rather large distances required for the validity of the far-field approximation, near-field effects will now be investigated by retaining all four terms in the wide-angle Fresnel approximation. The resulting form for  $I_3$  corresponding to Eq. (109) is

$$\begin{aligned}
 I_3 = & g_r^* \int_{-\infty}^{\infty} \int_{-\infty}^{\infty} g(x_h, y_h, z_h) \\
 & \times \exp \left\{ i \frac{\pi}{\lambda} \left[ \frac{(l_s x_h + m_s y_h + n_s z_h)^2}{R_s} + \frac{(l_d x_h + m_d y_h + n_d z_h)^2}{R_d} - (x_h^2 + y_h^2 + z_h^2) \left( \frac{1}{R_s} + \frac{1}{R_d} \right) \right] \right\} \\
 & \times \exp \left\{ i \frac{2\pi}{\lambda} [x_h(l_s + l_d) + y_h(m_s + m_d) + z_h(n_s + n_d)] \right\} dx_h dy_h dz_h
 \end{aligned} \quad (142)$$

The integral in Eq. (142) is the 3D Fourier transform of the product of the complex scattering function  $g(x, y, z)$  and a complex exponential that incorporates near-field effects. As  $R_s$  and  $R_d$  increase, the points  $P_s$  and  $P_d$  move into the far field and the complex exponential approaches unity, leaving a straight Fourier transform as given by Eq. (109).

An alternative form of Eq. (142), expressed in terms of  $\tilde{g}(f_x, f_y, f_z)$ , is obtained by calculating the Fourier transform of the complex exponential factor and applying the convolution theorem:

$$\begin{aligned}
 I_3 = & g_r^* \int_{-\infty}^{\infty} \int_{-\infty}^{\infty} \int_{-\infty}^{\infty} \tilde{g} \left( \frac{l_s + l_d}{\lambda} - f'_x, \frac{m_s + m_d}{\lambda} - f'_y, \frac{n_s + n_d}{\lambda} - f'_z \right) \\
 & \times H(f'_x, f'_y, f'_z; l_s, m_s, R_s; l_d, m_d, R_d; \lambda) df'_x df'_y df'_z
 \end{aligned} \quad (143)$$

where

$$\begin{aligned}
H(f'_x, f'_y, f'_z; l_s, m_s, R_s; l_d, m_d, R_d; \lambda) &= -\frac{1+i}{\sqrt{2}} \frac{R_s R_d}{\sqrt{R_s + R_d}} \frac{\lambda^{3/2}}{\sqrt{1 - (\hat{\mathbf{R}}_s \cdot \hat{\mathbf{R}}_d)^2}} \\
&\times \exp \left\{ i\pi \frac{\lambda}{1 - (\hat{\mathbf{R}}_s \cdot \hat{\mathbf{R}}_d)^2} \left[ R_s (f'_x l_d + f'_y m_d + f'_z n_d)^2 + R_d (f'_x l_s + f'_y m_s + f'_z n_s)^2 \right. \right. \\
&\left. \left. + \frac{[f'_x (m_s n_d - m_d n_s) + f'_y (l_d n_s - l_s n_d) + f'_z (l_s m_d - l_d m_s)]^2}{1/R_s + 1/R_d} \right] \right\} \quad (144)
\end{aligned}$$

and  $\hat{\mathbf{R}}_s$  and  $\hat{\mathbf{R}}_d$  are unit vectors. In the limit as  $R_s$  and  $R_d$  approach infinity,  $H$  becomes a 3D  $\delta$ -function located at the origin of Fourier space and Eq. (143) reduces to Eq. (109).  $H$  can be interpreted as an impulse-response function in Fourier-space that varies with the wavelength  $\lambda$  and the positions of the source point  $P_s$  and the observation point  $P_d$ .

Equations (142)–(144) are general expressions valid for arbitrary source-point directions. If it is assumed that the source point lies on the positive  $z$ -axis so that  $l_s = m_s = 0$  and  $n_s = 1$ , as in the far-field analysis, then Eq. (142) reduces to

$$\begin{aligned}
I_3 &= g_r^* \int \int \int_{-\infty}^{\infty} g(x_h, y_h, z_h) \exp \left\{ i\pi \left[ -\frac{x_h^2 + y_h^2}{\lambda R_s} + \frac{(l_d x_h + m_d y_h + n_d z_h)^2 - x_h^2 - y_h^2 - z_h^2}{\lambda R_d} \right] \right\} \\
&\times \exp \left\{ i \frac{2\pi}{\lambda} [x_h l_d + y_h m_d + n_h (1 + n_d)] \right\} dx_h dy_h dz_h \quad (145)
\end{aligned}$$

and Eq. (144) becomes

$$\begin{aligned}
H(f'_x, f'_y, f'_z; l_s = 0, m_s = 0, R_s; l_d, m_d, R_d; \lambda) &= -\frac{1+i}{\sqrt{2}} \frac{R_s R_d}{\sqrt{R_s + R_d}} \frac{\lambda^{3/2}}{\sqrt{l_d^2 + m_d^2}} \\
&\times \exp \left\{ i\pi \frac{\lambda}{l_d^2 + m_d^2} \left[ R_s (f'_x l_d + f'_y m_d + f'_z n_d)^2 + R_d f_z'^2 + \frac{(f'_x m_d - f'_y l_d)^2}{1/R_s + 1/R_d} \right] \right\} \quad (146)
\end{aligned}$$

Either Eq. (145) or Eq. (146) can serve as the basis for studying near-field effects in 3D imaging. Both forms are listed for reference; the following analysis, however, is based solely on Eq. (145).

Before proceeding with the analysis of Eq. (145), it should be observed that the complex exponential containing the near-field effects in Eq. (145) is neatly separated into an  $R_d$ -dependent term and an  $R_s$ -dependent term. Therefore, it can be inferred that the  $R_s$ -dependent term contains near-field effects caused by noncollimated illumination of the scattering object by the source point and that the  $R_d$ -dependent term contains near-field effects caused by the fact that the scattered light reaching the

observation point is noncollimated. These two effects may be treated separately or in combination by independently choosing whether the observation point and the source point satisfy the far-field condition.

To find the image  $P(x, y, z)$  corresponding to Eq. (145), it is necessary to evaluate the inverse-Fourier transform given by Eq. (114). Doing so, however, requires that  $I_3$  be expressed as a function of the spatial-frequency variables  $f_x, f_y$ , and  $f_z$ . It will be advantageous to rearrange the argument of the complex exponential in Eq. (145) as

$$\begin{aligned} & -\frac{x_h^2+y_h^2}{\lambda R_s} + \frac{(l_d x_h + m_d y_h + n_d z_h)^2 - x_h^2 - y_h^2 - z_h^2}{\lambda R_d} \\ & = 2\sqrt{1-l_d^2-m_d^2} \frac{l_d x_h + m_d y_h}{\lambda R_d} z_h - \frac{x_h^2+y_h^2}{\lambda} \left( \frac{1}{R_s} + \frac{1}{R_d} \right) + \frac{(x_h l_d + y_h m_d)^2 - z_h^2 (l_d^2 + m_d^2)}{\lambda R_d} \end{aligned} \quad (147)$$

Then, by using Eqs. (105) and (106) to convert  $l_d$  and  $m_d$  to spatial frequencies  $f_x$  and  $f_y$ , Eq. (145) can be written as

$$\begin{aligned} I_3 &= g_r^* \int_{-\infty}^{\infty} \int_{-\infty}^{\infty} g(x_h, y_h, z_h) \exp \left\{ i\pi \frac{\lambda}{R_d} \left[ (f_x x_h + f_y y_h)^2 - (f_x^2 + f_y^2) z_h^2 \right] \right\} \\ & \times \exp \left[ -i2\pi (f_x x_h + f_y y_h) \left( 1 - \frac{z_h}{R_d} \sqrt{1 - \lambda^2 f_x^2 - \lambda^2 f_y^2} \right) \right] \\ & \times \exp \left\{ -i2\pi \left[ f_z z_h + \frac{x_h^2 + y_h^2}{2\lambda} \left( \frac{1}{R_s} + \frac{1}{R_d} \right) \right] \right\} dx_h dy_h dz_h \end{aligned} \quad (148)$$

Finally, the  $\lambda$  dependence can be eliminated from Eq. (148) through the use of Eq. (116):

$$\begin{aligned} I_3 &= g_r^* \int_{-\infty}^{\infty} \int_{-\infty}^{\infty} g(x_h, y_h, z_h) \exp \left\{ -i2\pi \frac{f_z}{R_d} \left[ \frac{(f_x x_h + f_y y_h)^2 - (f_x^2 + f_y^2) z_h^2}{f_x^2 + f_y^2 + f_z^2} \right] \right\} \\ & \times \exp \left[ -i2\pi (f_x x_h + f_y y_h) \left( 1 - \frac{-f_x^2 - f_y^2 + f_z^2}{f_x^2 + f_y^2 + f_z^2} \frac{z_h}{R_d} \right) \right] \\ & \times \exp \left\{ -i2\pi \left[ f_z z_h - \frac{x_h^2 + y_h^2}{4} \left( f_z + \frac{f_x^2 + f_y^2}{f_z} \right) \left( \frac{1}{R_s} + \frac{1}{R_d} \right) \right] \right\} dx_h dy_h dz_h \end{aligned} \quad (149)$$

Note that  $R_s$  and  $R_d$  are free parameters in Eq. (149) that can be varied independently of  $f_x, f_y$ , and  $f_z$ . Therefore, there is a choice as to how these parameters behave during a measurement. In practical terms, one must consider both the detector geometry and any motion of the detector as a whole (or motion of individual elements of the detector) during a frequency scan. One may also allow the source point to move along the  $z$ -axis during a frequency scan.

Let us first consider detector geometry. The two most obvious choices are to hold either  $R_d$  constant or  $z_d$  constant during the measurement so that the speckle pattern is sampled on the interior surface of a sphere or on a planar surface, respectively. Equation (149) is suitable for sampling on the surface of a sphere as it stands. To apply it to a flat detector array,  $R_d$  is expressed in terms of detector plane distance  $z_d$  and spatial-frequency variables as

$$R_d = \frac{z_d}{n_d} = \frac{z_d}{\sqrt{1-l_d^2-m_d^2}} = z_d \frac{f_x^2 + f_y^2 + f_z^2}{-f_x^2 - f_y^2 + f_z^2} \quad (150)$$

There are also two natural choices for the variation of  $R_s$  and  $R_d$ . One is to keep these quantities fixed; the other is to hold the products  $R_s\lambda$  and  $R_d\lambda$  constant during the measurement. It will be shown that there may be an advantage to the latter choice in some situations.

Now that  $I_3$  is expressed as a function of spatial frequency, we can perform an inverse Fourier transform of Eq. (149) to obtain the image  $P(x, y, z)$  and observe any aberrations that appear in this image. Equation (149) is quite a general result for 3D imaging because no additional assumptions have been made beyond placing the source point on the  $z$ -axis and using the wide-angle Fresnel approximation. Evaluation of the inverse Fourier transform of Eq. (149) is complicated by the fact that nonlinearities in spatial frequency appear in the arguments of the complex exponentials. If not for these nonlinear terms, the inverse Fourier transform could be evaluated immediately.

An understanding of the dominant near-field effects can be gained by linearizing the spatial-frequency dependence in Eq. (149) so that it becomes a paraxial expression. This equation has already been organized in a manner that highlights the linear terms; the significance of the grouping of the three complex-exponential factors in Eq. (149) is that, to lowest order in  $f_x, f_y$  and  $\Delta f_z$ , the second factor is linear in  $f_x$  and  $f_y$  and the third factor is linear in  $\Delta f_z$ ; the first factor contains higher-order dependence and additional cross terms. The linearized form of Eq. (149) is

$$I_3 = g_r^* \int_{-\infty}^{\infty} \int_{-\infty}^{\infty} \int_{-\infty}^{\infty} g(x_h, y_h, z_h) \exp \left[ -i2\pi \left( f_x x_h + f_y y_h \right) \left( 1 - \frac{z_h}{z_d} \right) \right] \\ \times \exp \left\{ -i2\pi f_z \left[ z_h - \frac{x_h^2 + y_h^2}{4} \left( \frac{1}{z_s} + \frac{1}{z_d} \right) \right] \right\} dx_h dy_h dz_h \quad (151)$$

Equation (151) is written for constant  $z_d$  because  $z_d$  and  $R_d$  are equivalent to first order and constant- $z_d$  measurements are more likely in practice. Also,  $R_s$  and  $z_s$  have been interchanged because they are equal by the assumption that the source point lies on the  $z$ -axis.

Before evaluating the image corresponding to Eq. (151), validity conditions for Eq. (151) are calculated by determining the maximum object-point offset from the reference point that is allowed. This is done by requiring the phase error caused by nonlinear terms to be less than  $f_x = 1/(2\Delta x)$  for maximum spatial-frequency values of  $f_x = 1/(2\Delta x)$  and  $f_y = 1/(2\Delta y)$ . For a practical frequency scan,  $\Delta f_z$  is a fraction of  $f_{z_0}$  so that  $\Delta f_z$  can be set to zero. The resulting conditions imposed by the source-point distance  $z_s$  and the observation distance  $z_d$  obtained by setting  $\Delta x = \Delta y$  and  $y_h = 0$  are

$$|x_h| < \Delta x \sqrt{\frac{2z_s}{\lambda_0}}, \quad (152)$$

$$|x_h| < \Delta x \sqrt{\frac{2z_d}{\lambda_0}}, \quad (153)$$

and

$$|z_h| < \Delta x \sqrt{\frac{z_d}{\lambda_0}}. \quad (154)$$

An attractive feature of Eqs. (152) and (153) is that  $|x_h|$  is proportional to  $\Delta x$ . Because the number of pixels in a given direction in the detector array determines the maximum number of transverse points  $|x_h|/\Delta x$  that can be resolved in that direction in the image, it is not necessary to have a value of  $|x_h|/\Delta x$  from Eqs. (152) and (153) that is larger than the number of pixels along an edge of the detector array. For example, even a small source-point distance of  $z_s = 100$  mm and observation distance of  $z_d = 100$  mm yields a  $|x_h|/\Delta x$  ratio of 500 and a  $|z_h|/\Delta x$  ratio of 350 for  $\lambda_0 = 0.8 \mu\text{m}$ . Thus Eqs. (152)–(154) place relatively minor restrictions on practical imaging systems.

Now that it has been shown that aberrations caused by the nonlinear terms can be neglected for many practical applications, Eq. (151) can be substituted into Eq. (114) to evaluate the image  $P(x, y, z)$ . In doing so, it is assumed that the values of  $z_s$  and  $z_d$  remain constant throughout the measurement. The resulting image is

$$P(x, y, z) = g_r^* \int_{-\infty}^{\infty} \int_{-\infty}^{\infty} g(x_h, y_h, z_h) \delta \left[ x - x_h \left( 1 + \frac{z_h}{z_d} \right) \right] \delta \left[ y - y_h \left( 1 + \frac{z_h}{z_d} \right) \right] \delta \left[ z - z_h + \frac{x_h^2 + y_h^2}{4} \left( \frac{1}{z_s} + \frac{1}{z_d} \right) \right] dx_h dy_h dz_h \quad (155)$$

For far-field observation with collimated illumination, Eq. (155) reduces to the original result given in Eq. (115).

For far-field observation with noncollimated illumination, Eq. (155) becomes

$$P(x, y, z) = g_r^* g \left( x, y, z + \frac{x^2 + y^2}{4z_s} \right) = g_r^* a(x, y) \delta \left[ z - h(x, y) + \frac{x^2 + y^2}{4z_s} \right] \quad (156)$$

The second form of Eq. (156) is obtained by relating  $g(x, y, z)$  to  $a(x, y)$  and  $h(x, y)$  through Eq. (90). From this form it is clear that the effect of noncollimated illumination of the scattering object and far-field observation is to distort the surface of the image. This distortion is caused by the curvature of the outgoing beam, which produces different pathlengths to different points on the  $z = 0$  plane. These pathlength differences introduce  $z$  shifts in the image that increase with the distance in  $x$  and  $y$  from the origin. The quadratic dependence in Eq. (156) is due to the Fresnel approximation of a spherical wave of

radius  $R_s$ . There is a factor of 4 rather than 2 in the denominator because the pathlength difference corresponding to the height function  $h(x, y)$  is doubled, being a round-trip measurement. Correction of image distortion due to noncollimated illumination and far-field observation is a straightforward process that can be accomplished digitally. Because there is no coupling between the  $x$ ,  $y$ , and  $z$  coordinates, the correction consists of simply adding a value to  $h(x, y)$  that is a function of position  $(x, y)$  and source distance  $z_s$ .

The difficulty with evaluating Eq. (155) for near-field observation is that there is a coupling of  $x_h$ ,  $y_h$ , and  $z_h$  in the  $\delta$ -functions. The conditions that  $R_h \ll z_d$  and  $R_h \ll z_s$ , however, can be used to uncouple these  $\delta$ -functions and to approximate Eq. (155) as

$$P(x, y, z) = g_r^* \int_{-\infty}^{\infty} \int_{-\infty}^{\infty} g(x', y', z') \times \delta(x' - x + x_{\text{shift}}) \delta(y' - y + y_{\text{shift}}) \delta(z' - z + z_{\text{shift}}) dx' dy' dz' \quad (157)$$

where

$$x_{\text{shift}} = x \left[ \frac{z}{z_d} + \frac{x^2 + y^2}{4z_d} \left( \frac{1}{z_s} + \frac{1}{z_d} \right) \right] \quad (158)$$

$$y_{\text{shift}} = y \left[ \frac{z}{z_d} + \frac{x^2 + y^2}{4z_d} \left( \frac{1}{z_s} + \frac{1}{z_d} \right) \right] \quad (159)$$

and

$$z_{\text{shift}} = -\frac{x^2 + y^2}{4z_d} \left( \frac{1}{z_s} + \frac{1}{z_d} \right) \quad (160)$$

Then the general result corresponding to Eq. (156) that encompasses both noncollimated illumination and near-field observation is

$$P(x, y, z) = g_r^* g(x - x_{\text{shift}}, y - y_{\text{shift}}, z - z_{\text{shift}}) = g_r^* a(x - x_{\text{shift}}, y - y_{\text{shift}}) \delta[z - z_{\text{shift}} - h(x - x_{\text{shift}}, y - y_{\text{shift}})] \quad (161)$$

Equation (161) is an important result stating that the dominant near-field effect for constant values of  $z_s$  and  $z_d$  is a distortion in the 3D image. Because this distortion can be removed computationally, high-quality 3D images can be achieved much further into the near field than the far-field condition given by Eq. (101) would lead one to believe.

Next, let us explore the option of varying  $z_s$  and  $z_d$  during a measurement. First, consider moving the source point along the  $z$ -axis such that the product  $\lambda z_s$  remains fixed. Inspection of the second complex-exponential factor in Eq. (151) shows that keeping  $\lambda z_s$  fixed will eliminate phase variations due to wavelength changes in the quadratic curvature term in this complex exponential. Therefore, this

component is only dependent on  $x_h$  and  $y_h$  and can be absorbed into the  $a(x_h, y_h)$  factor without distorting the surface profile  $h(x_h, y_h)$ . Thus, keeping  $\lambda z_s$  fixed is an optical means of correcting for the curvature due to noncollimated illumination. Likewise, fixing  $\lambda z_d$  eliminates the distortion caused by near-field observation; it also, however, introduces a phase error by causing  $z_h/z_d$  in the first complex exponential in Eq. (151) to vary during a frequency scan, but this phase error is negligible, provided the conditions in Eqs. (153) and (154) are satisfied. The resulting image obtained by fixing  $\lambda z_s$  and  $\lambda z_d$  is

$$\begin{aligned}
 P(x, y, z) &= g_r^* g \left( x - \frac{xz}{z_d}, y - \frac{yz}{z_d}, z \right) \\
 &= g_r^* a \left( x - \frac{xz}{z_d}, y - \frac{yz}{z_d} \right) \delta \left[ z - h \left( x - \frac{xz}{z_d}, y - \frac{yz}{z_d} \right) \right]
 \end{aligned} \tag{162}$$

Although nonlinearities in the distortion have been removed, the image is still distorted such that range-plane magnification varies with range. This remaining distortion can readily be corrected in the data processing. An additional advantage of keeping  $\lambda z_d$  fixed is that wavelength-aberration compensation occurs automatically. Equation (162) is the basis for an optically simple 3D microscope that requires no lenses.

In summary, it has been shown that the original far-field theory for 3D imaging based on Eq. (109) can be extended well into the near field. The dominant near-field effect for most practical situations is image distortion, which can be corrected to produce accurate high-resolution images. An important benefit of near-field imaging is that noncollimated illumination and near-field observation can be used for larger objects where it is more difficult or more expensive to produce a collimating optic large enough to illuminate the object and to form its far-field speckle pattern at the detector plane without vignetting effects.

**Measurements.** The speckle-pattern-sampling technique for 3D imaging is now illustrated with laboratory measurements obtained using the optical system in Figure 19. The advantage of this system is that it produces collimated illumination and simulates far-field observation so that near-field effects are entirely eliminated for objects up to 225 mm in diameter.

Section 5 has already demonstrated how range information is obtained from the wavelength dependence of speckle. Figure 34 illustrates that cross-range information can also be obtained from speckle by Fourier transforming a speckle frame acquired at a single wavelength [59,60]. The object scene depicted in Figure 34(a) consists of the familiar nine-step target from Figure 27 and a specular reference point, illuminated along the axis of the step target. Three of the steps have been masked to make a more interesting object. The reference point is produced by a concave spherical mirror with a 75-mm radius of curvature located 25 mm to the right and 12.5 mm above the top right corner of the target. Figure 34(b) is the magnitude of the Fourier transform of a  $512 \times 512$  speckle frame from this object scene. The four components of Eq. (110) are evident in this figure. Because the reference point is separated from the step target in the transverse direction by more than its cross range extent of  $D_x = D_y = 19$  mm, the desired image (lower left) is isolated from the autocorrelation function (center) and the polar-symmetric image (upper right).

Let us now consider image resolution. Because of the long focal length  $R_d = f = 2$  m of the primary mirror and the small collecting area  $w_x = w_y = 16$  mm of the pinhole mirror, the cross-range resolution at  $\lambda_0 = 0.8 \mu\text{m}$  for this optical system is limited to  $\Delta x = \Delta y = 100 \mu\text{m}$  by Eqs. (122) and (123). The image in Figure 34(b) actually has a transverse resolution of  $\Delta x = \Delta y = 280 \mu\text{m}$ , which corresponds to a speckle magnification by the lens in Figure 19 of  $M = 2.4$  and a detector size of the CCD array of  $w_x = w_y = 13.8$  mm. This transverse resolution also corresponds to 68 pixels along the width of the target.

None of the three aberrations associated with errors in the sampling of Fourier space need to be corrected in Figure 34. Wavelength aberration is not an issue because the object is unresolved in range, being constructed from a single frame at constant wavelength. Detector-plane distortion can be entirely ignored for any image made with this optical system because it is negligible by Eq. (137) for even the best cross-range resolution and the largest object diameter allowed. By Eq. (141), depth-of-field aberration for the transverse resolution of  $\Delta x = \Delta y = 280 \mu\text{m}$  begins to be a problem for points that are offset from the reference point in range by more than  $|z_h| = 100$  mm. This condition is easily satisfied because the range extent of the nine-step target is only 24.6 mm.

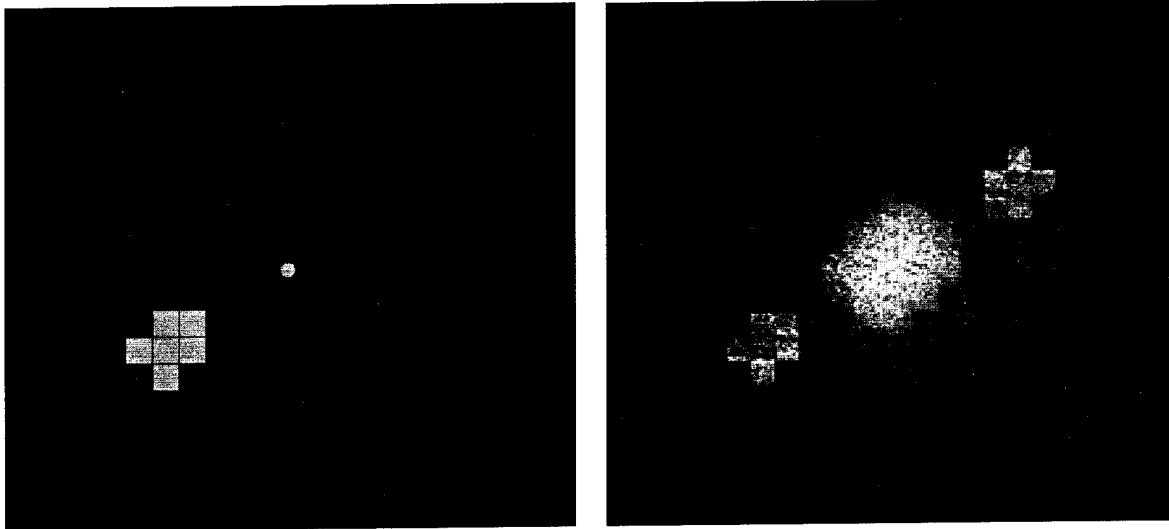
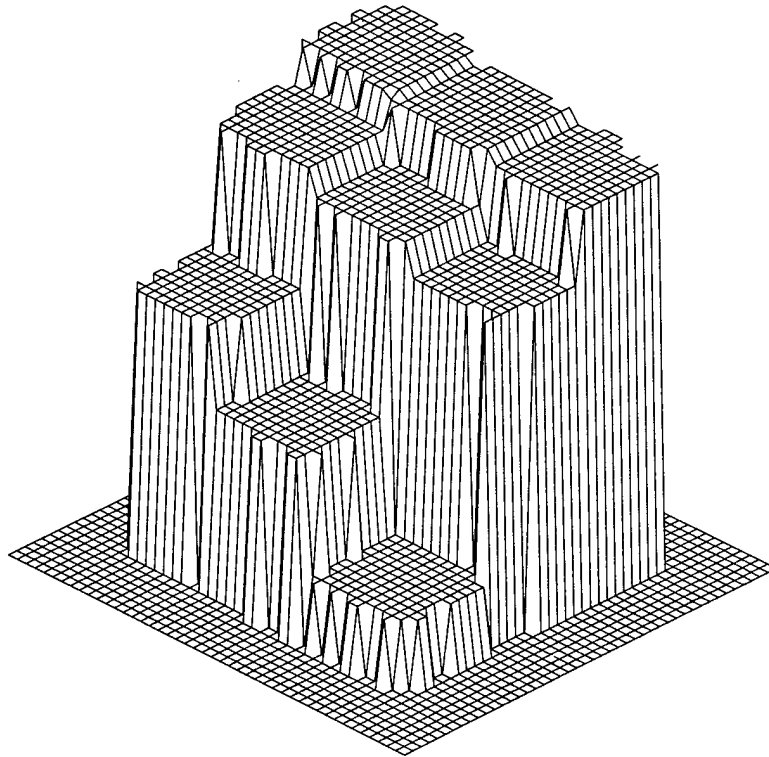


Figure 34. Cross-range-resolved image of nine-step target with three masked steps: (a) object scene consisting of target and reference point being illuminated into the page; and (b) image obtained from 2D Fourier transform of single speckle frame.

If the image in Figure 34 had been formed with the system's maximum transverse resolution of  $\Delta x = \Delta y = 100 \mu\text{m}$ , the maximum allowable range offset from the reference point would have been reduced to  $|z_h| = 12 \text{ mm}$  and the image would have been aberrated. The effect of depth-of-field aberration is to blur the 2D image of each object point by an amount that increases with the range offset  $z_h$  of that object point from the reference point. Thus, without correction of depth-of-field aberration, the only plane in perfect focus is the plane cutting through the reference point. In this regard, depth-of-field aberration is analogous with the limited depth of field encountered in conventional imaging. The higher the resolution, the more rapidly the image degrades in range.

262468-1



*Figure 35. 3D image of nine-step target obtained by speckle-pattern-sampling technique. Range resolution and cross-range resolution are obtained from the wavelength dependence and the spatial dependence of the speckle pattern, respectively.*

A comment is in order about how the value of the range offset  $z_h$  should be interpreted when implementing the reference point with a curved mirror. In the theoretical analysis, the reference point is the point from which the reference beam is scattered. Therefore, for a curved mirror, the reference point is not located at the surface of the mirror but at the focal point, either virtual or real, from which the light

appears to emanate. Consequently, for a concave spherical mirror of radius  $R$  that is illuminated with a collimated laser beam, the reference point is located in front of the mirror by the distance  $R/2$ . Because the light actually strikes the surface of the mirror, however, there is an extra propagation pathlength difference that must be accounted for in the  $z$  direction. In consideration of these facts,  $z_h$  is measured with respect to the location of the focal point and the total range extent  $L$  includes the location of the actual surface of the mirror.

Now that we have demonstrated how cross-range resolution is obtained from the speckle pattern, we demonstrate 3D imaging by combining range information (as illustrated by Figure 19) with cross range information (as illustrated by Figure 34) to produce the full 3D image of the nine-step target shown in Figure 35. For this measurement the 75-mm-radius concave mirror was placed 30 mm behind the bottom step and 10 mm to the side of the target. The desired image component can be isolated in the 3D Fourier transform because the surface of the mirror is offset in range from the target by more than its range extent. A  $256 \times 256$  region of the CCD array was selected and the speckle magnification was set at  $M = 2.5$ , yielding a transverse resolution of  $\Delta x = \Delta y = 575 \mu\text{m}$ . The total frequency span of the measurement was  $B = 320 \text{ GHz}$ , which produced a range resolution of  $\Delta z = 470 \mu\text{m}$ . For these resolutions and the given object scene, wavelength aberration and depth-of-field aberration are negligible.

By Eq. (126), the maximum frequency step size allowed for the range extent  $L = 55 \text{ mm}$  is  $\Delta v_{\text{step}} = 1.4 \text{ GHz}$ . An actual value of  $\Delta v_{\text{step}} = 1.25 \text{ GHz}$  was used in this measurement, so that the given scan bandwidth of  $B = 320 \text{ GHz}$  was achieved with a 256-frame measurement. The height values displayed in Figure 35 were obtained from the magnitude of the 3D Fourier transform by selecting the voxel having the highest value in each column. The step heights in the image agree with the step heights of the target to within the resolution of the measurement.

To demonstrate the high range resolutions that are achievable with the speckle-pattern-sampling technique, a second range-resolution target was fabricated by milling five steps of various heights in an aluminum plate. The distance between successive levels varies from  $25 \mu\text{m}$  to  $125 \mu\text{m}$  in  $25\text{-}\mu\text{m}$  increments for a target range extent of  $375 \mu\text{m}$ . The transverse dimensions of the entire target and of individual steps are  $50 \text{ mm} \times 75 \text{ mm}$  and  $15 \text{ mm} \times 50 \text{ mm}$ , respectively. Note that even the  $25\text{-}\mu\text{m}$  step is well resolved in range in the 3D image displayed in Figure 36.

The reference point in Figure 36 is a concave 75-mm-radius spherical mirror located 8 mm to the side of the middle step and recessed into the metal so that the surface of the mirror is  $395 \mu\text{m}$  below the bottom level of the target. The measurement consisted of 256 speckle frames with laser-frequency steps of  $\Delta v_{\text{step}} = 60 \text{ GHz}$  between frames, yielding a total frequency span of  $B = 15.3 \text{ THz}$  and a range resolution of  $\Delta z = 9.8 \mu\text{m}$ . The target was tilted slightly with respect to the illumination beam so that the raw image contained several discrete range steps of value  $\Delta z$  along the length of each step. The DFT technique for subdividing voxels described in Section 6.1.1 was used to enhance range resolution in Figure 36 and to eliminate range steps.

The speckle frames used in Figure 36 were taken from a  $256 \times 256$ -pixel region of the CCD array and subdivided for averaging into four  $128 \times 128$  subarrays. The height values in Figure 36 are the weighted average from these measurements. The cross-range resolution from the individual arrays is  $\Delta x = \Delta y = 700 \mu\text{m}$ .

The minimum radius of curvature that would yield a sufficient reference beam strength relative to the high return from the bare metal steps was 75 mm. Thus, the value of  $z_h$  that should be used in Eq. (141) for calculating whether depth-of-field aberration is significant is approximately half of this value,  $z_h = 37.5$  mm. Because of the large transverse resolution for this measurement, the allowable range offset  $z_h$  from Eq. (141) is many times this value so that depth-of-field aberration can be ignored for this measurement in spite of the relatively large value of  $z_h$ .

262468-2

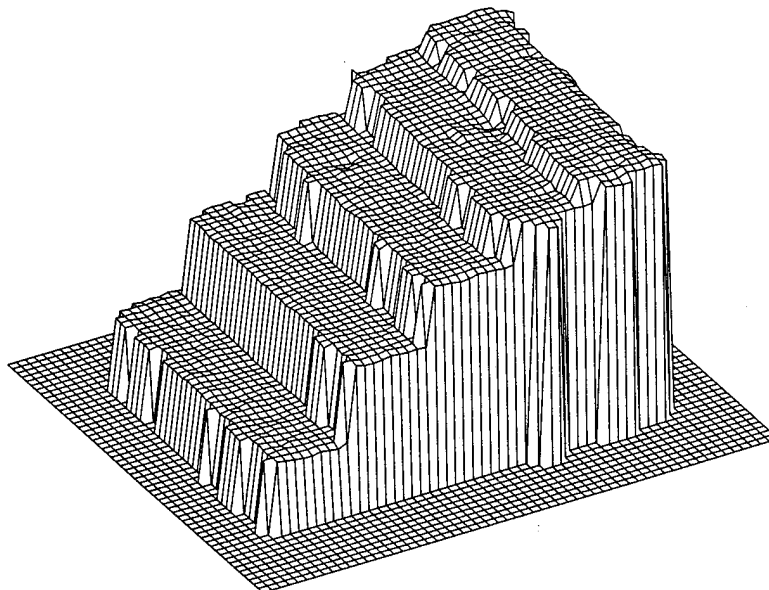


Figure 36. 3D image of five-step target demonstrating a range resolution of better than  $10 \mu\text{m}$ . The step sizes vary from  $25 \mu\text{m}$  for the top step to  $125 \mu\text{m}$  for the bottom step.

Wavelength aberration, on the other hand, is a significant aberration for this measurement; by Eq. (131), it degrades the image for object points with transverse offsets from the reference point of only 4 mm. Therefore, wavelength aberration had to be corrected in the measurement. This correction was accomplished by varying the speckle magnification during the frequency scan by changing the lens and detector positions in Figure 19 such that  $M\lambda$  remained constant.

The final measurement, Figure 37, is the 3D image of a 50-mm-long triconic being illuminated along the axis of symmetry. The streamers below the triconic represent the fact that the base of the triconic is not illuminated so that there are no scatterers to terminate the vertical lines. No aberration compensation was required here. Figure 37 is included to stress the fact that the imaging technique applies to quite general objects and that flat range steps are not required.

Many methods for 3D imaging are described in the literature and have been incorporated into practical systems [61]. In general, these methods are based on one or more of the following principles: physical contact, triangulation, time of flight, interference, or carrier modulation. The speckle-pattern sampling technique has several advantages over other techniques: It is noncontact-based and can image an entire object at once without the need for raster scanning; it can measure complex and irregular shapes having discontinuities and steep-sloped surfaces, where techniques such as Moiré interferometry run into difficulty; and its range resolution does not degrade with distance from the object, as is the case for techniques based on triangulation.

262468-1

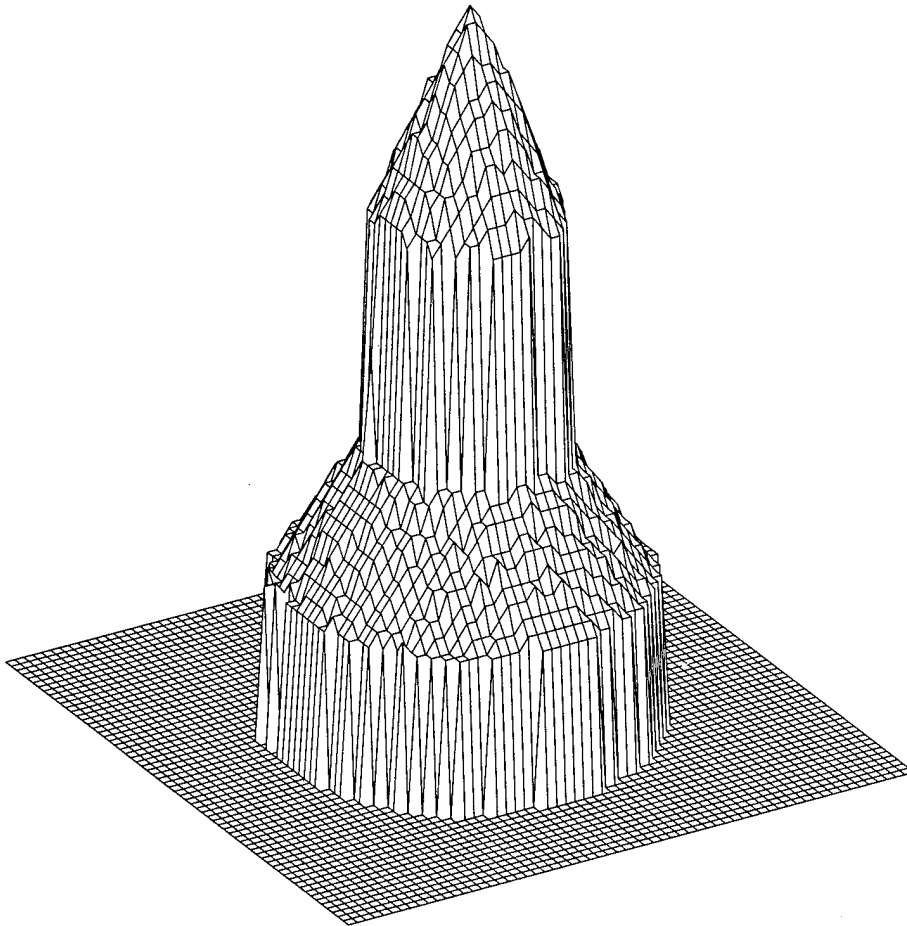


*Figure 37. 3D image of a 50-mm-long triconic obtained by the speckle-pattern-sampling technique.*

These advantages lead to many potential applications, such as inspection of turbine blades and complex gears; microscopic metrology of hardness indenters, Diesel injectors, and cutting tools; reverse engineering and digitization of clay models; large-scale metrology of airframe and autobody panels; inspection and assembly-line automation; and forensics. The three basic enabling technologies for the realization of these applications (and of applications of techniques yet to be described) are fast, rugged, compact, moderate-power, low-cost frequency-scanning lasers; high-readout-rate, megapixel, inexpensive CCD arrays; and fast, compact, low-cost, parallel-processing computers. At MIT Lincoln Laboratory, research is under way that is pushing the state of the art in each of these areas. Prototype imaging systems are now being designed and developed for specific applications ranging in size from microscopic to large scale.

### 6.1.2 Remote Orientation Sensing

An additional application of speckle-pattern sampling that can be implemented with reduced system requirements and without the use of a reference point is remote measurement of the normal vector to a flat surface. This measurement technique takes advantage of the fact that, for a flat surface, a change in laser frequency produces a global translation of the speckle pattern at the detector plane. The angle of incidence and the plane of incidence of the laser beam are determined from the rate and the direction of speckle translation, respectively.

This phenomenon will now be investigated in more detail. The first step is to write an expression for the measured speckle intensity with no reference point by setting  $g_r = 0$  in Eq. (110), which leaves only the second term of the original four terms:

$$I(x_d, y_d, z_d; \lambda) = \left| \tilde{g}(f_x, f_y, f_z) \right|^2 \quad (163)$$

The inverse Fourier transform of Eq. (163) with respect to the spatial frequency variables is the autocorrelation function

$$P_{AC}(x, y, z) = \int \int \int_{-\infty}^{\infty} g^*(x_h, y_h, z_h) g(x + x_h, y + y_h, z + z_h) dx_h dy_h dz_h \quad (164)$$

of the complex scattering function, which has been identified previously as the central region in Figure 32(b).

We proceed with the evaluation of Eq. (164) by using Eq. (90) to write the complex scattering function in terms of the complex amplitude  $a(x, y)$  and the height profile  $h(x, y)$ . Given that the laser beam illuminates the object along the negative  $z$ -axis, the height function for a flat plate can be expressed in terms of the angle of incidence  $\theta_h$  and the azimuthal angle  $\phi_h$  as

$$h(x, y) = h_0 - x \cos \phi_h \tan \theta_h - y \sin \phi_h \tan \theta_h \quad (165)$$

where  $h_0$  is the height of the planar surface at  $x = y = 0$ . The resulting expression for the autocorrelation function given by Eq. (164) is

$$P_{AC}(x, y, z) = \delta(z + x \cos \phi_h \tan \theta_h + y \sin \phi_h \tan \theta_h) \times \int_{-\infty}^{\infty} \int_{-\infty}^{\infty} a^*(x_h, y_h) a(x + x_h, y + y_h) dx_h dy_h \quad (166)$$

The  $\delta$ -function in Eq. (166) limits the autocorrelation function to a planar region of space passing through the origin of the coordinate system and having the same orientation as the original scattering surface. Consequently, a measurement of the orientation of the scattering surface could be performed through the standard speckle-pattern-sampling technique but without using a reference point.

There is a simpler approach to determining the orientation, however, that does not require the acquisition of a series of speckle frames at incremental laser-frequency shifts. This approach is based on measuring the speckle motion in the detector plane caused by varying the laser wavelength. To develop the theory governing this approach, we first evaluate Eq. (163) for the planar height profile given by Eq. (165):

$$|\tilde{g}(f_x, f_y, f_z)|^2 = |\tilde{a}(f_x - f_z \tan \theta_h \cos \phi_h, f_y - f_z \tan \theta_h \sin \phi_h)|^2 \quad (167)$$

Equation (167) is an expression for the speckle intensity at the detector plane in terms of spatial-frequency coordinates. It is useful for determining the effect that tuning the laser frequency has on an individual speckle lobe. Mathematically, the  $f_x$  and  $f_y$  coordinates of a speckle lobe are tracked by keeping the arguments of  $\tilde{a}$  constant as  $f_z$  is varied through changing the wavelength. Thus, for the first argument

$$f_{x_1} - f_{z_1} \tan \theta_h \cos \phi_h = f_{x_2} - f_{z_2} \tan \theta_h \cos \phi_h \quad , \quad (168)$$

and for the second argument

$$f_{y_1} - f_{z_1} \tan \theta_h \sin \phi_h = f_{y_2} - f_{z_2} \tan \theta_h \sin \phi_h \quad , \quad (169)$$

where the subscripts 1 and 2 denote speckle measurements at wavelengths  $\lambda_1$  and  $\lambda_2$ , respectively. The orientation of the scattering plane can be determined by solving Eqs. (168) and (169) for  $\theta_h$  and  $\phi_h$ . In terms of the spatial-frequency differences

$$\Delta f_x = f_{x_2} - f_{x_1} = \frac{l_{d_1}}{\lambda_1} - \frac{l_{d_2}}{\lambda_2} \quad , \quad (170)$$

$$\Delta f_y = f_{y_2} - f_{y_1} = \frac{m_{d_1}}{\lambda_1} - \frac{m_{d_2}}{\lambda_2} \quad , \quad (171)$$

and

$$\Delta f_z = f_{z_2} - f_{z_1} = \frac{1 + \sqrt{1 - l_{d_1}^2 - m_{d_1}^2}}{\lambda_1} - \frac{1 + \sqrt{1 - l_{d_2}^2 - m_{d_2}^2}}{\lambda_2} \quad (172)$$

of a speckle lobe at the two wavelengths, these angles can be written as

$$\tan \theta_h = \frac{\sqrt{\Delta f_x^2 + \Delta f_y^2}}{|\Delta f_z|} \quad (173)$$

and

$$\tan \phi_h = \frac{\Delta f_y}{\Delta f_x} \quad (174)$$

Equations (173) and (174) are general results for calculating the angle of incidence  $\theta_h$  and the plane of incidence  $\phi_h$  given the original direction cosines  $(l_{d_1}, m_{d_1})$  of a speckle lobe at wavelength  $\lambda_1$  and the new direction cosines  $(l_{d_2}, m_{d_2})$  that this speckle lobe takes at wavelength  $\lambda_2$ .

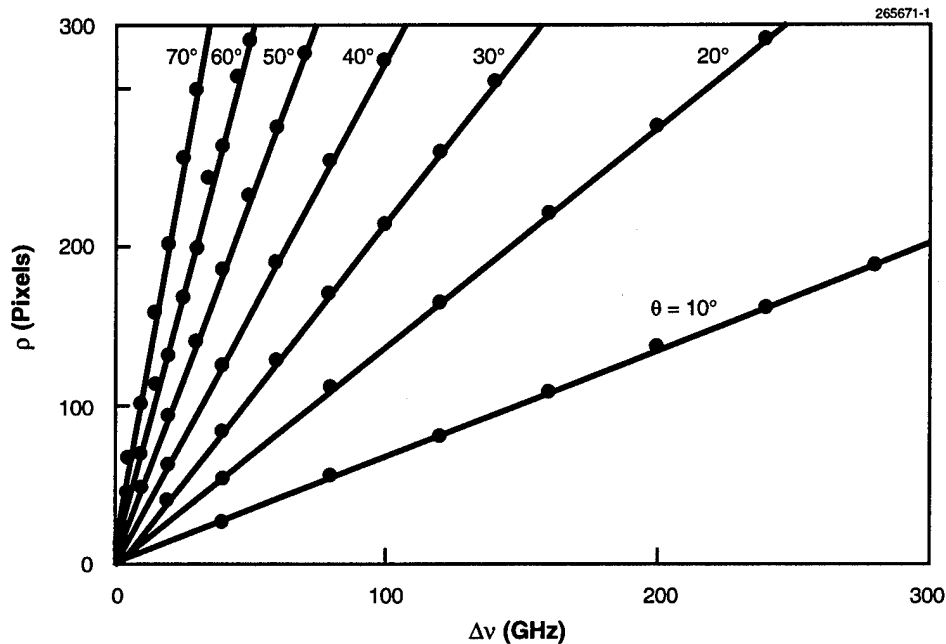


Figure 38. Remote angle-of-incidence measurements for a flat plate being illuminated by a tunable laser at various angles. As the laser frequency offset  $\Delta\nu$  increases, the speckle pattern shifts from the original position. The magnitude  $\rho$  of the shift increases with angle of incidence.

If wavelength aberration, detector-plane distortion, and depth-of-field aberration are negligible or have been corrected, Eqs. (170)–(172) can be written in terms of the location  $(x_d, y_d, z_d)$  of the speckle lobe on the detector plane and the frequency shift  $\Delta\nu$  as

$$\Delta f_x = \frac{x_{d_1} - x_{d_2}}{\lambda_0 z_d} \quad , \quad (175)$$

$$\Delta f_y = \frac{y_{d_1} - y_{d_2}}{\lambda_0 z_d} \quad , \quad (176)$$

and

$$\Delta f_z = 2 \left( \frac{1}{\lambda_1} - \frac{1}{\lambda_2} \right) = -2 \frac{\Delta v}{c} \quad . \quad (177)$$

Eqs. (173) and (174) then simplify such that every speckle lobe shifts by the same amount and in the same direction in the detector plane. From Eq. (173), the magnitude of this shift is

$$r_d = -2z_d \frac{\Delta v}{v_0} \tan \theta_h \quad , \quad (178)$$

and from Eq. (174), the direction of this shift is

$$\phi = \phi_h \quad . \quad (179)$$

Thus, the angle of incidence  $\theta_h$  and plane of incidence  $\phi_h$  can be determined remotely by measuring the magnitude and direction, respectively, of the speckle shift caused by tuning the laser frequency.

To apply Eq. (178) to the determination of  $\theta_h$  in practice, the detector distance  $z_d$  must be known. This requirement can be circumvented, however, by placing a Fourier-transform lens in front of the detector array. Then,  $z_d$  is replaced by the focal length  $f$  of the Fourier-transform lens and the measurement is insensitive to object distance. The object distance allowed by a Fourier-transform lens is limited, however, because the range of spatial frequencies accepted by the lens decreases with increasing object distance.

Laboratory measurements were performed using the optical system shown in Figure 19 to verify this technique for remote sensing of angular orientation of flat surfaces. In these measurements, a flat plate was mounted on a system of rotary stages that enabled control of the angle of incidence  $\theta_h$  and the plane of incidence  $\phi_h$  and the plate was spot illuminated with a beam from the Ti:sapphire laser. The general behavior predicted by Eqs. (178) and (176) was readily observed; as the laser frequency varies, the entire speckle pattern shifts in the direction  $\phi_h$  with a rate that increases with increasing  $\theta_h$ .

To make more quantitative measurements, the laser frequency was stepped by a known amount and the CCD frames compared at the two frequencies by calculating a 2D cross-correlation of the speckle frames. The magnitude and the direction of offset from the origin of the cross-correlation peak provided a measurement of  $r_d$  and  $\phi$ . Figure 38 is a family of plots of the magnitude of the speckle shift (in units of pixels  $\rho$ ) versus laser-frequency shift  $\Delta v$  for angles of incidence  $\theta_h$  ranging between  $10^\circ$  and  $70^\circ$  in  $10^\circ$  increments. In this figure, the  $\rho$  versus  $\Delta v$  curves are straight lines and the slope of these lines is proportional to  $\tan \theta_h$ , as predicted by Eq. (178). A series of measurements with constant  $\theta_h$  and variable

$\phi_h$  was also performed. The linear relation between  $\phi$  and  $\phi_h$  predicted by Eq. (179) was confirmed in these measurements.

Although no attempt was made to optimize the measurement technique or to access the accuracy to which the angles  $\theta_h$  and  $\phi_h$  can be measured in practice, it does appear that this technique offers the capability for accurate, real-time, remote measurements of surface orientation. (A by-product of the technique is a means for estimating the flatness of a surface by the strength of the cross-correlation peak.) This technology has many potential applications in robot vision and machine vision where surface-orientation information can greatly aid in the interpretation of object scenes.

### 6.1.3 3D Image Recovery from Autocorrelation Support

Knowledge of the 3D autocorrelation function would suffice in some pattern-recognition applications. But full knowledge of the 3D image is desired in many situations. For remote objects, where a reference point is impractical and where large target distances make it difficult to produce a virtual reference point through coherent detection, it would be highly desirable to be able to recover the missing Fourier-phase information from the 3D autocorrelation function. In speckle-pattern sampling, however, the function for which the autocorrelation function is known is complex, so there is not the typical constraint required for iterative phase retrieval—that the function being recovered is real and nonnegative.

The new 3D-image-recovery concept described and illustrated here is based on knowledge of the support of the 3D autocorrelation, support meaning the region in space where the function is nonzero valued. The development of robust algorithms based on this concept is currently an area of active research and no general solutions have been found. A framework is provided, however, for further development in this area and the general concept is illustrated by recovering the height values of a 25-point array of scatterers from its measured autocorrelation support.

The mathematical framework is introduced by assuming that the scattering function  $g(x, y, z)$  consists of a set of  $N$  discrete scatterers at locations  $(x_j, y_j, z_j)$ , where the subscript represents the  $j^{\text{th}}$  scatterer. (In practice, these scattering points can represent resolution cells in the 3D image of a continuous surface.) Following Eq. (91), the complex scattering function for this collection of points is written as

$$g(x, y, z) = \sum_{j=1}^N g_j \delta(x - x_j) \delta(y - y_j) \delta(z - z_j) \quad (180)$$

The measured quantity is the autocorrelation function of  $g(x, y, z)$ , which can be calculated by substituting Eq. (180) for  $g(x, y, z)$  into Eq. (164) and using the  $\delta$ -functions to evaluate the integrals:

$$P_{AC}(x, y, z) = \sum_{j=1}^N \sum_{k=1}^N g_j^* g_k \delta(x + x_j - x_k) \delta(y + y_j - y_k) \delta(z + z_j - z_k) \quad (181)$$

The meaning of Eq. (181) can be clarified by using Eq. (180) to eliminate one of the summations. There are two forms for the result, depending on which summation in Eq. (181) is eliminated:

$$\begin{aligned}
P_{AC}(x, y, z) &= \sum_{j=1}^N g_j^* g(x + x_j, y + y_j, z + z_j) \\
&= \sum_{j=1}^N g_j g^*(-x + x_j, -y + y_j, -z + z_j)
\end{aligned}
\tag{182}$$

The two expressions in Eq. (182) have simple interpretations. The upper form expresses the autocorrelation function as the summation of  $N$  copies of  $g(x, y, z)$ , with successive copies being shifted such that each of the  $N$  scattering points is at the origin of the coordinate system for one of the copies. More specifically, the  $j^{\text{th}}$  copy is shifted so that its  $j^{\text{th}}$  point is located at the origin, and the weighting factor for this copy is the complex conjugate of the scattering amplitude  $g_j$  for that point. Similar statements apply to the lower form in Eq. (182), except that the autocorrelation is expressed here as the complex conjugate of the summation of shifted copies of the inverted function  $g(-x, -y, -z)$ . Once again, the shifts successively place each of the  $N$  scattering points at the origin.

Figure 39 illustrates the above relation between the location of scattering points [Figure 39(a)] and the support of the autocorrelation function [Figure 39(b)] for a nine-point scattering object. In Figure 39(b), it is possible to pick out each of the nine copies of the scattering function as well as each of the nine copies of the inverted scattering function displayed in Figure 39(d). [Figure 39(c) will be referred to later in the description of the recovery algorithm.] The technique to be described below recovers the support of  $g(x, y, z)$ , or of  $g(-x, -y, -z)$ , to within an arbitrary spatial offset, by extracting one of the  $N$  copies from the autocorrelation function.

To formalize the notation, a support operator  $S$  is defined such that

$$S[f(x, y, z)] = \begin{cases} 0 & f(x, y, z) = 0 \\ 1 & f(x, y, z) \neq 0 \end{cases}
\tag{183}$$

Thus  $S$  produces a new function that is unit valued wherever the function that it is operating on is nonzero and zero valued elsewhere. Let

$$S_g(\mathbf{R}) = S[g(x, y, z)]
\tag{184}$$

represent the support of the scattering function. The vector notation  $\mathbf{R} = (x, y, z)$  is used for the argument of  $S_g$  to simplify the equations that follow. It is necessary to define the support of the autocorrelation function in a statistical sense,

$$S_{AC}(\mathbf{R}) = S[\langle |P_{AC}(x, y, z)| \rangle]
\tag{185}$$

to avoid the situation where overlapping points from different copies of  $g(x, y, z)$  might cause the autocorrelation function to add to zero. In practice, this situation corresponds to having speckle dropouts in the autocorrelation function that make it difficult to determine the support of the autocorrelation function in all regions of space. [One solution to this problem is to approximate the ensemble average in Eq. (185) by averaging the magnitude of  $P_{AC}$  from two or more measurements.]

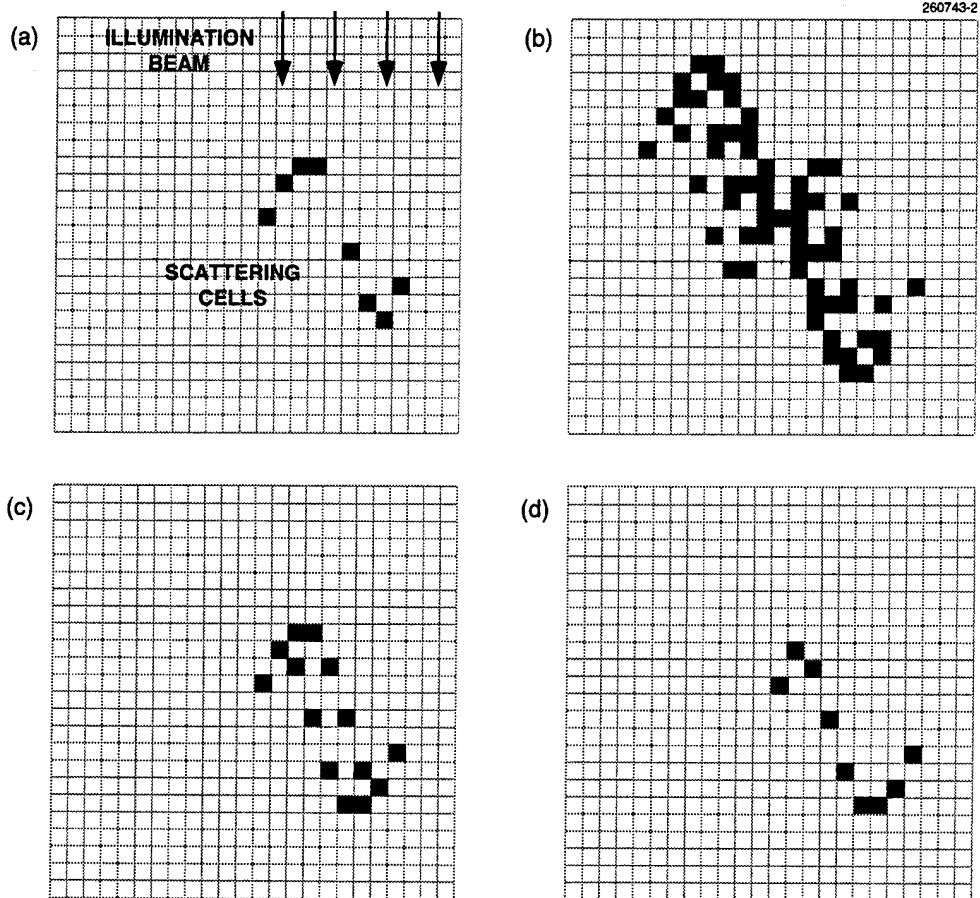


Figure 39. Illustration of the shift-intersection concept for recovering the 3D image from the support of the autocorrelation function.

Now that  $S_g$  and  $S_{AC}$  are defined,  $S_{AC}$  can be written in terms of  $S_g$  by referring to Eq. (181) and using the following facts:  $S[g_j] = 1$  for each of the  $N$  points,  $S[ab] = S[a]S[b]$ , and components in the summation cannot add to zero. The resulting expression for  $S_{AC}$  is

$$S_{AC}(\mathbf{R}) = S \left[ \sum_{j=1}^N S_g(\mathbf{R} + \mathbf{R}_j) \right] = S \left[ \sum_{j=1}^N S_g(-\mathbf{R} + \mathbf{R}_j) \right] \quad (186)$$

Equation (186) states what was already observed and what was illustrated in Figure 39: that the support of the autocorrelation function is the support of the sum of the supports of the various shifted copies of  $g$  making up the autocorrelation function.

The information available to work with from the measurement is the location of the support points for  $S_{AC}$ . These locations can be enumerated in terms of the locations  $\mathbf{R}_j$  of the  $N$  scattering points as

$$\mathbf{R}_{jk} = \mathbf{R}_k - \mathbf{R}_j \quad , \quad (187)$$

where the subscripts  $j$  and  $k$  each range from 1 to  $N$ . The points  $\mathbf{R}_{jk}$  are not all distinct; in fact, there are always  $N$  degenerate points  $\mathbf{R}_{1,1} = \mathbf{R}_{2,2} = \dots = \mathbf{R}_{NN}$  located at the origin. In terms of shifted copies of the scattering function,  $\mathbf{R}_{jk}$  in Eq. (187) can be interpreted as the  $k^{\text{th}}$  point on the  $j^{\text{th}}$  copy of  $g(x,y,z)$  or as the  $j^{\text{th}}$  point on the  $k^{\text{th}}$  copy of the inverted function  $g(-x,-y,-z)$ . Enumerating points in the autocorrelation-function support according to Eq. (187) is a useful tool for the analysis that follows, even though it presupposes that the problem at hand has been solved so that the proper indices can be assigned to each point.

The recovery technique for extracting a single copy of the scattering function involves taking the intersection, or overlap, of a series of shifted copies of the autocorrelation function support with shift values selected from among the points  $\mathbf{R}_{jk}$ . To motivate this approach, consider the intersection of a single shifted copy of the autocorrelation function with the original autocorrelation function. Through the use of Eq. (186), the support of the shifted autocorrelation-function can be written as

$$\begin{aligned} S_{AC}(\mathbf{R} - \mathbf{R}_{jk}) &= S \left[ S_g(\mathbf{R} + \mathbf{R}_j) + \sum_{\substack{l=1 \\ l \neq k}}^N S_g(\mathbf{R} - \mathbf{R}_{jk} + \mathbf{R}_l) \right] \\ &= S \left[ S_g(-\mathbf{R} + \mathbf{R}_k) + \sum_{\substack{l=1 \\ l \neq j}}^N S_g(-\mathbf{R} + \mathbf{R}_{jk} + \mathbf{R}_l) \right] \end{aligned} \quad (188)$$

In Eq. (188), the  $l = k$  term and the  $l = j$  term have been separated out of the summation in the upper and lower forms, respectively. Equation (188) is now multiplied by the unshifted autocorrelation-function support and the result written as

$$\begin{aligned} S_{AC}(\mathbf{R}) S_{AC}(\mathbf{R} - \mathbf{R}_{jk}) &= S \left[ S_g(\mathbf{R} + \mathbf{R}_j) + S_{AC}(\mathbf{R}) \sum_{\substack{l=1 \\ l \neq k}}^N S_g(\mathbf{R} - \mathbf{R}_{jk} + \mathbf{R}_l) \right] \\ &= S \left[ S_g(-\mathbf{R} + \mathbf{R}_k) + S_{AC}(\mathbf{R}) \sum_{\substack{l=1 \\ l \neq j}}^N S_g(-\mathbf{R} + \mathbf{R}_{jk} + \mathbf{R}_l) \right] \end{aligned} \quad (189)$$

It is unnecessary to multiply the separated terms in front of the summations by  $S_{AC}$  because these terms are completely contained within  $S_{AC}$ . Equation (189) shows that for any shift  $\mathbf{R}_{jk}$  there are at least two copies of  $S_g$  that survive unaffected by the shift-and-multiply operation, namely, the  $j^{\text{th}}$  copy and the  $k^{\text{th}}$  inverted copy. Equation (189) also indicates that many points not contained within these two copies are likely to be eliminated because of the offset between  $S_{AC}$  and its shifted replica.

Figure 39(c) shows the effect that applying a single shift-and-multiply operation can have on reducing the number of points. In this instance, the shift corresponds to placing the leftmost point of  $S_{AC}$  in Figure 39(b) onto the point of symmetry of the unshifted version of  $S_{AC}$  and taking the intersection. Note that this single shift has eliminated all points except for those that are in  $S_g$  and its inverted copy. In Figure 39(d), the inverted copy of  $S_g$  has been reconstructed by applying one or more of the remaining shifts from Figure 39(c).

A single shift-and-multiply operation is insufficient for determining  $S_g$  except, for instance, in the trivial case of a flat rectangular plate with  $\mathbf{R}_{jk}$  taken as one of the corners of  $S_{AC}$ . In general, a technique is needed for selecting additional shift values from  $\mathbf{R}_{jk}$  that will further reduce the number of points in  $S_{AC}$  while leaving a single copy of  $S_g$  intact. As stated previously, the first shift is completely arbitrary; let us denote it by  $\mathbf{R}_{j_1 k_1}$ . Equation (189), however, shows that once the first shift has been chosen, the second shift must lie either on the  $j_1^{\text{th}}$  copy of  $S_g$  or on the  $k_1^{\text{th}}$  inverted copy of  $S_g$  for one of these copies to remain positively intact. Thus, the second shift normally breaks the symmetry by eliminating points from one of these two copies. The third and subsequent shifts must then all lie on either the  $j_1^{\text{th}}$  copy of  $S_g$  or on the  $k_1^{\text{th}}$  inverted copy of  $S_g$ , depending on which one survived the second shift-and-multiply operation.

Assume, for the time being, that a means exists for correctly choosing subsequent shifts and that all  $N$  shifts have been applied that correspond to the particular copy of  $S_g$  being extracted. If the symmetry was broken such that the regular copy of  $S_g$  is reconstructed, the result of applying all  $N$  shifts is

$$\begin{aligned} & S_{AC}(\mathbf{R} - \mathbf{R}_{j_1,1}) S_{AC}(\mathbf{R} - \mathbf{R}_{j_1,2}) \dots S_{AC}(\mathbf{R} - \mathbf{R}_{j_1,N}) \\ &= S \left[ S_g(\mathbf{R} + \mathbf{R}_{j_1}) + \prod_{k=1}^N \sum_{\substack{l=1 \\ l \neq k}}^N S_g(\mathbf{R} - \mathbf{R}_{j_1 k} + \mathbf{R}_l) \right] \end{aligned} \quad (190)$$

It is not necessary to write  $S_{AC}(\mathbf{R})$  explicitly on the left side of the equal sign in Eq. (190) because one of the  $N$  factors degenerates to this form. In deriving Eq. (190) from Eq. (188), the following sequence of equalities have been used:

$$\begin{aligned} & \prod_{k=1}^N S[S(a) + S(b_k)] \\ &= S \left[ S(a)^N + S(a)^{N-1} \sum_{k=1}^N S(b_k) + \dots + \prod_{k=1}^N S(b_k) \right] \\ &= S \left[ S(a) \left( 1 + \sum_{k=1}^N S(b_k) + \dots \right) + \prod_{k=1}^N S(b_k) \right] \\ &= S \left[ S(a) + \prod_{k=1}^N S(b_k) \right] \end{aligned} \quad (191)$$

The expression corresponding to Eq. (190) for reconstruction of the inverted copy of  $S_g$  is

$$S_{AC}(\mathbf{R} - \mathbf{R}_{1,k_1}) S_{AC}(\mathbf{R} - \mathbf{R}_{2,k_1}) \dots S_{AC}(\mathbf{R} - \mathbf{R}_{N,k_1}) \\ = S \left[ S_g(-\mathbf{R} + \mathbf{R}_{k_1}) + \prod_{j=1}^N \sum_{\substack{l=1 \\ l \neq j}}^N S_g(-\mathbf{R} + \mathbf{R}_{j k_1} + \mathbf{R}_l) \right] \quad (192)$$

Equations (190) and (192) state that applying all  $N$  shifts corresponding to a given copy, or inverted copy, of  $S_g$  leaves that copy or the inverted copy intact, respectively. These equations also state that there may be additional points left over that survived all  $N$  shifts but do not lie on the given copy of  $S_g$  or the inverted copy of  $S_g$  respectively. For surfaces with sufficient complexity, points not on  $S_g$  will probably not survive all  $N$  shift-and-multiply operations, and Eqs. (190) and (192) represent acceptable solutions to the recovery of  $S_g$ .

A case where extra points remain is a flat rectangular plate with a hole in it. In this situation, there is insufficient information from  $S_{AC}$  alone to determine information about this hole, causing the hole to fill in in the reconstruction. It is likely, however, that the boundaries of the hole can also be reconstructed by using additional information available from the measurement, that is, the values of the product  $g_j^* g_k$  for each of the points  $\mathbf{R}_{j k_1}$ . Indeed, it may be possible to also determine  $g_j$  in general situations by combining the technique described here with other phase-retrieval techniques.

Now that the result has been described of correctly choosing a sequence of shifts that lie on the support of the copy of  $S_g$  being reconstructed, some ideas are presented that help determine these shifts. Note that in practical situations it is not necessary to apply all  $N$  shifts; the copy of  $S_g$  often reconstructs for a small subset of these shifts. Although no general solution has yet been found for determining shifts, there has been success in certain cases where there is a priori target information. The following makes some general observations about choosing shifts, then describes and illustrates the solution for a special case.

Recall that all points on the copy of  $S_g$  being recovered must have survived all previous shift-and-multiply operations. Therefore, the first general observation about choosing new shifts is that they must come from the pool of candidates that have survived all previous shifts. The number of points in this candidate pool decreases as the algorithm proceeds.

Thus far it has been assumed intrinsically in the mathematics that scattering from the  $N$  scattering points is dominated by single scattering. An additional assumption that aids in selection of shift values is that there is only one scattering point for each transverse location  $(x, y)$  in the illumination beam. (This assumption is equivalent to the opacity condition for surface scattering that has been used throughout the report.) The advantage of these two assumptions is that the function to be recovered is known to be single valued. The above two conditions can be verified by inspecting  $S_{AC}$  along the  $z$ -axis of the coordinate system. If these conditions are satisfied, the support  $S_{AC}$  is limited to the point  $z = 0$  along the  $z$ -axis, as depicted in Figure 39(b). This test works because there can be no overlap between the scattering object and a copy of the scattering object that is translated in the  $z$  direction for the given conditions. In practice, there may be some spread of the support  $S_{AC}$  about the  $z = 0$  point on the  $z$ -axis. For example, there may be multiple scattering between points that are in close proximity, or, in the case of a continuous surface,

one transverse resolution cell may extend over more than one longitudinal resolution cell for steep-sloped surfaces. In these cases, it is still possible to apply the shift-and-multiply algorithm as long as there is a vertical tolerance for determining whether two points overlap.

The following is an example of a situation where it has been demonstrated with simulated and measured data that subsequent shifts can be determined in a straightforward manner. In this example, the above two assumptions are coupled with knowledge of the lateral support of  $S_g$ . The object consists of an  $M \times M$  array of scattering points located on a square grid, with every grid point occupied by a scattering point. The relative height values of the individual points are desired. The lateral support of  $S_{AC}$  for this scattering function consists of a  $2M - 1 \times 2M - 1$  array. After the first shift, it is often possible to pick out two  $M \times M$  blocks in the lateral support of the product of  $S_{AC}$  and its shifted replica. These blocks correspond to the lateral support of the copy of  $S_g$  and of the inverted copy of  $S_g$  that survived the first shift-and-multiply operation.

The value of the second shift is determined by selecting a lateral position within one of these blocks that contains only one point. This point must be a correct shift because it is known that every grid point in the scattering function contains a scattering point. Application of this point as a shift eliminates many points in the  $M \times M$  block that was not selected. Any additional lateral positions in the surviving  $M \times M$  block containing a single point can also be applied as shifts, producing more lateral positions with single scattering points. In all cases tested, this algorithm converges correctly to a copy of  $S_g$  or an inverted copy of  $S_g$ .

The results of this algorithm are now described for the reconstruction of the pin heights for the  $5 \times 5$  array depicted in Figure 40. The tops of the individual pins were rounded to simulate point scatterers by making the light appear to emanate from the virtual focal point. The heights of the 25 pins were set at values obtained by a random number generator with the height difference between the highest and lowest points being 10 mm. The measurement was performed using the optical system described in Figure 19 without a reference point. The data array consisted of 256  $128 \times 128$ -pixel speckle frames with a frequency increment of 5 GHz between frames, yielding a total bandwidth of  $B = 1.28$  THz and a range resolution of  $\Delta z = 117 \mu\text{m}$ . The autocorrelation-function support  $S_{AC}$  was obtained by performing a 3D FFT of the data array and decimating the result to a  $9 \times 9 \times 256$  array such that each position in the  $9 \times 9$  lateral support array of  $S_{AC}$  was accounted for. The magnitude of the FFT was retained to allow for varying the threshold value in estimating  $S_{AC}$ .

The maximum number of points that should be in  $S_{AC}$  for ideal data from a 25-point scatterer is 601, accounting for a degeneracy of 25 at the origin. To produce all support points that should be in the estimate of  $S_{AC}$  it was necessary, however, to set the threshold level low enough so that three or four times this number of points occurred in the estimate of  $S_{AC}$ . These extra points did not seem to have much of a negative impact on the speed of convergence of the algorithm. In summary of the results, the relative height values for all 25 pins were reconstructed successfully for both the normally oriented object and the inverted object. The reconstruction results were in close agreement with the actual settings, with a maximum height error for a typical reconstruction of approximately  $\Delta z/2 = \pm 60 \mu\text{m}$  and a standard deviation of the height error of  $37 \mu\text{m}$ .

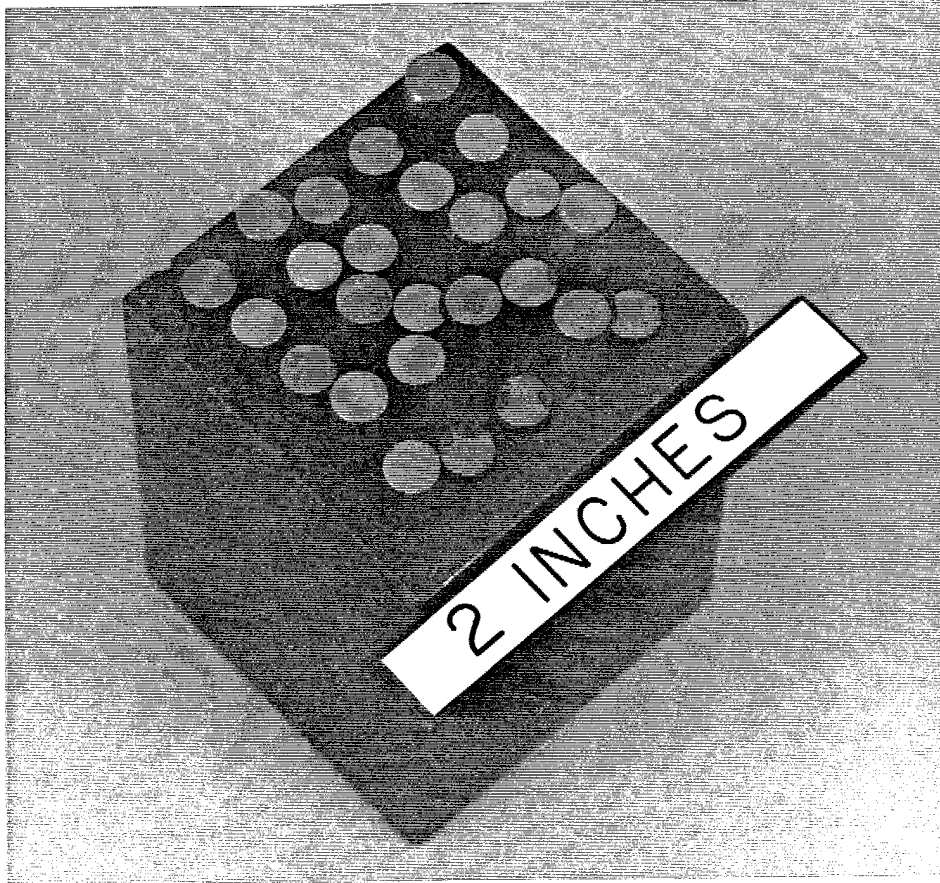


Figure 40. Photograph of a 25-point scattering array used to demonstrate the shift-intersection concept for 3D phase retrieval.

The success demonstrated with recovery of pin heights and the similarity between a rectangular array of scattering points and a continuous surface being imaged with a finite number of pixels encourage further research on the application of the general technique to more complicated objects. One approach to be investigated for applications where the conventional image is available is using this image to determine the lateral support of  $S_g$ .

## 6.2 IMAGE SPECKLE

The imaging techniques described thus far are based on speckle occurring in the radiation pattern of the scattering object. Two additional 3D-imaging techniques based on image speckle (speckle present in the conventional image of a coherently illuminated object) are now described. In these techniques, range information is obtained from the wavelength dependence of speckle, transverse information through conventional imaging.

### 6.2.1 Reference-Plane Technique

Figure 41 is a basic optical configuration for the reference-plane implementation of the image-speckle technique for 3D imaging. In this figure, a collimated laser beam from a tunable laser is divided by the beamsplitter into a beam that illuminates the scattering object and a beam that illuminates the reference plane. Scattered light from the object and the reference plane is recombined by the beamsplitter and imaged by the lens with magnification  $M$  onto the detector array. Thus, a scattering point  $P_h$  with transverse coordinates  $(x_h, y_h)$  is imaged onto the detector at coordinates  $x_d = Mx_h$  and  $y_d = My_h$  (It is assumed that the imaging system has sufficient depth of field to cover the range extent of the object and any range offset of the reference beam. The system may also be telecentric so that any defocus error does not affect the apparent position of a surface point). Because all imaging systems have a finite point-spread function, the light that reaches a given image point on the detector comprises light scattered from a small surface patch surrounding the corresponding object point. Consequently, interference between these components makes the image formed at the detector plane speckled. The average speckle size equals the imaging system's point-spread function width. Thus, the object's transverse resolution is the speckle size divided by the magnification  $M$ .

Let us next consider how range resolution is achieved. If the range origin of the object's height-profile function is defined to be at the reflected image of the reference plane into object space, then the optical pathlength difference between the object beam and the reference beam for an image point at detector coordinates  $(x_d, y_d)$  is  $2z_h$ ; the factor of 2 accounts for the round-trip pathlength difference. As the laser frequency is tuned, this pathlength difference causes the two components to alternate between constructive and destructive interference, producing a periodic modulation of the speckle intensity. The rate of modulation is proportional to the pathlength difference  $2z_h$ . The frequency change  $\Delta\nu_D$  required to induce one complete oscillation of the speckle intensity is

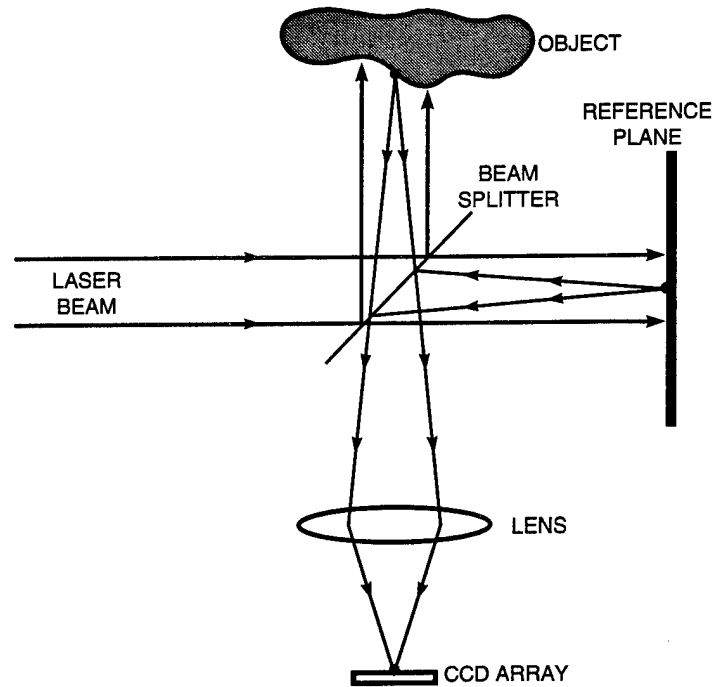
$$\Delta\nu_D = \frac{c}{2z_h} \quad (193)$$

Thus, measuring the speckle intensity as a function of laser frequency allows determination of  $z_h$ .

To address the accuracy to which  $z_h$  can be measured, first assume a simple intensity measurement that counts only the number of complete intensity oscillations. If  $B$  is the total bandwidth of the frequency scan, the number of oscillations that occur over the entire frequency scan is  $B/\Delta\nu_D$ . By equating the number of intensity oscillations with the number of resolution cells  $z_h/\Delta z$  and substituting the expression for  $\Delta\nu_D$  from Eq. (193),

$$\Delta z = \frac{c}{2B} \quad (194)$$

is obtained, which is the same expression given in Eq. (56) for wavelength decorrelation and in Eq. (124) for speckle-pattern sampling. Thus, these three techniques have similar range-resolution characteristics.



265352-1

Figure 41. Conceptual diagram for reference-plane implementation of image-speckle technique.

Once again,  $\Delta z$  is the discrete spacing between range planes obtained by using an FFT to calculate the whole number of speckle oscillations. For high-quality measurements, it is possible to further subdivide the resolution cell by accounting for the phase of the intensity oscillation, provided that the spread in  $z_h$  over a lateral resolution cell is smaller than  $\Delta z$ . (As explained in Section 6.1.1, maximizing the DFT is one such technique for enhancing range resolution.) For example, a typical frequency scan of  $B = 15$  THz for a diode laser produces a raw range resolution of  $\Delta z = 10 \mu\text{m}$ ; a subdivision of the period of oscillation by one part in ten would yield a range resolution of  $1 \mu\text{m}$ .

The main advantage of image-speckle techniques over speckle-pattern sampling is that there is already a one-to-one correspondence between points in the detector array and points in object space. Therefore, it is not necessary to do a 2D Fourier transform of each speckle frame to obtain the transverse information, nor is it necessary to sample the entire speckle pattern to obtain a high-resolution image of a single object point. These facts allow one to select individual image points or regions of interest in the image without processing or collecting data from points in between, greatly reducing the system demands when only sparse imaging is required.

A disadvantage of image-speckle techniques in general is that the depth of field of the 3D image is limited to the depth of field of a conventional imaging system. The speckle-pattern-sampling condition in Eq. (141) for negligible depth-of-field aberration can be applied to conventional imaging if  $z_h$  is interpreted as the depth of field. Because depth of field goes as the square of the transverse resolution, the

unaberrated range extent of a 3D image becomes severely limited for images with high transverse resolutions. For example, by Eq. (141), a transverse resolution of  $10\ \mu\text{m}$  limits the depth of field to  $125\ \mu\text{m}$  at  $\lambda_0 = 0.8\ \mu\text{m}$ . In speckle-pattern sampling, depth-of-field aberration can be corrected in the processing. Correction of depth-of-field effects in the image-speckle technique, however, requires the acquisition of a series of images at different focal positions.

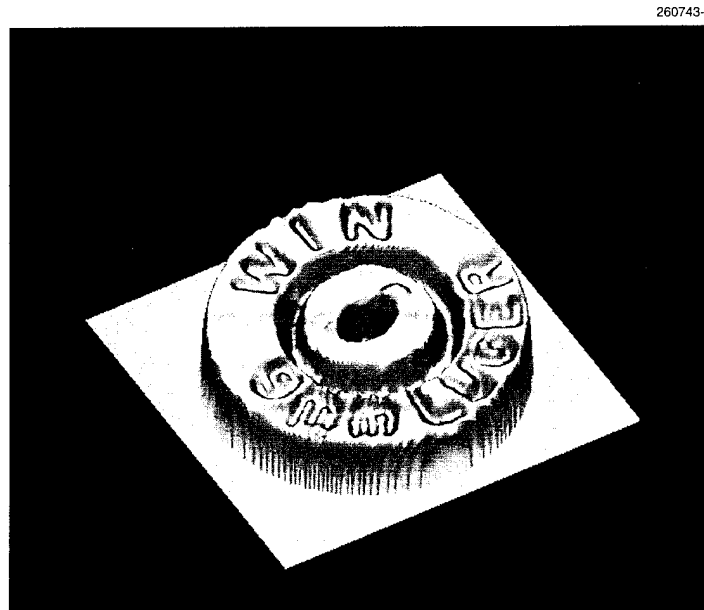


*Figure 42. 3D image of firing-pin indentation on a cartridge casing obtained using the reference-plane implementation of the image-speckle technique.*

Figure 42 is a 3D image illustrating the reference-plane technique for imaging the firing pin imprint on a cartridge casing. This image is representative of a class of applications of the 3D imaging techniques described in Section 6 to forensics.

### **6.2.2 Two-Source-Point Technique**

The reference-plane technique depicted in Figure 41 becomes impractical to implement for large objects because of the need for a correspondingly large reference plane and beamsplitter. Although variations of this technique that overcome these size restrictions are possible, these variations require relatively long separated paths for the object beam and the reference beam, making them sensitive to turbulence and vibration.

An image-speckle-based technique is now described that is well suited to 3D imaging of large objects. The key to this technique is that the reference beam is implemented automatically; refer to Figure 43 for a description of the technique and an explanation of its principle of operation. A laser beam from a tunable laser is split into two parts, producing two coherent source points at positions  $P_1$  and  $P_2$  that are separated by the distance  $R_{12}$ . (A convenient means for producing the two source points is through fiber-optic cables.) For the purpose of this explanation, the origin of the coordinate system is placed halfway between points  $P_1$  and  $P_2$  so that these points are located at the coordinates  $(x_1, y_1, z_1)$  and  $(-x_1, -y_1, -z_1)$ . The beams from these source points have sufficient divergence and are pointed so that they simultaneously illuminate the region of interest.

Transverse information is obtained in the same manner as for the reference-plane technique. Once again, the image is speckled due to surface roughness and coherent illumination, and the  $z$ -axis is defined to be parallel to the optical axis of the imaging system. Consider the point  $P_h$  lying on the surface of the object at position  $(x_h, y_h, z_h)$ . The coordinates  $x_h$  and  $y_h$  of this point are known, to within the transverse resolution of the optical system, by the location  $x_d$  and  $y_d$  of its image on the detector array. If the coordinate  $z_h$  corresponding to each value of  $x_h$  and  $y_h$  could be determined, then the desired 3D image would be obtained.

Let  $R_{1h}$  and  $R_{2h}$  be the distance from the points  $P_1$  and  $P_2$  to the point  $P_h$ , respectively, and let  $s$  be the pathlength difference between these two distances, that is,  $s = R_{2h} - R_{1h}$ . (For the purpose of this discussion, consider the optical pathlengths from the split in the optical fiber to the ends of the two fibers to be equal.) The measurement of  $z_h$  is based on determining the value of  $s$  for each value of  $x_h$  and  $y_h$ . To determine  $s$ , consider the effect that tuning the laser has on the speckled image. On average, approximately half the light reaching a given point in the detector array comes from each of the two source points. If  $s$  is nonzero, tuning the laser produces relative phase delays between the contributions from these two points. As with the reference-plane technique, these phase delays cause the contributions to alternate between destructive and constructive interference, resulting in a modulation of the speckle intensity. Once again, the rate of modulation is proportional to the pathlength difference. The frequency change  $\Delta\nu_D$  required to induce one complete oscillation of the speckle intensity is now

$$\Delta\nu_D = \frac{c}{s} \quad (195)$$

The factor of 2 is absent in the denominator because  $s$  accounts for the entire pathlength difference, there being no additional pathlength difference incurred in propagation from the scattering point to the detector. The resolution in  $s$  obtained by counting whole intensity oscillations is

$$\Delta s = \frac{c}{B} \quad (196)$$

Note that there is a loss in resolution of a factor of 2 in Eq. (196) compared to Eq. (193). Therefore, a frequency scan of  $B = 15$  THz produces a resolution of  $\Delta s = 20 \mu\text{m}$  rather than  $10 \mu\text{m}$ . Enhanced resolution beyond this limit is also possible with the two-source-point technique through measuring partial oscillation cycles.

Now that it has been shown how  $s$  can be measured, the next step is to relate  $s$  to the desired quantity  $z_h$ . This can be done by writing  $s$  in terms of  $z_h$  and the known quantities  $(x_h, y_h)$  and  $(x_1, y_1, z_1)$  as

$$s = \sqrt{(x_h + x_1)^2 + (y_h + y_1)^2 + (z_h + z_1)^2} - \sqrt{(x_h - x_1)^2 + (y_h - y_1)^2 + (z_h - z_1)^2} \quad (197)$$

and then solving for  $z_h$ , which yields

$$z_h = \frac{4(x_h x_1 + y_h y_1)z_1 \pm \frac{s}{2} \sqrt{16(x_h x_1 + y_h y_1)^2 + (s^2 - 4z_1^2)(s^2 - R_{12}^2 - 4x_h^2 - 4y_h^2)}}{s^2 - 4z_1^2} \quad (198)$$

Thus,  $z_h$  is determined to within the  $\pm$  sign ambiguity in Eq. (198). This ambiguity is readily resolved in practice. The correct sign depends on the relative positions of the source points and the object.

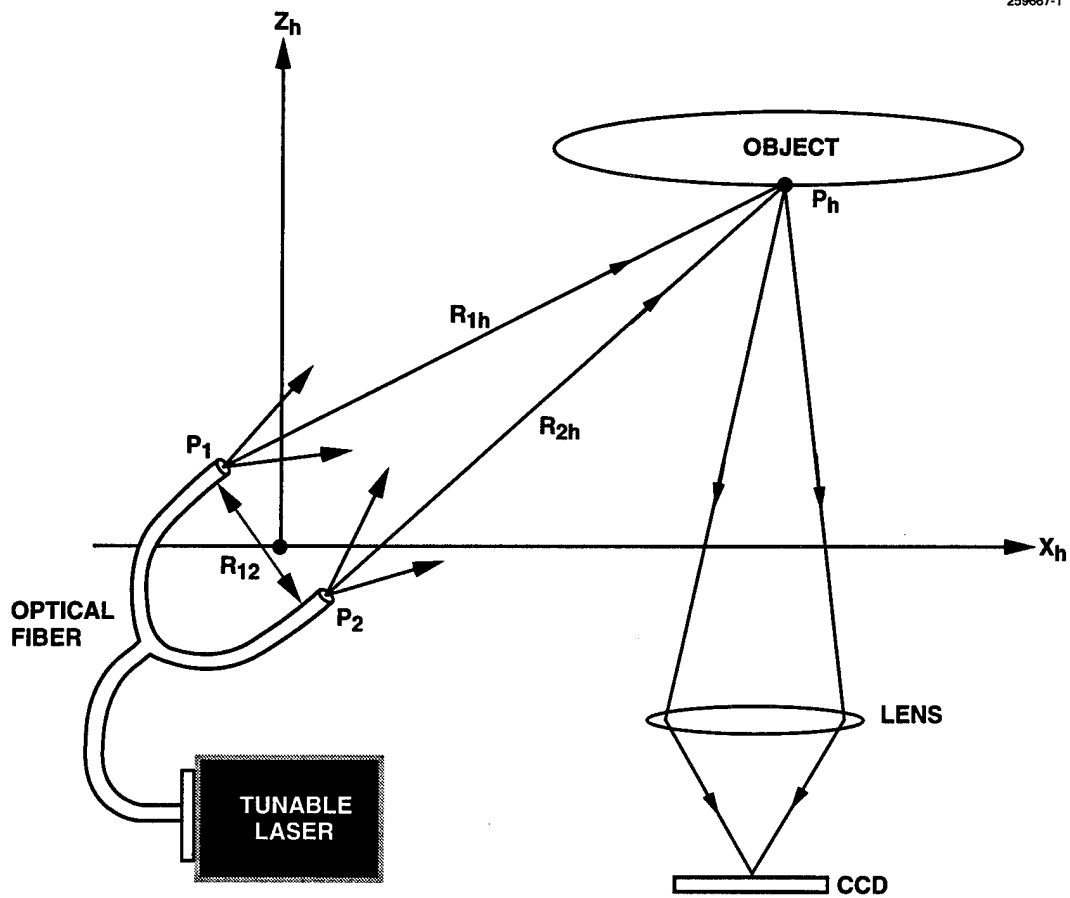


Figure 43. Coordinate system for the two-source-point implementation of 3D imaging using the image-speckle technique.

Uncertainties in the parameters in Eq. (198) can affect the accuracy of the measurement of  $z_h$ . Let us first look at the effects of an uncertainty in  $s$  on the uncertainty in  $z_h$ . To do so, we take the partial derivative of  $s$  with respect to  $z_h$  and study how this derivative  $\partial s/\partial z_h$  varies with the parameters  $(x_h, y_h, z_h)$  and  $(x_1, y_1, z_1)$ . This procedure shows that the magnitude of this ratio varies between 0 and 2, where a value of 0 corresponds to complete loss of range sensitivity. A value of 2 is impractical to achieve in practice because the surface must lie directly between the two points, and only one side of the surface could be illuminated from each beam. For parameters as suggested by Figure 43, the derivative is approximately  $\partial s/\partial z_h = 0.2$  so that there is a loss in range sensitivity of a factor of 5. Thus, for a 15-THz scan with no attempt to extend the resolution beyond counting whole cycles, the range resolution would be  $\Delta z = 100 \mu\text{m}$ .

The sensitivity of the measurement of  $z_h$  to uncertainties in  $(x_1, y_1, z_1)$  and  $(x_h, y_h)$  will now be addressed. With a good mechanical design, uncertainties in  $(x_1, y_1, z_1)$  are small and have minimal effects on  $z_h$ . For large objects, there may be much greater uncertainties in the values of  $(x_h, y_h)$ , or spreads in these quantities over a pixel, because of practical limits on transverse resolution over large fields. For the purpose of this discussion, let the two source points lie in the  $x$ - $z$  plane. Then by calculating  $\partial z_h/\partial y_h$ , it can be shown that the measurement of  $z_h$  is insensitive to errors in  $y_h$ . Uncertainties or spreads in  $x_h$ , however, can have a much greater effect on  $z_h$ ; the magnitude of  $\partial z_h/\partial x_h$  is approximately equal to the magnitude of  $z_h/x_h$ . This ratio should be as low as possible to minimize errors in  $z_h$ . Therefore, illumination angles with bisectors perpendicular to the camera axis offer the best immunity to errors in transverse position. These angles also offer good range resolution.

As mentioned previously, the depth of focus decreases as the transverse resolution of the optical system improves, limiting the usable range extent of the technique. This difficulty can be overcome, to a certain extent, by sequentially focusing on different range planes and using only those pixels within the depth of field. For example, a 100- $\mu\text{m}$  transverse resolution limits the depth of field to the order of 10 mm; an object with a 100-mm range extent could be imaged at full resolution by focusing sequentially at 10 different ranges. To minimize the effects of depth of field, the  $z$ -axis should be defined in a direction that minimizes the range extent, that is, normal to the average surface plane.

To increase the transverse area that can be imaged without losing transverse resolution, multiple cameras can be used to cover the whole area or individual cameras can be used for inspecting regions of interest. These cameras must be registered accurately in the transverse plane. For gently curved objects, the usable range extent can be extended by focusing the cameras individually.

The two-source-point technique is well suited to the measurement of contoured sheet-metal parts such as airframe and autobody panels. For these aerodynamic surfaces, the whole surface can be illuminated from a fairly low angle, providing good range resolution and immunity to transverse position errors. Additionally, because these surfaces are smooth and well behaved, the spread in  $z_h$  resulting from the variation of  $z_h$  within a resolution cell can be reduced by relating the spread in  $s$  for a given pixel to the orientation of the surface element being imaged and curve fitting to a smooth surface. Furthermore, if the desired surface shape is known, either mathematically or through a physical master, then deviations from the ideal signature can be related to deviations from true form.

Aside from its ease of implementation and robustness, another attractive feature of the two-source-point technique is that the pathlength difference  $s$  is limited in magnitude to the separation  $R_{12}$  between

the two source points. This fact limits the demands on the tunable laser by making the smallest frequency-step and coherence-length requirements independent of object size. Having two source points also does away with the need to adjust the path length of a reference beam for the given object and object position.

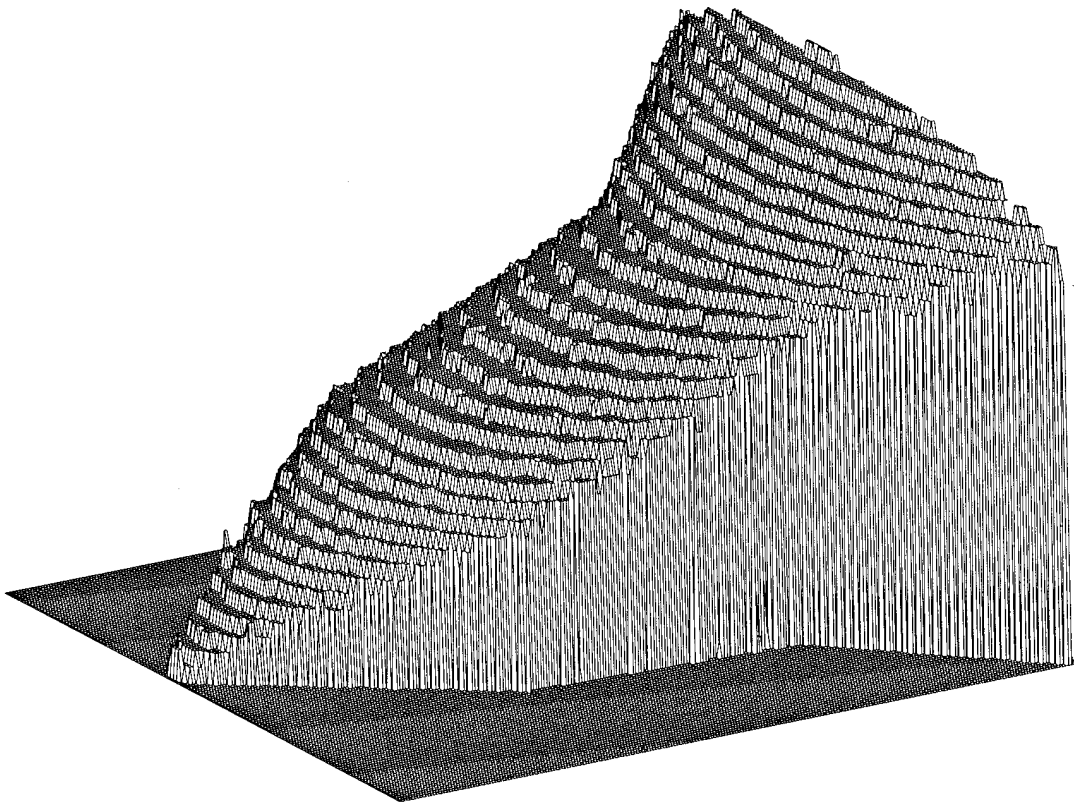


*Figure 44. 3D measurement of a triconic using the two-source-point implementation of the image-speckle technique.*

Figure 44 is a 3D image of a 50-mm-long triconic obtained using the two-source-point technique. The discrete range steps that are visible in the image can be removed by using a DFT to subdivide range-resolution cells. Two other phenomena were observed in the laboratory data. First, the degree of modulation of the speckle intensity varies from point to point in the image. The reason for this variation is that the speckled image is actually the interference pattern of two speckle patterns. If  $I_1$  and  $I_2$  represent the speckle intensity at a given pixel from each beam alone with the other beam blocked, then the intensity of the speckle pattern formed by the combination will vary about the value  $I_1 + I_2$  with amplitude

$I_{12} = 2\sqrt{I_1 I_2}$ . Thus, complete modulation occurs only when  $I_1 = I_2$ , and the amplitude of the sinusoidal component being extracted by the Fourier transform is  $I_{12}$ . Consequently, some pixels will be more susceptible to noise than others and there may be dropouts in the data for pixels with small values of  $I_{12}$ . In procedures such as curve fitting height values to a smooth surface, the result can be improved by using  $I_{12}$  to weight the individual height values.

The second observation is that turbulence affects the image speckle for large values of  $R_{1h}$  and  $R_{2h}$  by causing the speckle pattern to twinkle with no change in laser frequency. This effect can cause significant degradation of the data for slow frequency scans but becomes much less of a problem as the scan rate increases. If desired, turbulence compensation could be achieved by putting a monochromatic probe beam through the same path, or nearly the same path, calculating the phase offset necessary to keep the speckle pattern constant, and applying this compensation to the frequency-dependent data.

## 7. SUMMARY

This report has demonstrated techniques for using the wavelength dependence of laser-speckle-intensity patterns to determine information about the size, shape, and surface properties of a scattering object. Both statistical and deterministic approaches to this inverse-scattering problem are considered. In the statistical approach, known as the wavelength-decorrelation technique, fluctuations in the speckle intensity caused by changing the laser frequency are analyzed statistically and yield a measurement of the range-resolved laser radar cross section  $U(z)$  of the object for the given viewing angle. The functional form of  $U(z)$  is directly related to the object's size and shape as well as to the angular-scattering distribution of its surface materials. The extended tuning range of commercially available tunable lasers has been used to achieve submillimeter-range-resolution measurements of  $U(z)$  in laboratory demonstrations. These measurements agree well with calculations of  $U(z)$  based on the known shape of the object and on measured angular-surface-scattering properties. The wavelength-decorrelation technique has been implemented using both direct detection and a form of coherent detection that uses a range-reference plane (or a range-reference point) located near the object. The direct-detection approach requires additional signal processing, such as bispectral analysis, to recover the Fourier phase of  $U(z)$ .

The deterministic approach, referred to as the speckle-pattern-sampling technique, relates the detailed structure of the speckle-pattern intensity to the 3D distribution of scatterers on the object's surface. Excellent agreement has been demonstrated between the resulting 3D images and known object shapes. This 3D imaging technique requires either coherent detection or 3D phase retrieval. In the laboratory demonstrations, coherent detection was implemented using a reference point located near the object. A concept for 3D phase retrieval was also demonstrated on an array of point scatterers. In the speckle-pattern-sampling technique, longitudinal and lateral information is obtained through the wavelength dependence and spatial structure of the speckle pattern, respectively. The longitudinal resolution of an image is determined by the frequency scan length, whereas the lateral resolution is determined by the solid angle subtended by the detector array. As the resolution improves, these two effects mix so that more sophisticated sampling and data analysis are required. This 3D imaging technique is scalable from the microscopic regime to the large-scale regime, but the resolution-cell size becomes limited for larger objects because the number of resolution cells is restricted by the size of the 3D Fourier transform that can be processed by the computer.

An additional application of the wavelength dependence of speckle was demonstrated for the remote measurement of the normal vector to a surface. Because this technique is based on measuring the direction and magnitude of the shift in the speckle pattern caused by tuning the laser, it can be implemented with a simplified system.

A second class of 3D imaging techniques based on image speckle obtains the lateral information by conventional imaging and the longitudinal information from the wavelength dependence of image speckle. These image-speckle techniques have the advantage that high lateral resolution can be maintained over a large surface area by using additional cameras and individual regions of the surface can be inspected at high resolution. A disadvantage is that the depth of field is limited the same way as for conventional imaging. These techniques also require a reference beam. A particularly simple

implementation of the image-speckle technique using two point sources was described in which the reference beam is introduced automatically.

There are many potential commercial applications of the wavelength dependence of laser speckle in advanced manufacturing, dimensional metrology, machine vision, industrial inspection, and robotics. Work is currently under way to adapt this proven technology to these applications, including development of a fast frequency-scanning laser, a parallel processor engineered for real-time digital signal processing, and prototype demonstration systems designed for specific applications.

## APPENDIX ANGULAR-SCATTERING MEASUREMENTS

To understand and predict laser radar target signatures, it is important to be able to measure the angular-scattering properties of surface materials. For a monostatic radar configuration, the surface-scattering properties can be characterized by the monostatic reflectance distribution function  $f(\theta)$ . Basically,  $f(\theta)$  describes the variation with angle of incidence  $\theta$  of the strength of the backscattered radiation from a flat-shaped material sample. If the return signal is measured in units of laser radar cross section  $\sigma$  and if the surface area of the sample is  $A$ , then  $f(\theta)$  can be written as

$$f(\theta) = \frac{\sigma}{4\pi \cos^2 \theta A} \quad (A-1)$$

Equation (A-1) is obtained by applying Eq. (4) to the calculation of  $\sigma$  for a flat plate and solving for  $f(\theta)$ . The division by  $\cos^2 \theta$  in Eq. (A-1) accounts for two separate  $\cos \theta$  obliquity factors. One obliquity factor arises from the decrease in target irradiance  $E_0 \cos \theta$  (measured normal to the surface element) as  $\theta$  increases. The other obliquity factor accounts for the smaller projected area  $A \cos \theta$  of the surface with respect to the receiver at larger values of  $\theta$ . Equations (5) and (6) show how  $f(\theta)$  enters into the calculation of the laser radar cross section  $\sigma$  and the range-resolved laser radar cross section  $U(z)$ . Equation (3) gives the local angle of incidence  $\theta$  in terms of the height function  $h_1(x, y)$  that specifies the target shape.

The following describes two methods for measuring  $f(\theta)$ . The first method is to flood-illuminate a flat-shaped sample of the surface material with a uniform beam and to measure the laser radar cross section  $\sigma$  as a function of the angle of incidence  $\theta$ . The resulting values of  $\sigma$  are then substituted into Eq. (A-1). Although the optical system shown in Figure 19 was designed to measure a target's monostatic speckle pattern, it is also useful for measuring  $\sigma$  because it provides for flood-illumination of the target and detection of the return signal in the monostatic direction. When using this system to measure  $\sigma$ , the laser frequency is fixed and the integrated intensity at the detector plane is measured rather than tuning the laser and resolving the individual speckles. The value of  $\sigma$  is determined by comparing the result with the reading for a calibrated target with known  $\sigma$ .

The first method has two problems that limit its accuracy. First, because the surface sample is flood-illuminated, the incident beam also strikes the background and the supporting structure. The resulting unwanted contributions to the return signal affect the accuracy of the measurement. Second, a uniform illumination beam is difficult to produce. This fact results in uncertainty in the total power incident on the surface sample, which causes inaccuracies in the measurement of  $\sigma$ .

Both of these difficulties can be overcome by spot-illuminating the sample material so that the entire beam strikes the target. Let  $P_i$  be the total incident power on the surface sample. For spot-illumination, it is necessary to have an expression for  $f(\theta)$  based on knowledge of  $P_i$ , rather than on the assumption that the surface is uniformly illuminated with irradiance  $E_0$ . If the strength of the return signal is specified in terms of the radiometric intensity  $I = dP/d\Omega$ , where  $dP$  represents the power collected by a receiver subtending a solid angle of  $d\Omega$  with respect to the scatterer, an expression corresponding to Eq. (A-1), but for spot illumination, can be written as

$$f(\theta) = \frac{I}{P_i \cos \theta} \quad (\text{A-2})$$

The  $\cos \theta$  obliquity factor in Eq. (A-2) accounts for the decrease in surface irradiance with increasing angle of incidence  $\theta$ . Only one obliquity factor occurs in the spot-illumination mode (in contrast with the flood-illumination mode) because the projected area of the illumination spot remains constant. Because the actual illuminated area of the surface sample is proportional to  $\cos^{-1} \theta$ , either a large sample or a small beam is required to make measurements at large aspect angles.

One approach to measuring  $f(\theta)$  by spot-illumination is to measure the radiometric intensity  $I$  and the incident power  $P_i$  separately and substitute them into Eq. (A-2). A better approach is to use a surface-material standard. The standard should be diffuse and highly reflective so that it approximates a Lambertian surface. Then,  $f(\theta)$  at normal incidence will then be close to the ideal value of  $f(0) = 1/\pi$ . The system calibration factor is determined by relating the instrument reading for normally incident illumination of the standard to the known  $f(0)$  value of the standard. Readings at angles other than normal incidence are divided by  $\cos \theta$  in accordance with Eq. (A-2).

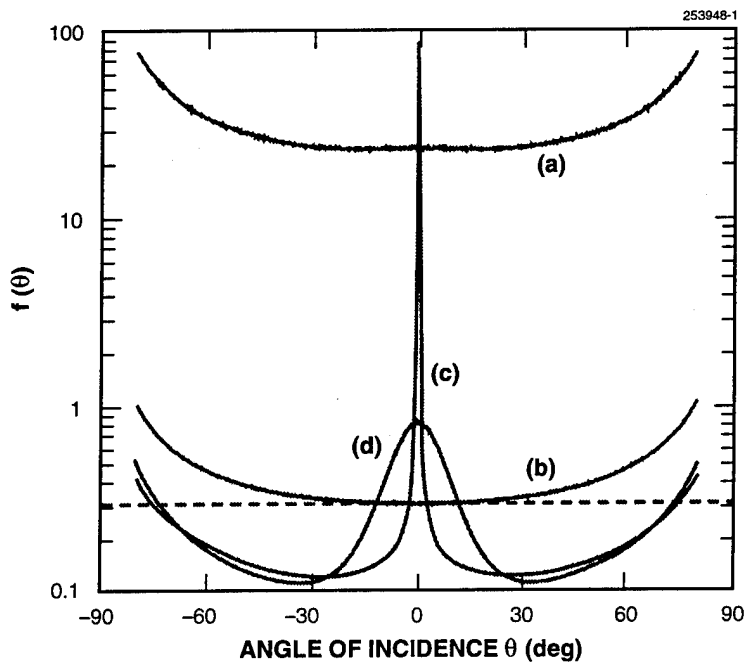


Figure A-1. Measured  $f(\theta)$ : (a) Newport HC-560 retroreflective paint; (b) Newport HC-563 white diffuse paint; (c) alodined aluminum; and (d) Krylon 1402 heat-resistant paint.

Figure A-1 contains measurements of  $f(\theta)$  obtained using the spot-illumination mode and the optical system depicted in Figure 19. In these measurements, flat samples of the surface material are placed in an angular positioner at the target location and illuminated by a HeNe laser with  $\lambda = 0.633 \mu\text{m}$ . The measurements of  $f(\theta)$  in Figure A-1 are for Newport HC-560 retroreflective paint, Newport HC-563 white diffuse paint, alodined aluminum, and Krylon 1402 heat-resistant paint. The dashed line represents a theoretical Lambertian surface with  $f(\theta) = 1/\pi$ . All of the measurements of  $f(\theta)$  curve upward for large values of  $\theta$ , even though the  $\cos \theta$  obliquity factor has been properly accounted for. The white diffuse paint most closely resembles a Lambertian surface. For monostatic purposes the retroreflective paint can be modeled as a Lambertian surface with a gain of approximately 20 dB.

## REFERENCES

1. P.P. Ewald, "Theory of X-ray Interference," *Phys. Zs.* **14**, 465–472 (1913).
2. R.W. James, *The Optical Principles of the Diffraction of X-Rays*, London: Bell (1950).
3. R. Hosemann and S.N. Bagchi, *Direct Analysis of Diffraction by Matter*, Amsterdam: North Holland (1962).
4. M. Nieto-Vesperinas, *Scattering and Diffraction in Physical Optics*, New York: Wiley (1991).
5. E. Wolf, "Three-Dimensional Structure Determination of Semi-Transparent Objects from Holographic Data," *Opt. Commun.* **1**, 153–156 (1969).
6. E. Wolf and R.P. Porter, "On the Physical Contents of Some Integral Equations for Inverse Scattering from Inhomogeneous Objects," *Radio Science* **21**, 627–634 (1986).
7. N.N. Bojarski, "The Far Field in Terms of the Spatial Fourier Transform of the Sources and Its Implications on the Inverse Problem," *J. Appl. Phys.* **58**, 1–5 (1985).
8. T-H. Chu, *Optimal Methodologies in Inverse Scattering Utilizing Wavelength, Polarization and Angular Diversity*, Ph.D. thesis, U. Pennsylvania (1983).
9. H.P. Baltes, ed., *Inverse Scattering Problems in Optics*, Berlin: Springer-Verlag (1980).
10. P.C. Sabatier, ed., *Basic Methods of Tomography and Inverse Problems*, Bristol: Adam Hilger (1987).
11. N. George and A. Jain, "Space and Wavelength Dependence of Speckle Intensity," *Appl. Phys.* **4**, 201–212 (1974).
12. N. George, A. Jain, and R.D.S. Melville, Jr., "Experiments on the Space and Wavelength Dependence of Speckle," *Appl. Phys.* **7**, 157–169 (1975).
13. N. George, "The Wavelength Sensitivity of Back-Scattering," *Opt. Commun.* **16**, 328–333 (1976).
14. N. George, "Speckle from Rough, Moving Objects," *J. Opt. Soc. Am.* **66**, 1182–1194 (1976).
15. N. George, A.C. Livanos, J.A. Roth, and C.H. Papas, "Remote Sensing of Large Roughened Spheres," *Opt. Acta* **23**, 367–387 (1976).
16. N. George, "Speckle," *SPIE* **243**, 124–140 (1980).
17. N.H. Farhat, in *Optics in Four Dimensions-1980*, M.A. Machado and L.M. Narducci, eds. (American Institute of Physics, New York, 1981), pp. 627–642.
18. C.K. Chan and N.H. Farhat, "Frequency Swept Tomographic Imaging of Three-Dimensional Perfectly Conducting Objects," *IEEE Trans. Antennas Propag.* **29**, 312–319 (1981).
19. J.Y. Wang, "Imaging Laser Radar—An Overview," *Proc. 9th Intl. Conf. Lasers '86*, 19–29 (1986).
20. J.L. Meyzonnette and G. Saccomani, "Imaging CO<sub>2</sub> Laser Radar, a Comparison of Three Techniques: LFM Pulse Compression, FMCW, CW," *Proc. SPIE* **999**, 91–99 (1988).

## REFERENCES (Continued)

21. E.M. Strzelecki, D.A. Cohen, and L.A. Coldren, "Investigation of Tunable Single Frequency Diode Lasers for Sensor Applications," *J. Lightwave Tech.* **6**, 1610-1618 (1988).
22. L.J. Sullivan, B.E. Edwards, and W.E. Keicher, "The Firepond High Power Carbon Dioxide Laser Radar System," *Proc. Intl. Conf. Radar '89*, Vol. **2**, 353-357 (1989).
23. L.G. Shirley, "Speckle Decorrelation Techniques for Remote Sensing of Rough Objects," in *OSA Annual Mtg. Tech. Dig.* **18** (Optical Society of America, Washington, 1989), p. 208.
24. L.G. Shirley, "Speckle Decorrelation," *Proc. IRIS Targets, Backgrounds, and Discrimination* **1**, 123-145 (1990).
25. A.L. Kachelmyer, "Range-Doppler Imaging with a Laser Radar," *Lincoln Lab J.* **3**, 87-118 (1990).
26. D. Klick, "A Laser Radar Experiment in Space: Firepond Images the Firefly Rocket," *Proceedings of the Intl. Conf. on Lasers 90*, 289-300 (1990).
27. D.J. McClure, "Diode Laser Radar—Applications and Technology," *Proc. SPIE* **1219**, 446-456 (1990).
28. D.J. Schertler and N. George, "Comparison of Wavelength Scanning and Pulse Echo Systems in Remote Sensing," *Opt. Commun.* **77**, 91-98 (1990).
29. L.G. Shirley, "Remote Sensing of Object Shape Using a Wavelength Scanning Laser Radar," in *OSA Annual Mtg. Tech. Dig.* **17** (Optical Society of America, Washington, 1991), p. 154.
30. L.G. Shirley and J.R. Vivilecchia, "Target Characterization Using a Wavelength Scanning Laser Radar," *Proc. Second Annual Automatic Target Recognizer System and Technology Conf.* (1992).
31. L.G. Shirley, E.D. Ariel, G.R. Hallerman, H.C. Payson, and J.R. Vivilecchia, "Advanced Techniques for Target Discrimination Using Laser Speckle," *Lincoln Lab. J.* **5**, 367-440 (1992).
32. W. Krohn and W.F. Matthews, "Multispectral Diode-Based Imaging Laser Radar," *Proc. SPIE* **1633**, 294-303 (1992).
33. J.C. Marron and K.S. Schroeder, "Three-Dimensional Lensless Imaging Using Laser Frequency Diversity," *Appl. Opt.* **31**, 255-262 (1992).
34. J.C. Marron and T.J. Schulz, "Three-Dimensional, Fine-Resolution Imaging Using Laser Frequency Diversity," *Opt. Lett.* **17**, 285-287 (1992).
35. T. Dresel, G. Hausler, and H. Venzke, "Three-Dimensional Sensing of Rough Surfaces by Coherence Radar," *Appl. Opt.* **31**, 919-925 (1992).
36. K.I. Schultz, S.A. Davidson, A.J. Stein, and J.K. Parker, "Range Doppler Laser Radar for Midcourse Discrimination: The Firefly Experiments," *2nd Annual AIAA SDIO Interceptor Technology Conference*, Albuquerque, NM, June, 1993.
37. L.G. Shirley and P.A. Lo, "Bispectral Analysis of the Wavelength Dependence of Speckle: Remote Sensing of Object Shape," *Opt. Soc. Am. A.* **11**, 1025-1046 (1994).

## REFERENCES (Continued)

38. M. Takeda and H. Yamamoto, "Fourier-Transform Speckle Profilometry: Three-Dimensional Shape Measurements of Diffuse Objects with Large Height Steps and/or Spatially Isolated Surfaces," *Appl. Opt.* **33**, 7829–7837 (1994).
39. "ALCOR Data Users and Radar Operators Manual, K<sub>a</sub> and W Bands," MIT Lincoln Laboratory Manual 134 (1 Aug 1988).
40. L.G. Shirley and N. George, "Diffuser Radiation Patterns over a Large Dynamic Range. 1: Strong Diffusers," *Appl. Opt.* **27**, 1850–1861 (1988).
41. C.E. Halford, W.L. Gamble, and N. George, "Experimental Investigation of the Longitudinal Characteristics of Laser Speckle," *Opt. Eng.* **26**, 1263–1264 (1987).
42. F.E. Nicodemus, "Reflectance Nomenclature and Directional Reflectance and Emissivity," *Appl. Opt.* **9**, 1474–1478 (1970).
43. F.E. Nicodemus, J.C. Richmond, J.J. Hsia, I.W. Ginsberg, and T. Limperis, *Geometrical Considerations and Nomenclature for Reflectance* (U.S. Government, Washington, 1977).
44. G.T. Ruck, D.E. Barrick, W.D. Stuart, and C.K. Krichbaum, *Radar Cross Section Handbook*, Vols. 1–2, New York: Plenum Press (1979).
45. W.R. Rambaucke and R.R. Gruenzel, "Distribution of Diffuse Optical Reflection around Some Stereometric Surfaces," *J. Opt. Soc. Am.* **55**, 315–318 (1965).
46. J.C. Dainty, ed., *Laser Speckle and Related Phenomena*, Berlin: Springer-Verlag (1984).
47. J.W. Goodman, *Statistical Optics*, New York: Wiley (1985).
48. W.F. McGee, "Complex Gaussian Noise Moments," *IEEE Trans. Inform. Theory* **17**, 149–157 (1971).
49. L.G. Shirley and N. George, "Speckle from a Cascade of Two Thin Diffusers," *J. Opt. Soc. Am. A* **6**, 765–781 (1989).
50. I.S. Reed, "On a Moment Theorem for Complex Gaussian Processes," *IRE Tran. Inform. Theory* **8**, 194–195 (1962).
51. J.R. Fienup, "Reconstruction of an Object from the Modulus of Its Fourier Transform," *Opt. Lett.* **3**, 27–29 (1978).
52. H. Stark, ed., *Image Recovery: Theory and Application*, New York: Academic Press (1987).
53. C.L. Nikias and M.R. Raghuveer, "Bispectrum Estimation: A Digital Signal Processing Framework," *Proc. IEEE* **75**, 869–891 (1987).
54. J.M. Mendel, "Tutorial on Higher-Order Statistics (Spectra) in Signal Processing and System Theory: Theoretical Results and Some Applications," *Proc. IEEE* **79**, 278–305 (1991).
55. A.W. Lohmann and B. Wirtzner, "Triple Correlations," *Proc. IEEE* **72**, 889–901 (1984).

## REFERENCES (Continued)

56. L.G. Shirley, G.R. Hallerman, and J.R. Vivilecchia, "Determination of Angular Surface Scattering from Measurements of Range-Resolved Laser Radar Cross Section," in *OSA Annual Mtg. Tech. Dig.* **23** (Optical Society of America, Washington, 1992), p. 205.
57. C. Brophy, "Design of an All-Glass Achromatic-Fourier-Transform Lens," *Optics Commun.* **47**, 364–368 (1983).
58. G.M. Morris and D.A. Zweig, "White-Light Fourier Transformations," in *Optical Signal Processing*, J.L. Horner, ed., San Diego: Academic (1987).
59. P.S. Idell, J.R. Fienup, and R.S. Goodman, "Image Synthesis from Nonimaged Laser-Speckle Patterns," *Opt. Lett.* **12**, 858–860 (1987).
60. D.G. Voelz, J.D. Gonglewski, and P.S. Idell, "Image Synthesis from Nonimaged Laser-Speckle Patterns: Comparison of Theory, Computer Simulation, and Laboratory Results," *Appl. Opt.* **30**, 3333–3344 (1991).
61. J.L.C. Sanz, ed., *Advances in Machine Vision*, Berlin: Springer-Verlag (1989).

# REPORT DOCUMENTATION PAGE

*Form Approved*  
**OMB No. 0704-0188**

Public reporting burden for this collection of information is estimated to average 1 hour per response, including the time for reviewing instructions, searching existing data sources, gathering and maintaining the data needed, and completing and reviewing the collection of information. Send comments regarding this burden estimate or any other aspect of this collection of information, including suggestions for reducing this burden, to Washington Headquarters Services, Directorate for Information Operations and Reports, 1215 Jefferson Davis Highway, Suite 1204, Arlington, VA 22202-4302, and to the Office of Management and Budget, Paperwork Reduction Project (0704-0188), Washington, DC 20503.

1. AGENCY USE ONLY ( <i>Leave blank</i> )	2. REPORT DATE <b>26 February 1996</b>	3. REPORT TYPE AND DATES COVERED <b>Technical Report</b>	
4. TITLE AND SUBTITLE <b>Applications of Tunable Lasers to Laser Radar and 3D Imaging</b>		5. FUNDING NUMBERS  C — F19628-95-C-0002 P — 342	
6. AUTHOR(S)  Lyle G. Shirley and Gregory R. Hallerman		8. PERFORMING ORGANIZATION REPORT NUMBER  TR-1025	
7. PERFORMING ORGANIZATION NAME(S) AND ADDRESS(ES)  MIT Lincoln Laboratory 244 Wood Street Lexington, MA 02173-9108		10. SPONSORING/MONITORING AGENCY REPORT NUMBER  ESC-TR-95-043	
9. SPONSORING/MONITORING AGENCY NAME(S) AND ADDRESS(ES)  U.S. Army Space and Strategic Defense Command CSSD-SD P.O. Box 1500 Huntsville, AL 35807		11. SUPPLEMENTARY NOTES  None	
12a. DISTRIBUTION/AVAILABILITY STATEMENT  Approved for public release; distribution is unlimited		12b. DISTRIBUTION CODE	
13. ABSTRACT ( <i>Maximum 200 words</i> ) <p>This report demonstrates the remote sensing of a scattering object's size, shape, and surface properties using techniques based on the wavelength dependence of laser speckle. Originally, these techniques were motivated by applications of laser radar to target discrimination in ballistic missile defense. More recently, the emphasis has shifted to industrial applications of 3D imaging involving machine vision and dimensional metrology. Consequently, the report addresses a wide range of techniques and potential applications.</p> <p>For applications to target discrimination, the capability of obtaining high-resolution measurements of the target's range-resolved laser radar cross section is emphasized. Submillimeter range resolutions are demonstrated in the laboratory. The analytical background is also included for predicting and understanding target signatures based on knowledge of the target's shape and the scattering properties of its surface materials.</p> <p>Two approaches to high-resolution 3D imaging are considered that have many potential industrial applications. The first approach is an extension of the technique for measuring range-resolved laser radar cross section. The second approach relies on the wavelength dependence of laser speckle to provide range information and conventional optical imaging to provide lateral information. These techniques are analyzed theoretically and demonstrated in the laboratory. Together, they cover object sizes ranging from millimeters to meters.</p>			
14. SUBJECT TERMS speckle                      bispectral analysis                      dimensional metrology                      target discrimination three dimensional imaging                      remote sensing                      speckle metrology                      frequency diversity laser radar cross section                      phase recovery                      metrology                      automatic target recognition laser radar                      tunable lasers                      wavelength decorrelation                      Ewald sphere autocorrelation support                      wide angle Fresnel approximation                      remote orientation sensing			15. NUMBER OF PAGES <b>138</b>
17. SECURITY CLASSIFICATION OF REPORT <b>Unclassified</b>			16. PRICE CODE
18. SECURITY CLASSIFICATION OF THIS PAGE <b>Unclassified</b>	19. SECURITY CLASSIFICATION OF ABSTRACT <b>Unclassified</b>	20. LIMITATION OF ABSTRACT <b>Same as Report</b>	